Multimodal modelling
of the human brain

DISSERTATION

to obtain the joint degree of Doctor at
the University of Liège and Maastricht University,

on the authority of the Rector Magnifici,
Prof. Dr. A. Corhay and Prof. Dr. L.L.G Soete

in accordance with the decision of the Board of Deans,
to be defended in public
on Thursday the 20th of November 2014 at 14:00 hours

by
Erik Ziegler

Supervisors

Prof. Dr. R. Goebel, Maastricht University

Ir Dr. C. Phillips, University of Liège

Dr. A. Roebroeck, Maastricht University

Assessment Committee

Prof. Dr. C. Geuzaine, University of Liège (Chairman)

Prof. Dr. H. Johansen-Berg, University of Oxford

Prof. Dr. A. Sack, Maastricht University

Prof. Dr. B. Vanrumste, University of Leuven

Abstract

There are many ways to model properties of the brain from magnetic resonance imaging (MRI) data. One acquisition technique, known as diffusion-weighted imaging (DWI), can map the speed and direction of water diffusion within the brain. This work explores the quantitative potential of DWI, in combination with other neuroimaging modalities, for *in vivo* modelling of the human brain.

Fiber tractography from DWI can be used to construct a wiring diagram of the brain (or *connectome*) and identify connectivity patterns between regions. To explore the utility of connectome modelling, we constructed brain networks from healthy subjects carrying known genetic variations. Using machine learning, we demonstrated high classification accuracy between subjects with different genotypes using only their connectomes.

Next, we tested whether fiber track density images could be used to detect early pathological effects in patients with Parkinson's disease. We found increases in track density in disease-relevant regions of the white matter, including the nigrostriatal pathway, used unbiased whole-brain statistical testing. This result is extremely encouraging, as axonal degeneration within this area is challenging to identify with standard magnetic resonance imaging contrasts.

Finally, a finite element modelling (FEM) approach was developed for solving the electroencephalography (EEG) forward problem. Electrical conductivity tensors were estimated from DWI in order to represent the heterogeneous conductivity profile of the white matter. When tested against the analytical solution, this FEM method proved more reliable than the current state-of-the-art alternative.

Advanced brain modelling from DWI can clearly provide lucrative results. These methods have been open-sourced for use by the community.

Propositions

In complement of the Ph.D. thesis

Multimodal modelling of the human brain

Erik Ziegler

Maastricht, Thursday the 20th of November, 2014

1. Genetic bases shape the human connectome.

2. Most polymorphisms are subtle and may be undetectable by neuroimaging.

3. Polymorphisms in genes affecting ubiquitous neurotrophic agents can produce macroscale structural changes in the brain.

4. Axonal damage from Lewy neurites may be the earliest sign of Parkinson's disease, preceding somatic atrophy in the substantia nigra.

5. *In vivo* identification of Parkinsonian neurodegeneration with advanced diffusion imaging is possible and may be a viable alternative to presynaptic dopaminergic radiotracers.

6. Neural source localization methods should not overlook the conductivity profile of the white matter.

7. Accurate finite element head modeling can improve both passive and active neuroscience methods.

8. Your project is not unique: release your methods early and let everyone know what you are working on.

9. Open and distributed software development should be embraced.

10. Cloud and GPU computing tools should be taught to neuroscientists.

11. Peer review is the worst system, except for all the others.

List of Publications

This thesis is based on the following papers, which are referred to in the text by their Roman numerals:

I. **Altered white matter architecture in *BDNF* Met carriers**
    Ziegler, E., Foret, A., Mascetti, L., Muto, V., Le Bourdiec-Shaffii, A.,
    Stender, J., Balteau, E., Dideberg, V., Bours, V., Maquet, P., Phillips, C.
    PLoS One, 2013, 8(7): e69290, doi:10.1371/journal.pone.0069290

II. **Mapping track density changes in nigrostriatal and extranigral pathways in Parkinson's disease**
    Ziegler, E., Rouillard, M., André, E., Coolen, T., Stender, J., Balteau, E.,
    Phillips, C.*, Garraux, G.*
    NeuroImage, Volume 99, October 1st 2014, Pages 498-508
    ISSN 1053-8119, doi:10.1016/j.neuroimage.2014.06.033

III. **A finite-element reciprocity solution for EEG forward modeling with accurate individual head models**
    Ziegler, E., Chellappa, S. L., Gaggioni, G., Ly, J. Q. M., Vandewalle, G.,
    André, E., Geuzaine, C.*, Phillips, C.*
    NeuroImage, 2014, In Press
    doi:10.1016/j.neuroimage.2014.08.056

* Contributed equally

Contents

List of Figures

Glossary

^{18}F-DOPA

[^{18}F]-L-dihydroxyphenylalanine - Similar to L-DOPA, it is a dopamine precursor. Its uptake in the brain can be used to assess presynaptic dopamine terminal function. 47

circadian

Biological, mental, and behavioural changes that occur in an approximate 24-hour cycle. Circadian ~ circa + dia ~ about + day. 42

Dipy

Dipy is a free and open source Python software package for diffusion magnetic resonance imaging (dMRI) analysis.
Available at: `http://nipy.sourceforge.net/dipy/` 13

dyskinesia

Involuntary muscle movements, tremors, and/or other uncontrollable movement. 47

Freesurfer

A set of tools for analysis and visualization of structural and functional brain imaging data. FreeSurfer contains a fully automatic structural imaging stream for processing cross-sectional and longitudinal data.
Available at: `https://surfer.nmr.mgh.harvard.edu/` 19, 54

GetDP

GetDP is a general finite element solver for discrete problems defined by the user (e.g. electrostatics, magnetodynamics).
Available at: `http://www.geuz.org/getdp/` 54

long-term potentiation

Enhanced signalling between neurons caused by their simultaneous stimulation. 41, 42

MNE

MNE is a software package for processing magnetoencephalography (MEG) and EEG data. A Python package for further analysis, called MNE-Python, is also available.
Available at: `http://martinos.org/mne` 35

MPTP

1-methyl-4-phenyl-1,2,3,6-tetrahydropyridine - a neurotoxin that destroys dopaminergic neurons in the substantia nigra. 49

Nipype

Nipype is a Python project that provides a uniform interface to existing neuroimaging software and facilitates interaction between these packages within a single workflow.
Available at: `http://nipy.sourceforge.net/nipype/` 54

SimNIBS

SimNIBS is a MATLAB and UNIX shell script package designed for realistically calculating the electric field induced by transcranial magnetic stimulation (TMS).
Available at: `http://simnibs.org/` 54–56

single-nucleotide polymorphism

Changes from one nucleotide (e.g. G, T, A, C) to another at a specific codon (i.e. position in the genetic code) of a certain gene. 42, 43, 45

striatum

Subcortical collection of structures. It is made up of the caudate nucleus and the putamen. 47

substantia nigra

A largely dopaminergic region in the midbrain important for movement and reward signalling. 47

the FMRIB Software Library

    FSL is a general library for analyzing, transforming, and manipulating MRI data.

    Available at: `http://fsl.fmrib.ox.ac.uk/fsl/fslwiki/` 48

Introduction

The primary aim of this research was to combine two neuroimaging modalities: diffusion-weighted magnetic resonance imaging (DWI) and electroencephalography (EEG).

A relatively new method, DWI allows researchers to quantify the mobility of water molecules within biological tissue. Diffusion of water molecules is naturally hindered by cellular structures as well as other micro and macrostructural factors. This technique allows researchers to trace, at a large scale, the neural tracts that transport information throughout the brain.

EEG, which is one of the oldest methods in functional neuroscientific research, monitors electrical signals produced by synaptic activity. Unlike MRI methods, EEG does not create an image of the brain. Rather, it records electrical activity over time through electrodes placed on the scalp. A key issue modern day researchers face with EEG is identifying the origin of interesting physiological signals. Providing tools to address this problem was one aim of this work. The secondary focus of this work was to develop and explore advanced diffusion-weighted imaging analysis techniques for use in future neuroscientific studies.

Chapter 1 provides a brief review of the physics, biology, and practical issues related to diffusion-weighted imaging. Chapter 2 covers the basics of EEG and the problem of source localization. The following three chapters describe a set of studies performed in parallel:

I. The first study assesses genetic influences on the wiring of the human brain using network analysis methods.

II. The second study tests whether the quantification of fiber tractogram models can be used as a marker for Parkinson's disease.

III. The third study describes a method for creating accurate EEG leadfield matrices - a key step in localizing neuronal sources - using head models with DWI-derived conductivity tensors.

The full detailed manuscripts of these studies are available in Appendices A, B, and C. For the interested reader, these manuscripts offer in-depth descriptions of the methods, results, and implications of these studies. In Chapters 3, 4, and 5, there is an overview of each study and a discussion of topics not present in the manuscripts.

The thesis closes by discussing the current state of the neuroimaging field in relation to methodological reproducibility (Chapter 6) and summarizing the work performed (Concluding remarks).

Diffusion-weighted imaging

Diffusion is the process of mass transport in a medium from areas of high concentration to those of low concentration. Molecular diffusion describes the random movement of molecules, also known as Brownian motion, in the absence of a concentration gradient. Molecular diffusion rates depend principally on the size of the molecule and the temperature of the medium. For example, the diffusion coefficient (or diffusivity) of water $D_{H_2O,25°C}$ is 2.3 x 10^{-3} mm^2/s at 25° Celsius. Diffusivity is expressed as an area (mm^2) per unit time (s) because it is proportional to the particles' mean velocity and mean free path (i.e. the distance travelled between collisions).

Diffusion-weighted imaging (DWI) is a type of MRI technique in which successive applications of strong magnetic gradient pulses are used to dephase and rephase the spins of protons. Spins that are static will be fully refocused whereas spins that have moved will rephase less. Regions in which there is a higher rate of water motion will produce less signal than those in which there is a lower rate. For further insight into diffusion MRI, the reader is referred to [1].

The acquired diffusion signal from a pulsed gradient technique depends on characteristics other than the diffusion coefficient. Specifically, scanner and sequence-specific variables such as the gyromagnetic ratio, applied gradient pulse strength, time between pulses, and pulse duration are directly related to the signal. For simplification, these variables are bundled into an abstract measure known as the "b value". The b value is linked to the acquired diffusion-weighted signal (S) and the unweighted signal (S_0) by Equation 1.1:

$$S(b) = S_0 e^{-bADC} \tag{1.1}$$

The variable ADC in Equation 1.1 is the apparent diffusion coefficient, which is included because diffusion in biological tissue is influenced by various factors (e.g.

cellular structure). Figure 1.1 shows brain images acquired with varying levels of diffusion weighting.

Diffusion imaging acquisitions typically apply the pulsed gradient sequence described above along many unique gradient directions [2]. In this manner the acquired signal reflects the rate of diffusion of water molecules within each voxel along the direction of the applied magnetic field. By mapping the diffusion profile in each direction one can infer properties about the macro and microscopic structure of the tissue being studied. For an extensive review of diffusion-weighted imaging, the reader is referred to [3] and [4]. In practice, most neuroimaging researchers tend to care about two things: (i) the applied b value, and (ii) the number of gradient directions (or "b vectors") the data was acquired with.

| Unweighted image
(b=0) | Diffusion-weighted
b=1000 s/mm^2 | Diffusion-weighted
b=2500 s/mm^2 |
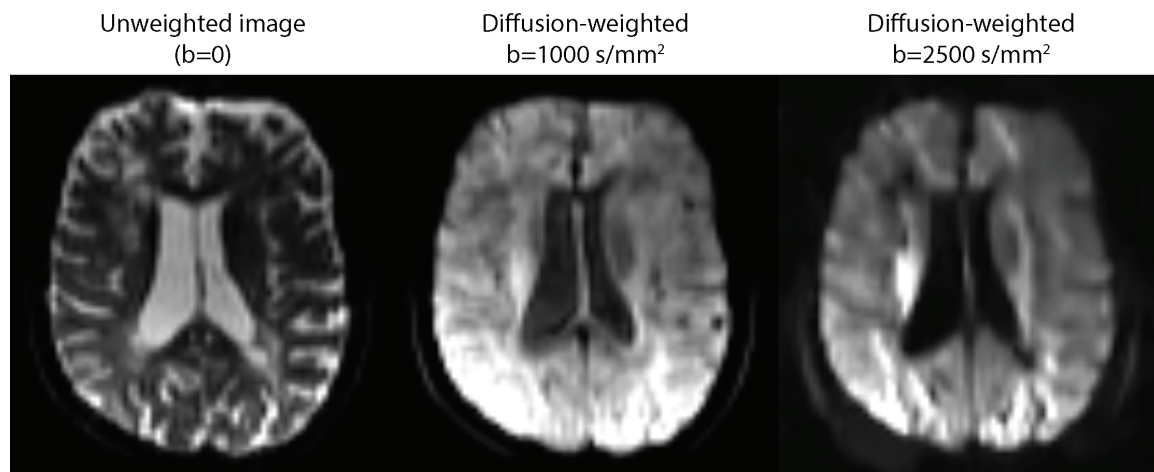
Figure 1.1: Example weighted and unweighted images. Three images of a patient with multiple sclerosis. Images were acquired at b=0, b=1000 s/mm^2, and b=2500 s/mm^2. The two diffusion-weighted images are weighted along similar gradient directions (approximately [-0.8, -0.40, 0.25]).

1.1   Modelling diffusion profiles

The analysis of diffusion-weighted images generally requires the selection of a model to represent the diffusion profile in each voxel. There are alternative methods, though, such as diffusion spectrum [5] and q-ball [6] imaging, which do not require the choice of a model. The typical choice is a tensor, and tensors can be fit to the diffusion signal in each voxel using a variety of different methods [7, 8]. Briefly,

the goal is to solve Equation 1.2 for $\mathbf{D}$.

$$S(g, b) = S_0 e^{-bg^T \mathbf{D} g} \tag{1.2}$$

Where $\mathbf{D}$ is a tensor defined by Equation 1.3, and $g = [g_x, g_y, g_z]$ is the gradient direction defined as a vector.

$$\mathbf{D} = \begin{pmatrix} D_{xx} & D_{xy} & D_{xz} \\ D_{yx} & D_{yy} & D_{yz} \\ D_{zx} & D_{zy} & D_{zz} \end{pmatrix} \tag{1.3}$$

It is important to note that this tensor is symmetric about the diagonal ($\mathbf{D} = \mathbf{D}^T$). Because the diffusion coefficient is a real and positive-valued function, the eigenvalues of this matrix must also be positive and real values. The diffusion tensor is often referred to as a symmetric positive definite matrix.

Studies commonly fit the diffusion tensor using an ordinary linear least squares fit to the natural logarithm of the signal. In the presence of noise, though, this type of fitting can produce negative eigenvalues. Weighted linear least squares fitting [9] and non-linear least squares solutions [7] are preferable because they are more robust. Non-linear least squares solutions also do not require log transformation of the signal, which makes it easier to factor out errors in the signal [10]. Tensor fits can be constrained through post-estimation methods for correcting negative eigenvalues, such as taking their absolute value [7]. Iterative methods for outlier rejection, such as RESTORE [8], also offer robust tensor fitting, but require a solid estimate of the noise in the data. Estimating the noise in a DWI acquisition can be performed by calculating the standard deviation of the background of an unweighted image or by assessing the deviation between two or more repeated (un)weighted scans.

The diffusion signal intensity does not vary linearly with b value [11], though this approximation is sufficient up to about b = 1000 s/mm^2 (see Figure 1.2). Studies with more than one b value are described as "multi-shell" acquisitions, and studies wishing to perform more complex analyses usually include a separate high b value acquisition (e.g. at b = 2500 s/mm^2). One such analysis method, diffusion kurtosis imaging (DKI), is used to quantify the non-Gaussianity of the diffusion within a voxel. DKI fits require high b values and fit the data using a quadratic approach [12].

There are various ways to generate gradient directions for a DWI experiment, though the most common approach is based on an electrostatic repulsion model in a sphere [13]. Researchers generally acquire volumes using at least 30 unique gradient
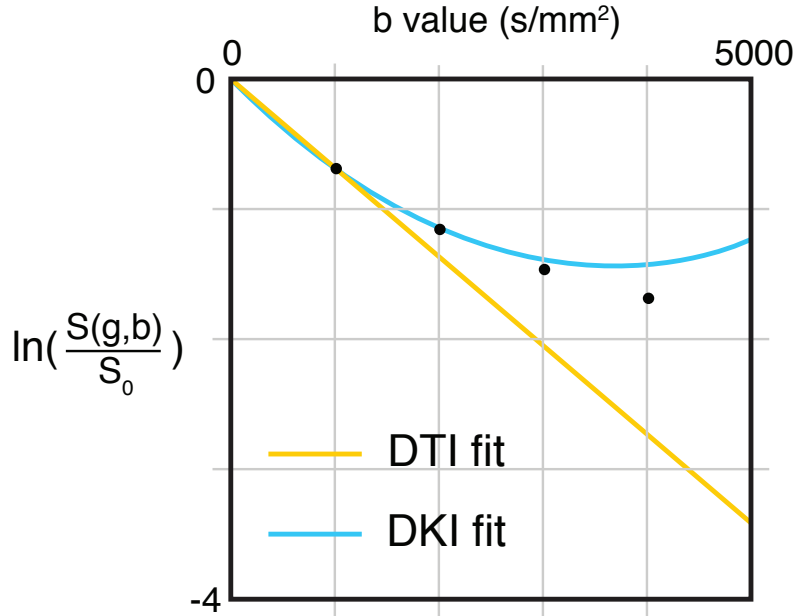
Figure 1.2: Diffusion signal dependence on b value. The diffusion-weighted imaging signal drops at higher b values. At b values greater than 1000 s/mm^2 the linear fitting approach used for diffusion tensor imaging (DTI) no longer applies to the data. High b value acquisitions are often analyzed using diffusion kurtosis imaging (DKI), which fits the signal using a parabola. Adapted from [12].

directions so that tensors can be fit reliably [14]. Studies with large numbers of directions (usually > 40) are referred to as high angular direction diffusion imaging (HARDI) datasets [15].

1.1.1   Diffusion tensor imaging (DTI)

In neuroimaging studies, tensors are usually analyzed with metrics calculated from their eigenvalues. The most common measures are fractional anisotropy (FA) and mean diffusivity (MD), though others, such as radial diffusivity and tensor mode [16, 17] have also proven useful. Mean diffusivity is calculated using Equation 1.4:

$$MD = \frac{\lambda_1 + \lambda_2 + \lambda_3}{3} \tag{1.4}$$

Where λ_1, λ_2, and λ_3 represent the eigenvalues of the tensor. Fractional anisotropy, which describes how directional a tensor is, can be calculated using Equation 1.5.

$$FA = \sqrt{\frac{1}{2}\frac{(\lambda_1 - \lambda_2)^2 + (\lambda_1 - \lambda_3)^2 + (\lambda_2 - \lambda_3)^2}{\lambda_1{}^2 + \lambda_2{}^2 + \lambda_3{}^2}} \tag{1.5}$$

Tensor mode provides a method for quantifying the type of anisotropy (e.g. planar = two fiber populations, or linear = one fiber population) found in the voxel. This can be useful in combination with FA, for example, to help identify the mechanisms of pathological damage. Mode ranges between -1 (planar anisotropy) and +1 (linear anisotropy) with 0 representing orthotropy. To calculate the mode of a tensor ($\mathbf{D}$) we must first calculate the isotropic part ($\bar{\mathbf{D}}$) of the tensor using Equation 1.6.

$$\bar{\mathbf{D}} = \frac{1}{2}(\lambda_1 + \lambda_2 + \lambda_3)I \tag{1.6}$$

Where I is the identity matrix. The deviatoric part ($\widetilde{\mathbf{D}}$) of the tensor is defined in Equation 1.7.

$$\widetilde{\mathbf{D}} = \mathbf{D} - \bar{\mathbf{D}} \tag{1.7}$$

Mode is then calculated with the following equation:

$$Mode = 3\sqrt{6} * det(\frac{\widetilde{\mathbf{D}}}{||\widetilde{\mathbf{D}}||}) \tag{1.8}$$

Where det refers to the matrix determinant and $||x||$ refers to the Euclidean (ℓ^2) norm.

A set of tensor-derived measures for a set of real data can be found in Figure 1.3. In this image, FA is highest in the largest fiber pathways, such as the corticospinal tracts. Mean diffusivity is greatest in the ventricles and cerebrospinal fluid, as the diffusion is unhindered in these regions. Tensor mode is highest in large single-tract areas, reflecting the linearity of their diffusion profiles.

In order to convey anatomical qualities in tensor data, studies often colour each voxel using a convention based on the principal direction of its tensor. For example, in a voxel with the principal direction oriented left-to-right, the voxel may be given a red-green-blue (RGB) value for red. The standard convention is that left-to-right is red, anterior-to-posterior is green, and inferior-to-superior is blue. These colour maps can also be modulated by the FA values in each voxel, leading to what is known as an RGB-FA image [18]. For reference, a standard high-resolution T1-weighted magnetic resonance image (T1) and an RGB-FA image are shown in Figure 1.4. Tensors are also commonly portrayed as coloured directional ellipsoids.

One further quality of diffusion tensors is that their eigenvalues can be scaled to approximate conductivity tensors [19, 20]. The scaling required was first assumed to be linear, though this has been called into question by incongruities between
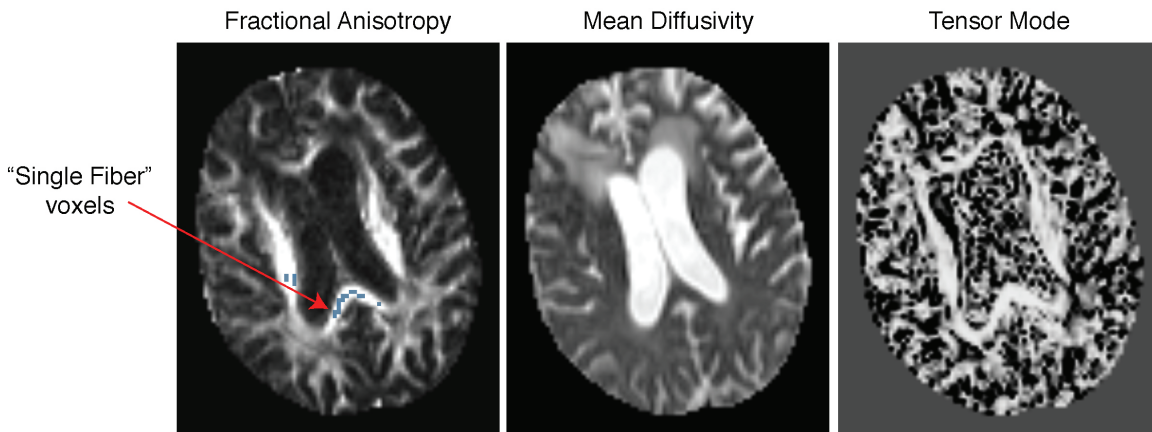
Figure 1.3: Tensor-based diffusion measures. Fractional anisotropy (FA), mean diffusivity (MD), and tensor mode maps for a severely brain-damaged patient. A red arrow points to a set of calibration voxels for spherical deconvolution, which are shown in blue.
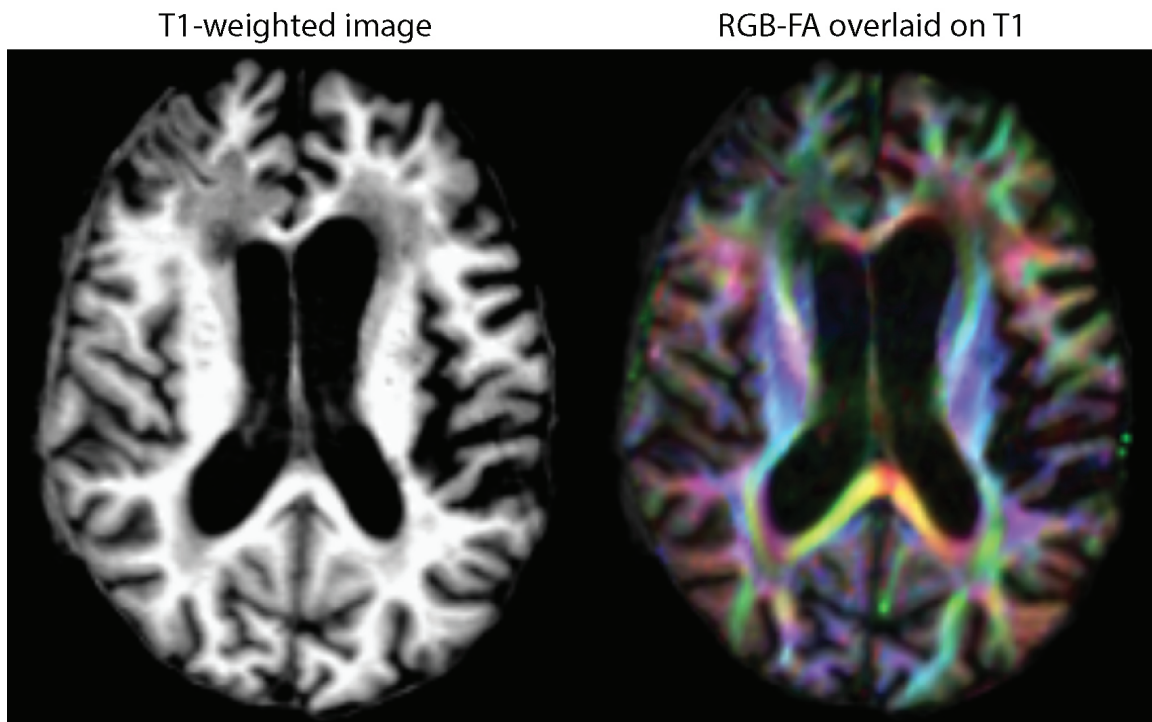
Figure 1.4: Example RGB-FA and T1-weighted images. *Left:* a typical high-resolution T1-weighted magnetic resonance image in a brain-damaged patient. *Right:* A red-green-blue (RGB) fractional anisotropy image overlaid on the T1. The RGB colours are calculated from the principal direction of the tensor in each voxel, and their intensity is modulated by the fractional anisotropy (FA) in that voxel. The colours follow the generally accepted convention: Red: Left-Right, Green: Anterior-Posterior, Blue: Inferior-Superior

phantom and *in vitro* studies of excised brain tissue [21–23]. Although direct mapping of eigenvalues has been used most often, a method for "volume normalized" tensor remapping has been proposed. In volume normalized tensor remapping, the directional information of the tensor is kept untouched, but the mean conductivity of the tensor is forced to a pre-defined value. The value chosen is usually the mean conductivity that is assumed in studies with isotropic conductivity profiles. This is meant to prevent the inclusion of erroneously high conductivity values that can be adopted during direct mapping [24].

In the human brain tensors cannot fully portray the real-world properties of the voxels they represent, as most white matter voxels contain more than one unique fiber population [25]. Their primary fault is their unidirectionality, and higher-order diffusion models aim to address this issue. There have been several demonstrated alternatives (e.g. multi-tensor models [15]) for representing diffusion profiles, though we do not deal with them in this thesis. Instead, as we intend to perform fiber tractography, we focus on estimating fiber orientation distribution functions (FODs, or fODFs), which should not be confused with diffusion orientation distribution functions (dODFs).

1.1.2 Fiber orientation distributions (FODs)

Fiber orientation distributions do not aim to represent the diffusion profile in a voxel. Instead, they aim to represent the distribution of fiber tracts inside a voxel. As such, their derivation is based on the idea that the diffusion profile in any single voxel is the sum of the diffusion profile of all the fibers passing through the voxel. FODs are commonly fit using spherical deconvolution [26], though other methods are available. Before explaining spherical deconvolution it is prudent to introduce spherical harmonics.

Spherical harmonics are easiest to explain by way of an analogy to the Fourier series. The Fourier series is a method for approximating or deconstructing a signal using a sum of several oscillatory functions. These oscillatory functions are essentially modulated sinusoidal functions. As a simple example, the square wave shown in Figure 1.5 is being approximated by a high-order combination of sine functions. Using basis functions to approximate a signal is performed in exactly the same manner using spherical harmonics.

The spherical harmonic basis functions are not sinusoidal functions but more complex functions defined in a spherical coordinate system. In spherical coordinates
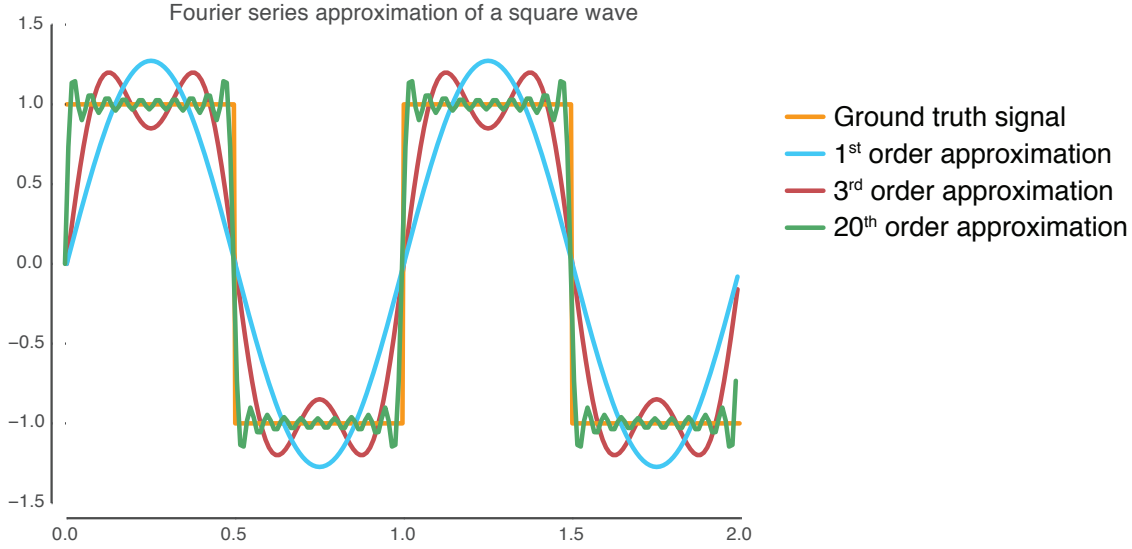
Figure 1.5: Fourier series approximation of a square wave. Decomposition of a square wave into a sum of sine functions using the Fourier series. Spherical harmonic basis functions are analogous to the Fourier series, but for functions defined on a sphere, rather than periodic signals.

points are defined using their elevation angle (θ), azimuthal angle (ϕ), and radius (r), rather than x, y, and z values. Spherical harmonic basis functions are all defined to have unit radii and are therefore only functions of θ and ϕ. Spherical harmonics are denoted by two numbers, their degree (m, sometimes called the phase factor) and their harmonic order (l, or sometimes n). The first six real-valued spherical harmonics ($\Re(Y_l^m(\theta,\phi))$) for l=[1-3], 0≤m<l) are plotted on spheres on the left panel of Figure 1.6. In the right panel of Figure 1.6 they are plotted again, but with their radius scaled by the function's value.

As mentioned earlier, the key assumption behind spherical deconvolution approaches is that the measured signal in any voxel depends on the number of fibers in the voxel, the amount of space they occupy, and the signal each fiber generates [26]. Equation 1.9 relates the signal $S(\theta,\phi)$ with the volume fraction of the voxel taken up by each fiber (f_i). The signal (or response) for each fiber is assumed to be equal and is represented as an axially symmetric function ($R(\theta)$). One further term, $\hat{A}_i$, acts as a rotation operator to account each fiber's orientation (θ_i, ϕ_i) within the voxel.

$$S(\theta,\phi) = \sum_i f_i \hat{A}_i R(\theta) \tag{1.9}$$
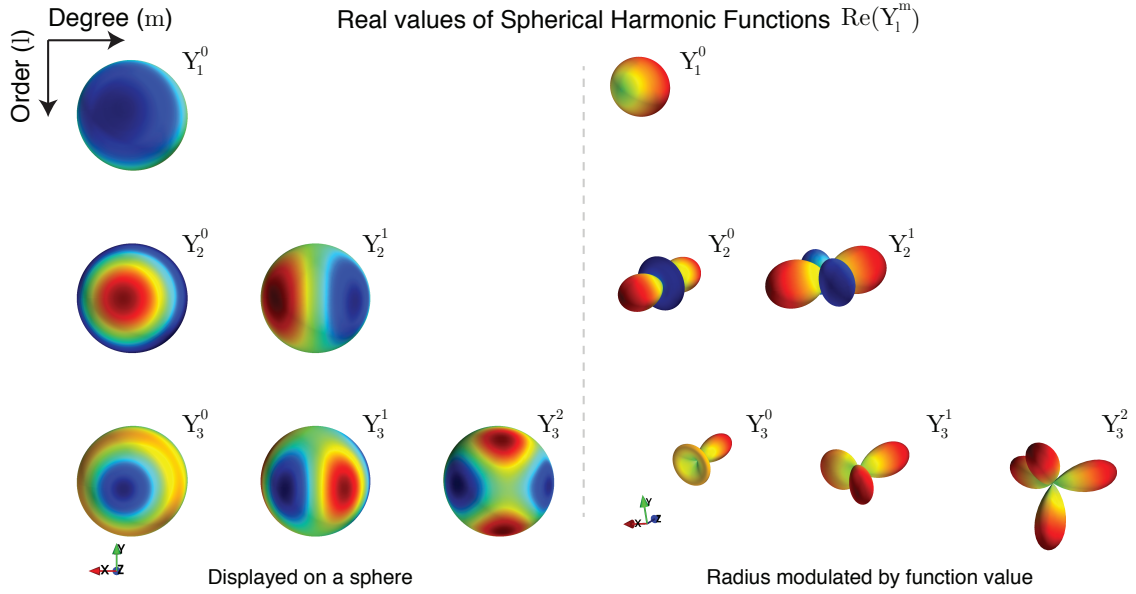
Figure 1.6: Real-valued spherical harmonic functions. A demonstration of the first six real-valued spherical harmonics ($\Re(Y_l^m(\theta, \phi))$ for l=[1-3], 0≤m<l). These functions are defined using spherical (polar) coordinates (i.e. using θ, ϕ, and r to represent the azimuthal angle, polar angle, and the radius, rather than using the Cartesian x, y, z coordinate system). Often the radius is modulated by the value of the function, leading to the plots shown on the right.

In order to simplify Equation 1.9, we can reduce the problem and state that the measured signal in any voxel is a convolution of the fiber orientation distribution ($F(\theta, \phi)$) in that voxel and the diffusion-weighted signal response for a single-fiber population ($R(\theta)$).

$$S(\theta, \phi) = F(\theta, \phi) \otimes R(\theta) \tag{1.10}$$

The "single-fiber response" ($R(\theta)$) is estimated from voxels expected *a priori* to contain only fibers oriented in one direction. The response is then assumed to be equal for every fiber throughout the white matter. This calibration has historically been done by selecting fibers with high FA, though some iterative [27] and recursive [28] methods have also been described. As an example a set of suitable calibration voxels is overlaid on the FA image in Figure 1.3.

Since diffusion is a real function, the imaginary portions of the spherical harmonics can be ignored, which reduces by half the number of parameters to estimate. Because diffusion is symmetric about the origin, odd (i.e. $l = 1, 3, ...$) harmonic orders can be discarded.

The spherical harmonic representation of the signal (S^l) is first obtained by a linear least squares fit [29]. The system described in Equation 1.11 is then solved for the fiber orientation distribution (F^l) at each voxel by inverting the response function (R^l) and multiplying it by S^l.

$$S^l = F^l R^l \tag{1.11}$$

In these equations F^l is a vector of length $(2l + 1)$ that represents the spherical harmonic decomposition of $F(\theta, \phi)$ up to a harmonic order l. The lth order rotational harmonic decomposition of $R(\theta)$ is represented using a $(2l + 1)(2l + 1)$ matrix (R^l). Due to its axial symmetry, the response function collapses to a single real scalar constant for each harmonic order. The spherical deconvolution approach is thus reduced to a single matrix multiplication at each voxel. A constraint of non-negativity can be imposed on the fiber orientation distribution to improve the fitting, and this technique is known as constrained spherical deconvolution (CSD) [30, 31]. For a detailed background of fiber orientation distribution (FOD) estimation by spherical deconvolution, the reader is referred to [26].

The fiber orientation distributions are approximated by a linear combination of spherical harmonic basis functions which are then truncated at a specified maximum order harmonic. The number of parameters required for fitting the FOD depends on the maximum order chosen, as shown in Table 1.1. In practice, this means that the number of unique gradient directions acquired determines the maximum harmonic order one can use for estimating FODs using spherical deconvolution.

Table 1.1: Number of parameters required for each maximum harmonic order

Maximum harmonic order	Number of parameters required
2	6
4	15
6	28
8	45
10	66
l	$\frac{1}{2}(l + 1)(l + 2)$

There are various sources of error in this technique and they have yet to be fully characterized. It is clear that the choice of calibration voxels is extremely important, as is the choice of the harmonic order at which to truncate the function [27, 32]. In general, taking higher harmonic orders into account will allow the FODs to more

faithfully represent the fiber distribution in each voxel. In practice, though, the impact of maximum harmonic orders higher than 8 on the FOD fit is negligible for the b values used in most studies (b < 3000 s/mm^2) [27]. The use of lower harmonic orders can reduce the effect of noise and errors due to miscalibration (e.g. when the single-fiber voxels are poorly chosen) [32]. Selecting the maximum harmonic order is therefore a difficult and controversial decision as the choice can affect the results of the study. Alternative methods for calibration-free spherical deconvolution have been proposed, including damped Richardson-Lucy deconvolution [33] and voxel-by-voxel response estimation [34].

It has been estimated that as much as 90% of the white matter contains multiple intersecting fiber populations [25]. While FOD estimation approaches may have issues that voxel-by-voxel tensor estimation does not, they offer multi-direction intra-voxel fiber modelling which is imperative for accurate tractography. Figure 1.7 shows a side-by-side comparison of tensors and fiber orientation distributions in an axial slice of the frontal lobe in a healthy subject.

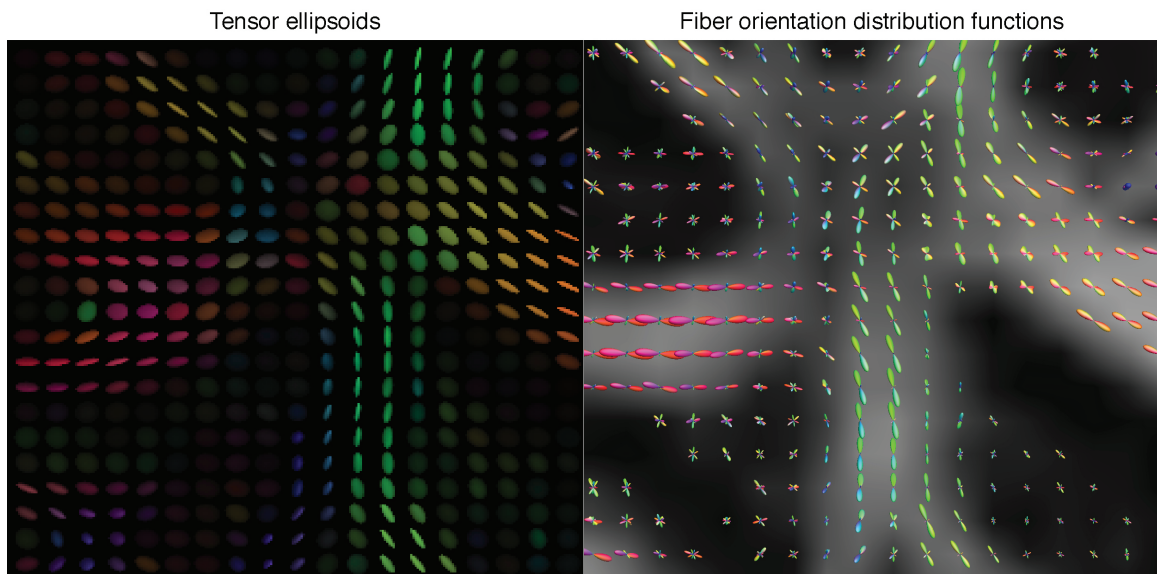**Figure 1.7: Tensors and fiber orientation distributions.** A single axial slice showing the anterior forceps. Crossing fiber regions are represented more accurately using orientation distribution functions. FODs are overlaid on the fractional anisotropy image. Stanford HARDI dataset courtesy of Dipy. Colours follow the standard convention: Red: Left-Right, Green: Anterior-Posterior, Blue: Inferior-Superior.

1.2   Fiber tractography

Streamline tractography algorithms can be used to create wiring models of the brain. Generally, the idea of tractography is that an algorithm individually estimates multiple streamline pathways from one part of the brain to another based on the diffusion or fiber orientation model calculated at each voxel. Fiber tracks are seeded in white matter regions and progressive tracking steps are taken until the streamline is terminated. There are multiple approaches for choosing a direction to step in, as well as for evaluating the probability that two voxels are connected by a track. For an extensive review and quantitative comparison of tracking algorithms using a DWI phantom, the reader is referred to the "Fiber Cup" results [35]. When referring to the results of fiber tractography, we will use the terms "fibers", "tracks", and "streamlines" interchangeably, and these should not be confused with actual biological tracts [36]. When discussing a set of modelled tracks in a subject we will use the term "tractogram".

Tractography has recently evolved from deterministic to probabilistic. In deterministic tracking a single path is estimated by choosing the best available direction at each progressive step. Probabilistic tracking, on the other hand, tests numerous paths for each fiber track before choosing the most likely. In the tracking implementation used in Paper I and II, the direction of each step is chosen by randomly sampling the FOD function [37]. Rejection sampling is used to sample the FOD on the fly and choose the trajectory of the track. The tracking step is taken if the amplitude of the FOD peak is greater than a user-defined threshold[1], and the curvature of the tracks is less than the maximum allowable turning angle. This FOD amplitude threshold can help prevent implausible streamlines. Anatomically defined masks (e.g. of grey matter and cerebrospinal fluid) can be used to terminate or otherwise prevent "false positive" streamlines from being considered in the final tractogram [38]. Tracks are commonly seeded from random voxels within a masked region[2]. In Figure 1.8, white matter (WM) and termination masks are shown for a severely brain-damaged patient.

Track seeding is usually performed until a user-defined maximum number of tracks is reached. Alternatively, a specific number of tracks can be seeded from every voxel in the mask. The tracks can later be filtered to remove pathways through

---

[1]tensor-based tracking methods use a minimum FA threshold
[2]for whole brain tracking, this is the white matter mask

White matter mask

Termination Mask

FLAIR image of MS patient
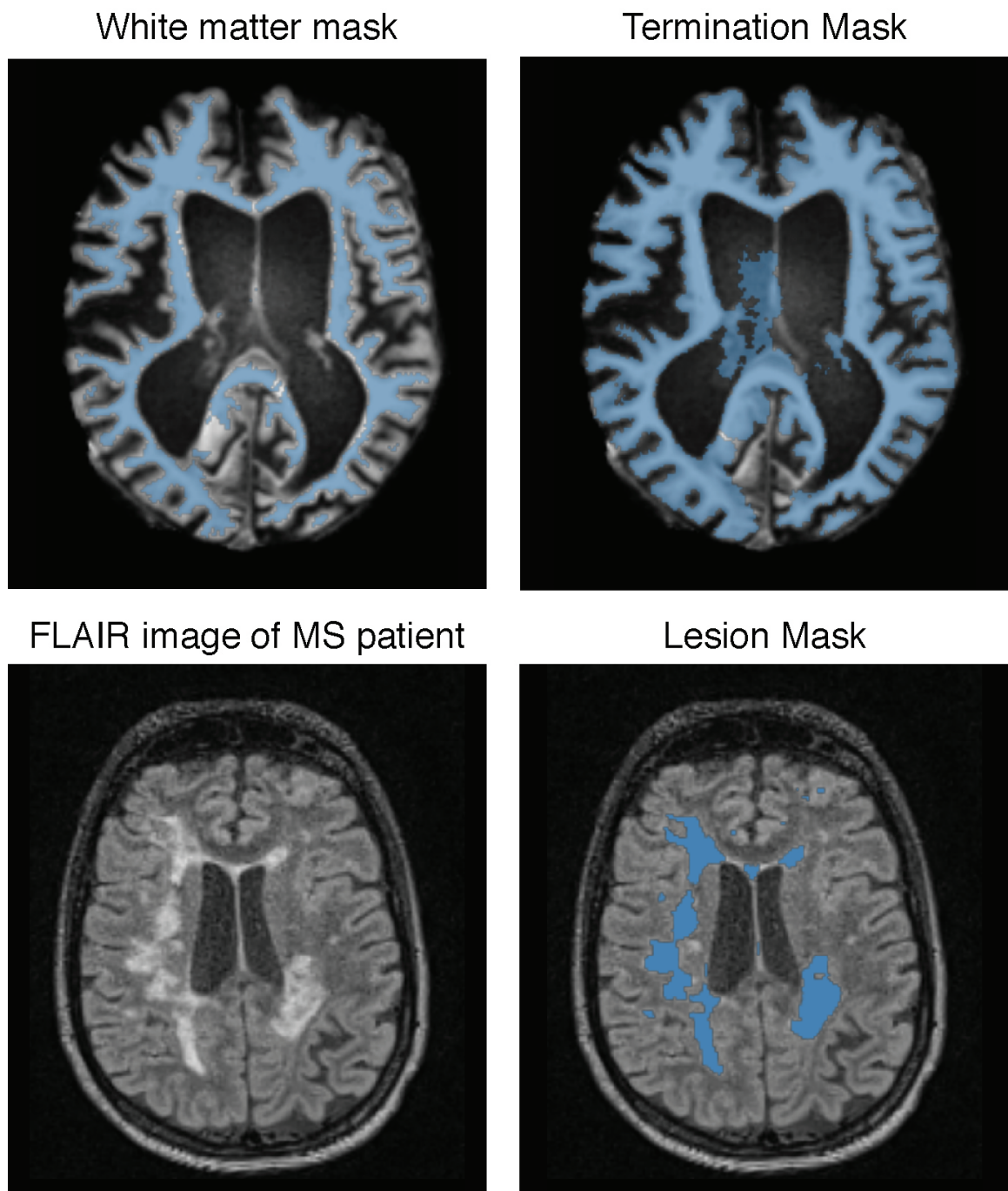
Lesion Mask

Figure 1.8: Example white matter and termination masks. *Top:* White matter and cerebrum masks (blue) overlaid on the T1 of a severely brain-damaged patient. *Bottom:* fluid attenuated inversion recovery (FLAIR) image and lesion masks for a patient with multiple sclerosis (MS) and clear white matter lesions. Streamlines are seeded in voxels of the white matter mask. Fiber tracks are terminated when they extend out of the termination mask or into the lesion mask.

unlikely areas, for example by comparing the streamline distribution with the amplitude of the FOD peaks [39]. A cortical tractogram for a healthy subject is shown in Figure 1.9.
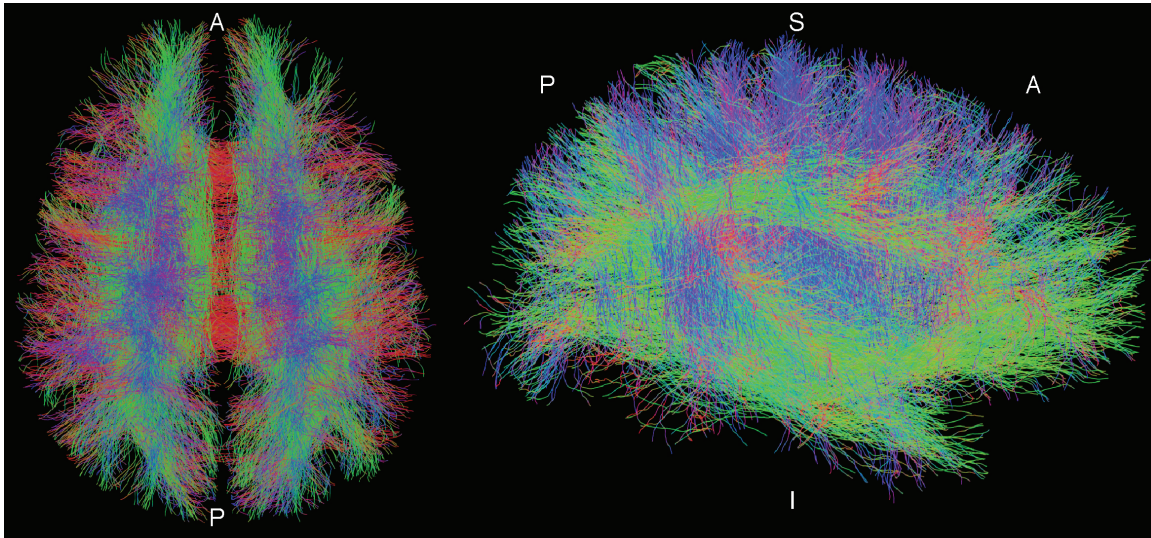
Figure 1.9: An example tractogram. Probabilistic CSD tractography performed in the cerebrum of a healthy control subject. Colour is determined by principal direction and follows the convention: *Red:* Left-Right, *Green:* Anterior-Posterior, *Blue:* Inferior-Superior.

In recent years the variety and performance of fiber tractography approaches has increased dramatically. In a tractography competition known as the Fiber Cup, global tractography [40] performed best overall, followed by constrained spherical deconvolution. The ground truth phantom used in the Fiber Cup is shown in Figure 1.10 alongside the results from the top-performing global and CSD tracking algorithms. More recent (and ongoing) tracking competitions such as the Tractometer [41] and Fiberfox [42] both report[3] that CSD approaches are the top performers.

When working with patients that present with local lesions, for example in MS or traumatic brain injury (TBI), an open question is how to proceed in regions of pathologically damaged white matter. The issue is that diffusion models fit to damaged tissue (e.g. in a region afflicted by gliosis) may be woefully inaccurate, and tracks suggested to pass through these voxels may not reflect the underlying biological structure. Furthermore, when using calibration-based methods (like CSD), the single-fiber response values may not apply to damaged regions, leading to further errors when resolving fiber orientation distributions.

---

[3]As of April 23rd, 2014
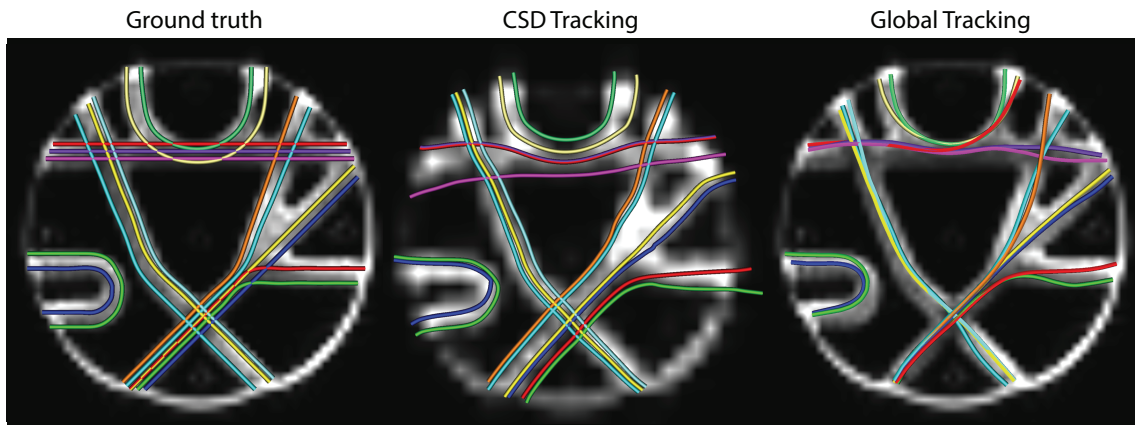
Figure 1.10: Tractography algorithm comparison in a phantom. The Fiber Cup [35] phantom ground truth fibers were reconstructed using various tractography algorithms. The two best performers were global tracking [40] and constrained spherical deconvolution.

One recent study of patients with multiple sclerosis (MS) took special measures to track through both the normal-appearing white matter [43] and the lesioned areas, citing the need to reduce "false negatives" in the tractogram. The study in question used deterministic tensor tractography and therefore did not have to deal with CSD calibration issues. Nevertheless, it is still inadvisable to perform fiber tractography through lesioned areas. Studies should prevent tracks from entering hypointense WM areas in T1-weighted MR images, as well as areas demarcated by subject-specific lesion masks. An example of subject-specific lesion masking in MS using FLAIR images is shown in Figure 1.8.

Once tractography is complete the subsequent analysis steps depend on the goal of the study. Many types of analysis, such as evaluating structural connectivity, require the tracks to be aligned to another scan. This can be performed by obtaining a rigid, affine, or non-linear transformation between diffusion space and that of the target image. This is commonly done by registering the FA image to the target (e.g. T1)[4]. The transformation can then be applied to each point of every streamline in order to register the tractogram to the target image.

---

[4]In my experience the best coregistration results come from rigidly registering a thresholded binarized FA image to a binarized T1-derived white matter mask.

1.3 The Connectome

Representing the brain as a network, or *connectome* [44], allows researchers to quantitatively explore brain connectivity. In human neuroimaging, this approach began with diffusion-weighted imaging and is now prevalent in functional magnetic resonance imaging (fMRI) as well as EEG. Briefly, the approach defines regions of the brain as nodes in a network and uses measures of structural (or functional) connectivity to populate the edges. An example of a simple four-node network is shown in Figure 1.11. Network edges are commonly represented as diagonally symmetric square matrices. Diagonal elements can represent within-node measures of connectivity, though in structural connectivity analyses these are usually ignored.
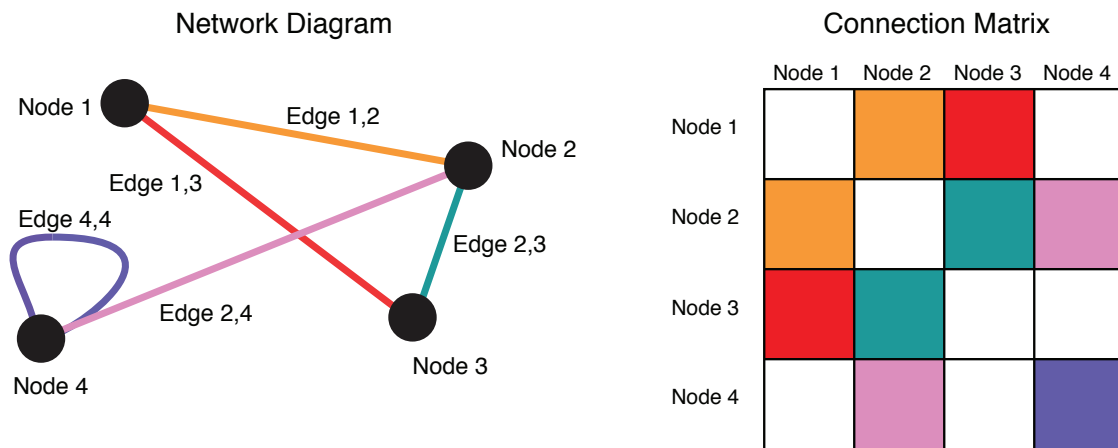
Figure 1.11: An example network. Networks are defined by their nodes and the edges connecting them. They can also be represented as diagonally symmetric square matrices, where the value at index x,y (and y,x) of the matrix corresponds to the edge weight.

The connectome concept is widespread in other areas of neurobiology; in the Caenorhabditis elegans worm, the network of its entire nervous system has been mapped, neuron by neuron[5]. More recently, the connectome of a standard lab mouse was fully traced at the cellular level [45].

1.3.1 Parcellation schemes

There are a multitude of approaches for defining the nodes of a connectome [46], but in general, nodes are defined structurally by segmenting the brain into re-

---

[5]An interactive version is available at http://www.openworm.org/

gions. This can be done, for example, through automated anatomical segmentation methods [47]. Freesurfer, which labels regions using borders on the gyri, is the current standard for this, though Klein & Tourville's Mindboggle package (`http://mindboggle.info/`) is an excellent new addition to the field [48]. Alternatively, it is possible to create connectomes in which each and every grey matter (GM) voxel is considered a distinct node, but this is much more computationally expensive. Regional parcellation schemes are the most common, but they have some caveats.

First, for the connectomes to be comparable across subjects in a study, the nodes must be anatomically and functionally equivalent. Second, for a weighted network to be studied using graph theory summary statistics, the regions must have approximately the same spatial dimensions. Without similar dimensions, or a subsequent edge-weight correction scheme, the network is implicitly biased toward large nodes. One commonly used parcellation scheme, shown in Figure 1.12, involves sub-dividing the anatomically defined regions of Freesurfer [47] into small, approximately equal-sized parcels[49, 50].

Another parcellation option is to randomly place equally sized parcels throughout the grey matter, and then interpret the results anatomically as with a voxelwise map. There are various drawbacks and benefits from each of type of parcellation scheme, but the general rule is that the parcellation must be adapted to the study population and research question. The parcellation schemes must also be sensible to use with the edge definition. For example, it would be odd to build an fMRI correlation matrix using large regions that are composed of unique functional areas. Likewise, it's inadvisable to build structural connectomes with regions made up of only a handful of voxels, since so few tracks will reach each region that edge values will be too unreliable.

Building the connectome itself can be done in either subject space or in a common template space. Subject space is preferable because regions can be more accurately defined using the subject's own anatomical image. Constructing connectomes by warping an atlas to the subject's T1, or alternatively, by warping the tracks to the space of an atlas has the downside that errors can be introduced during warping. The thickness of the grey matter in a human brain generally ranges from 1 to 4.5 millimetres [51]. Since network connections are typically defined by tracks crossing or terminating in grey matter regions, this means that the (usually non-linear) subject-to-template transformations must be very accurate[6].

---

[6]See [52] for an evaluation of various non-linear deformation algorithms

Lausanne 2008 Atlas Parcellations

Freesurfer Desikan-Killiany
Automated Segmentation

120 regions

250 regions

83 regions

500 regions

1015 regions
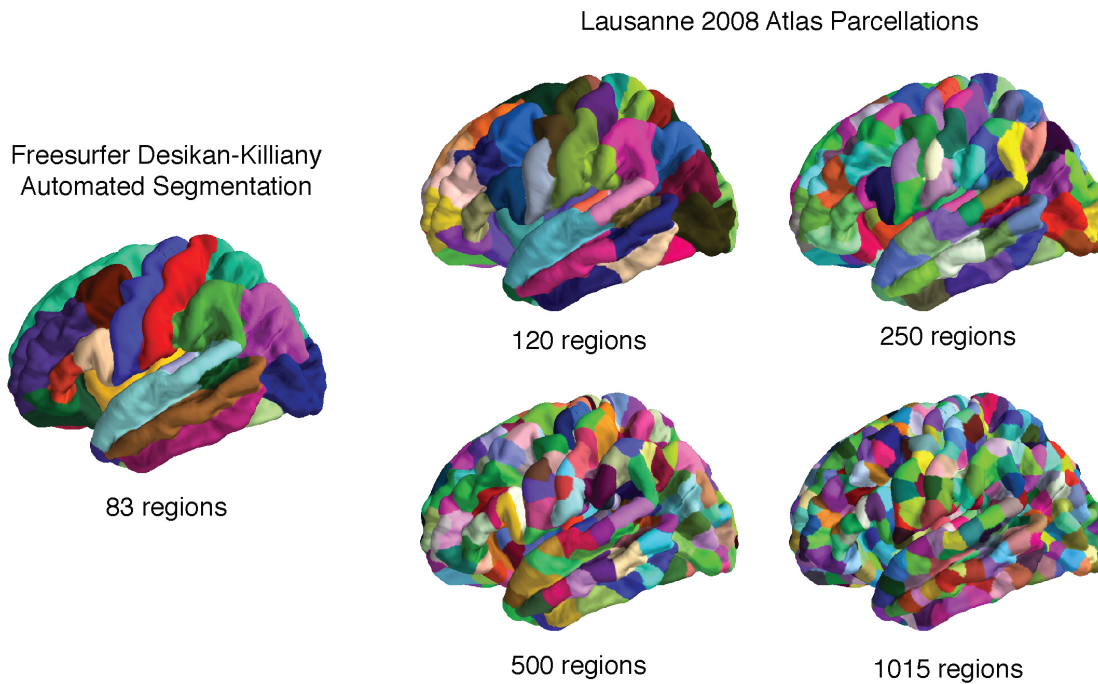
Figure 1.12: Example of structural parcellation schemes. Example showing the Desikan-Kiliany automatic segmentation applied to the Freesurfer average brain. Finer parcellated regions of the Lausanne 2008 atlas are shown on the right [49, 50].

The number of nodes has a substantial effect on the properties of the connectome, which further complicates interpretation of network-level neuroimaging studies [46]. A recent and interesting development is the introduction of functionally defined (e.g. by fMRI) parcellation schemes for connectome construction [53].

1.3.2   Edge weights

The next question when building a connectome is how to define the edges. The classic measure is a simple sum of the number of fiber tracks beginning in one region and terminating in another. It is common to normalize the number of fiber tracks between regions in order to remove confounding factors such as brain volume or region size. The fiber counts can be normalized by the total number of fiber tracks in the subject's tractogram, for example, and/or by the sum of the volumes of the regions that the edge connects. Many recent studies have opted to calculate "along tract statistics" in order to avoid normalization issues[7] [54]. These studies calculate the FA or MD for all voxels that each track passes through, and sums these values

---

[7]There is a nice open-source MATLAB library for this at `https://github.com/johncolby/along-tract-stats`

to calculate the edge weight. The main issue with this method is that edges within each network are no longer directly comparable, since some brain regions naturally show larger FA than others. A number of studies have binarized their connection matrices prior to analysis, whereas others have opted to analyze the network using multiple edge weight thresholds. There is currently no consensus regarding the most appropriate edge-weighting method. An example connectome for a single healthy subject is shown in Figure 1.13.
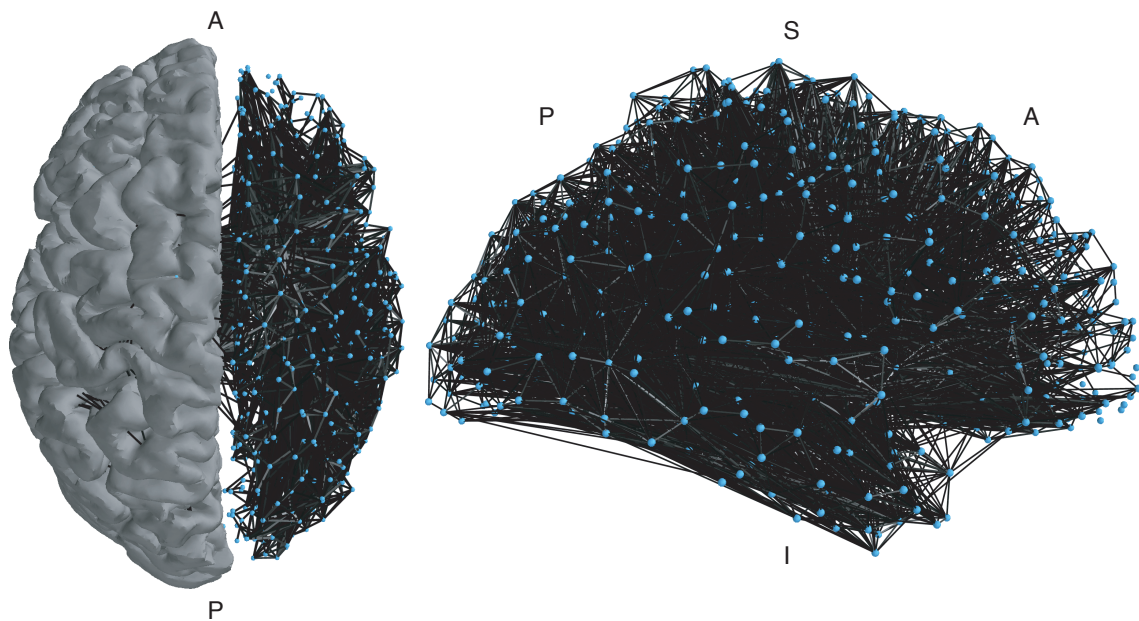
Figure 1.13: An example connectome. The figure shows axial and sagittal views of an example connectome. In the axial view, the grey matter surface is also shown for reference. The connectome was built using CSD, probabilistic tractography, and the 1015-region Lausanne 2008 atlas. Nodes are shown in blue and edges in greyscale, with darker edges representing stronger connections. Edges are weighted by the number of fibers connecting each node. A = Anterior, P = Posterior, S = Superior, I = Inferior.

1.4   Network analysis

Network analysis with fine-grained connectomes is complex. Direct comparison of edge weights is inadvisable due to the enormous number of comparisons required. As an example, consider that a connectome with 1000 regions will have 499,500

unique connections to assess[8]. Statistical correction schemes for multiple comparisons (e.g. Bonferroni correction) are overly conservative in this scenario.

For this reason researchers turn to network summary statistics. These summarize networks using measures from graph theory that describe the topological qualities of their connective structure. Several common network measures, such as nodal degree and centrality measures are explained in Figures 1.14 and 1.15. Network efficiency, shown in Figure 1.16, describes the ease of communication within a network, and reflects the "cost" for each node to communicate with all others. Many graph measures are computed on the nodal level, whereas others are computed for the network as a whole (i.e. globally). One of the most comprehensive graph analysis libraries is NetworkX [55], which we have used in Paper I.

Global network measures, however, can be insensitive to large changes to brain structure. A recent functional connectivity study reported that patients with severe brain damage showed global network measures that did not significantly differ from healthy controls [56]. Local network measures are therefore preferable for neuroimaging studies. Connectomes are, in general, not comparable between studies due to the various processing options chosen during network construction. For an evaluation of the influence of tractography algorithms on structural connectome reconstruction, the reader is referred to [57].

There are alternative methods for identifying between-group differences in connectivity matrices that do not involve graph theoretical measures. One such non-parametric method is the network-based statistic (NBS) [58], which operates similarly to statistical parametric mapping (SPM), and was used in Paper I (Appendix A). The NBS aims to control the family-wise error-rate (FWE) by assessing the statistical significance of clusters of supra-threshold edges. First, two-sample t-tests are performed between edge weights at every link for the two groups being compared. Next, these t-statistics are thresholded and a breadth-first search is performed to identify supra-threshold "components", which are the network equivalent of connected voxel clusters. The number of edges (or "size") of each component is stored for later. This procedure is repeated numerous times while permuting the group to which each subject belongs. The set of permutations are used to construct a distribution of maximum component sizes and estimate p-values for each link. The user-defined t-statistic threshold has a substantial influence on the extent of the identified results, and it is therefore common to evaluate various thresholds.

---

[8]$(n * (n - 1))/2 = (1000 * 999)/2 = 499,500$
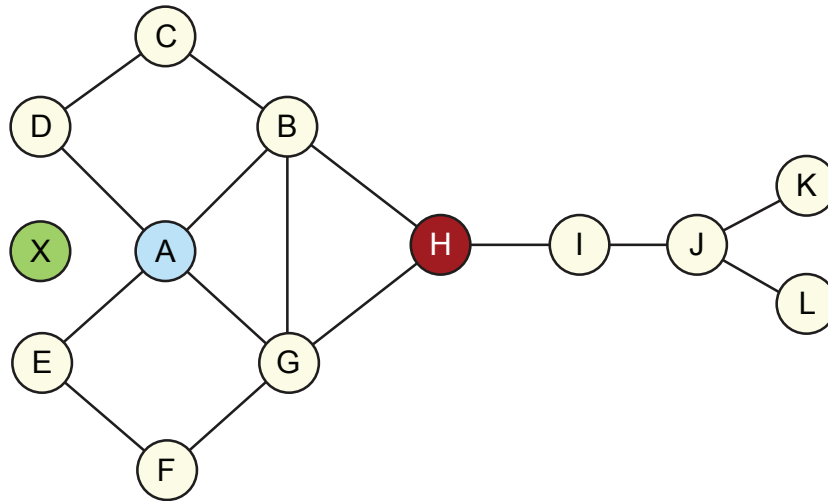
X is an isolated node with degree = 0

A has degree = 4 and high degree centrality

H has high betweenness centrality, as it plays a broker role

A clique is a group in which all nodes are connected to each other.
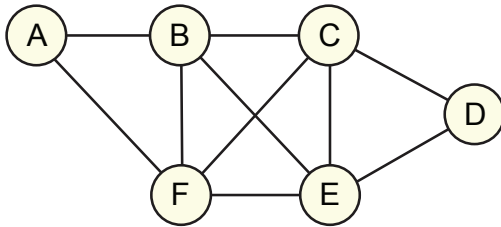
A simple example network
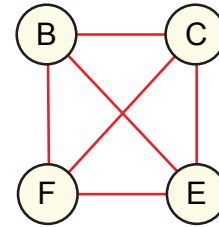
The largest (or maximal) clique

$$\text{Graph density} = \frac{\text{number of present connections}}{\text{number of possible connections}}$$
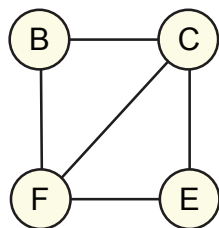
Four nodes: n = 4

Possible connections: n*(n-1) / 2 = 6

Graph density is 5 / 6

Figure 1.14: Nodal degree & centrality, cliques, and graph density.

Node strength is the sum of the edge weights connected to a node
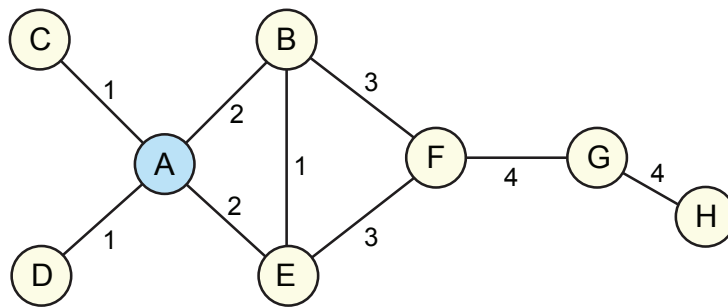
A simple example network with edge weights

A has strength = 1 + 1 + 2 + 2 = 6

Clustering describes how connected a node's neighbours are to each other
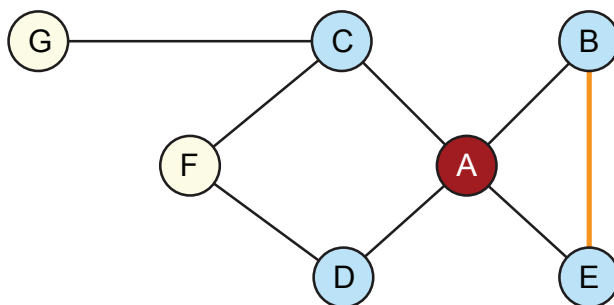
Blue nodes are neighbours of A

There are 4 nodes with 1 connection between them, in orange

The clustering coefficient of A is $\dfrac{1}{(4 * (4\text{-}1) / 2)}$ = $\dfrac{1 \text{ present connection}}{6 \text{ possible connections}}$

Figure 1.15: Node strength and clustering.

Path length is the distance from one node to another
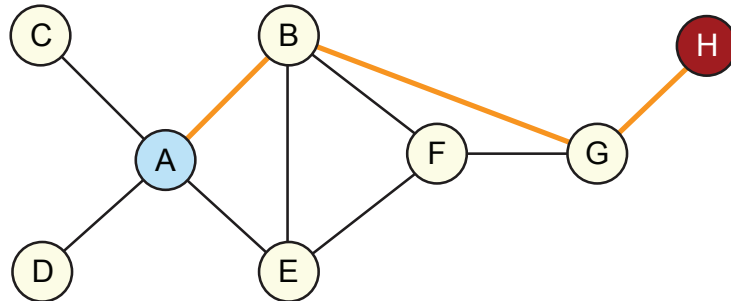
The shortest path length between (A) and (H) is 3 edges, shown in orange

Characteristic path length is the average path length to all other nodes

(A) has a characteristic path length of $\dfrac{1+1+1+1+2+2+3}{7 \text{ nodes}} = 1.57$

Figure 1.16: Characteristic path length.
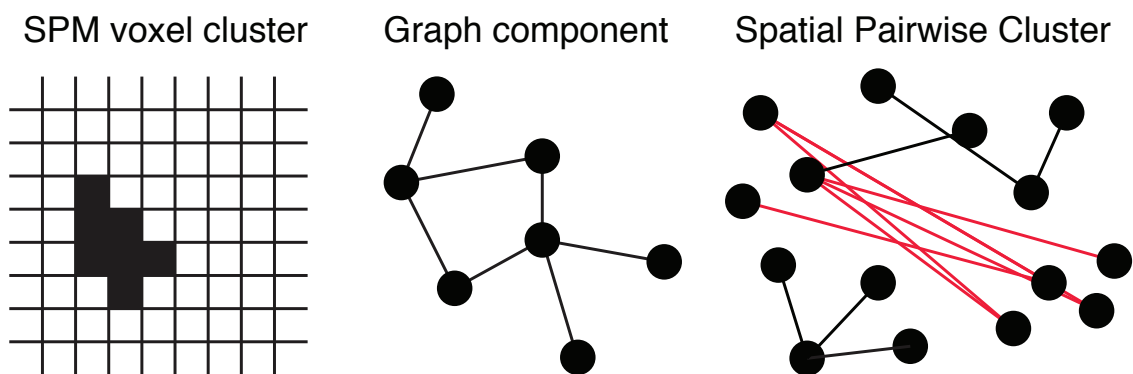
Figure 1.17: Statistical network comparison methods. Graph components identified by the Network-Based Statistic (NBS) are analogous to Statistical Parametric Mapping (SPM) voxel clusters. An alternative method for statistical testing is to assess pairwise clusters of nodes. Connections that would be identified by spatial pairwise clustering (SPC) are shown in red.

Another method, known as spatial pairwise clustering [59, 60], can also be used to identify region-to-region connective structures that the NBS may inadvertently aggregate into a single component. Figure 1.17 shows an example of an SPM voxel cluster, an NBS graph component, and a set of nodes involved in a spatial pairwise cluster.

1.5   Track quantification

Fiber track quantification is a logical extension upon high-resolution tractography methods. Put simply, if the fibers produced by the tractography model accurately represent white matter pathways, then sampling their properties on a grid can provide a volumetric image worthy of analysis. Using this premise the researcher is open to develop novel track-weighting methods.

The most basic track quantification method is known as track density imaging (TDI), in which the modelled fibers are counted within voxels of a newly imposed grid [61]. Intriguingly, the borders of the white matter can be accurately represented by this method down to sub-millimetre levels using standard DWI acquisitions [62]. The resolution obtained by track density imaging can be higher than that of the original acquisition (i.e. super-resolution imaging). The super-resolution quality of track-weighted imaging comes from the added information obtained by tracking the neural pathways. In another track-weighted imaging method, known as average pathlength mapping (APM), the signal represents the mean length of the tracks that pass through each voxel [63, 64]. A schematic illustrating the track-weighted imaging method is shown in Figure 1.18.

Several whole-brain maps are shown in Figure 1.19 to compare the resolution obtained by typical tensor-derived measures and that of track-weighted imaging. It is important to note that although the TDI and the FA maps look similar, they offer different contrasts and cannot be interpreted equivalently. As shown in Figure 1.19, colour mapping by directional encoding of track direction in each voxel also allows TDI maps to be created with false colour, similar to RGB-FA maps.

The track-weighted imaging framework has been extended to produce a number of interesting image contrasts [63, 65–67]. In these methods, a scalar map (e.g. the FA map, or a scalar map of functional connectivity) is first sampled at each point of each streamline. The method of sampling the scalar map for each streamline is user-definable (e.g. a sum across all track points, mean value for the entire track, or a more complex operation). The tracks are then regularized, as before, by imposing
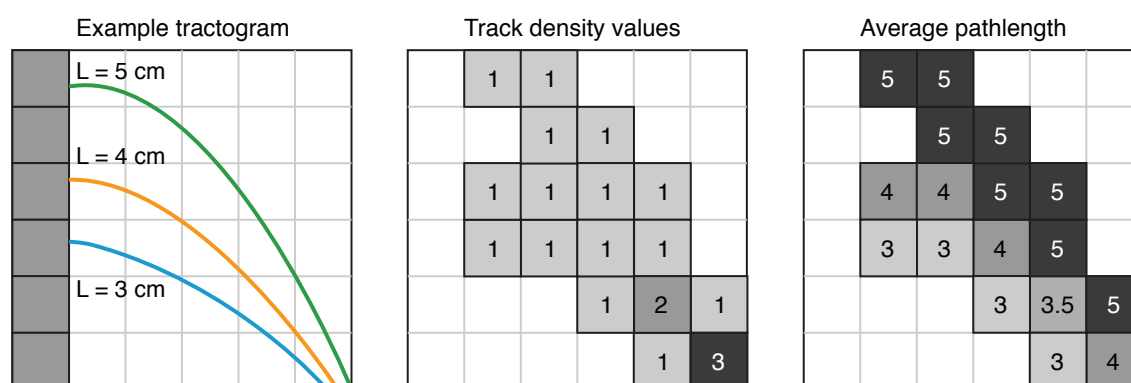
Figure 1.18: Schematic of track-weighted imaging. In track-weighted imaging, the fiber tractogram is quantified on a user-defined grid. The left panel shows an example tractogram with three fibers of varying length (L). The track density values in each newly created voxel are shown in the center. Average track length (often referred to as pathlength [64]) values are shown on the right. Given a sufficient quantity of realistic streamlines, the imposed track density grid can provide higher resolution than the original scan (i.e. super-resolution imaging).

a grid. Finally, a second within-voxel mathematical operation is performed over all the tracks passing through the voxel. Distance-weighted track quantification images, in which the fiber distance from a marked point (e.g. a tumour) modulates the signal during track quantification, have also been demonstrated [67]. Since track-weighted imaging is inherently non-local, the values at each voxel can be hugely biased by local changes. Results are smoothed across the entire path of all the tracks that pass through these voxels. It is especially important, then, that potential artifacts are removed and that poor quality scans are not used because modelling errors propagate throughout the brain, unlike in other methods[9].

It is clear that using this framework an enormous amount of novel image contrasts can be developed. It is unclear, though, if they can be made to reflect biological properties that are interpretable to neuroscientists or clinicians. At the very least, these contrasts will be interesting for the visualization and localization of abnormal white matter pathways.

1.6 Diffusion imaging artifacts

Because of the complexity of DWI acquisitions there are a number of artifacts that are commonly encountered.

---

[9]e.g. in voxel-based analysis of fractional anisotropy, errors remain local
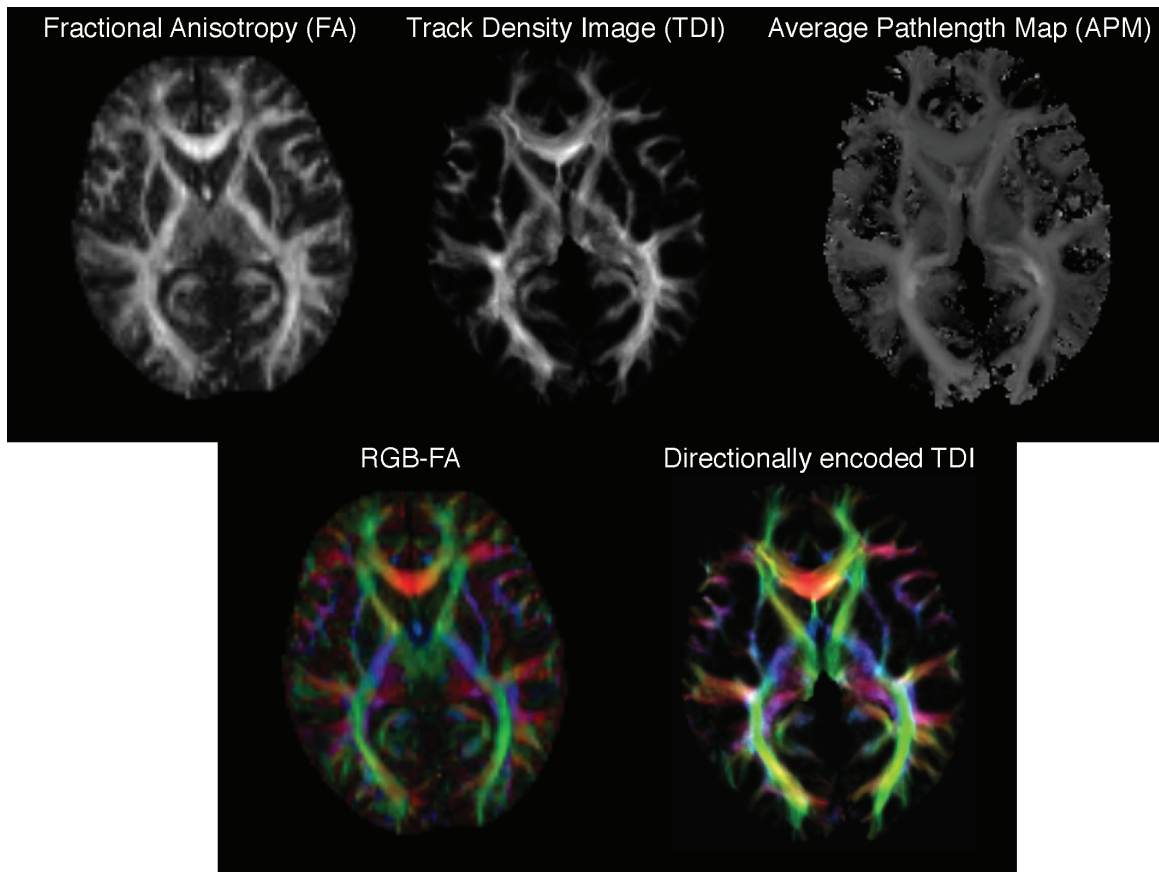
Figure 1.19: Examples of track-weighted imaging. A track density image (TDI) is shown next to a fractional anisotropy image in order to demonstrate the improved resolution possible with TDI. Contrast is also improved in the directionally encoded TDI (DEC-TDI) compared to the RGB-FA image. The average pathlength map (APM) shows that the longest tracks in this subject's brain are in projections to the occipital cortex. TDI images were created with 1 million tracks and 1 mm^3 isotropic voxels, whereas FA images had the original scan resolution (1.8 x 1.8 x 3.3 mm^3). Data from CHU Liège.

Artifacts from subject movement between acquired volumes are common and usually alleviated by rigid realignment to an unweighted (b = 0) volume [4]. When this is performed, the associated b-vectors must be rotated using the applied transformation matrices [68]. A recent study has demonstrated the effect of motion in DWI and recommends that an index of subject motion is kept as a nuisance covariate for later analyses [69].

The cycling of strong gradient pulses frequently induces eddy currents in various parts of the MR scanner [4]. These eddy currents create magnetic fields which distort the acquired images. These shear-like distortions can be alleviated by performing affine transformations between the weighted volumes and an unweighted volume. It has been suggested that the DWI signal must be modulated after affine transformation to correct for the volumetric changes [70], though software packages largely ignore this step. Eddy current-induced distortions can also be avoided by using specially designed DWI sequences. In Paper II, we used a sequence which included a second refocusing pulse and adjusted gradient timing in order to nullify eddy currents [71].

A further nefarious artifact can be induced by table vibration in certain scanners (e.g. Siemens TIM Trio) and manifests as augmented diffusion along a specific direction (usually the x-direction; left-to-right within the head)[72, 73]. These artifacts are practically impossible to remove post-acquisition unless a distinct dataset was acquired with phase encoding reversed [73]. Researchers are forced to either manually mask the artifact and attempt to regress out its effect during tensor fitting [72], or to remove volumes acquired with a large x-component in the gradient direction. The former is unreliable and ineffective and has not yet been extended to models of higher order than tensors. The latter has dramatic effects on the signal-to-noise ratio of the data, and appears to only slightly reduce the effect of the artifact.

Compounding on these issues, DWI is also affected by routine MRI artifacts, such as spatial bias in the strength of the magnetic field and slice or volume drop-out [4]. Plotting a map of the residual values obtained during tensor fitting is an easy way to quickly identify artifacts in DWI datasets [3]. At higher b values (b > 2000 s/mm^2) there is a lower signal-to-noise ratio making both motion and eddy currents more difficult to correct. For this reason, specialized post-processing techniques [74] have been developed to correct high b value DWI acquisitions.

For more information, the reader is directed towards a seminal review of the diffusion field, which describes in detail the best approaches for identifying and dealing with these artifacts [3].

1.7   The future of diffusion imaging

The DWI methods described here represent only one portion of the research into diffusion MR imaging and there are a wide variety of alternative analysis methods under development. For example, studies are beginning to incorporate improved registration schemes, in which tensors or FODs are used directly for registration and/or normalization [75]. Direct voxelwise comparison of FOD functions has recently been demonstrated [76] and significant regional and orientation-specific differences were identified in patients with motor neuron disease. Tensor registration methods in which anisotropy is conserved [77] may also be useful in multimodal studies, such as in the forward modelling study described in Chapter 5.

Another interesting method is DKI, in which the kurtosis (i.e. non-Gaussianity) is estimated from the diffusion probability distribution. This is only possible at high b values, where the tensor model of diffusion is no longer valid. Kurtosis-derived measures are considered to be sensitive to cellular microstructure, which may make this an interesting clinical imaging method. Although some promising results have been obtained (e.g. in Parkinson's disease [78]), DKI is still in its early stages, and is still plagued by artifacts [79].

A further class of methods is focused on axon diameter and density estimation. Methods like AxCaliber [80, 81] and ActiveAx [82] use novel acquisition sequences and complex models of intra-voxel diffusion [83] to approximate axon diameter distributions within each voxel. These methods have been validated *ex vivo* through comparison with histology and have enormous potential. Unfortunately, their use is hampered by long acquisition times (e.g. ActiveAx takes 1 hour of acquisition [82]).

Although many researchers wish to study specific biological tracts, it is quite difficult to objectively identify which streamlines belong to these tracts. Solving this problem is a goal of several recent packages for streamline clustering (or "bundling") using atlas-based [84, 85] and atlas-free [86] algorithms. These approaches may help simplify the visualization of large track datasets and clarify the biological relevance of network analysis results.

The move towards high-field MR imaging (e.g. at 7 Tesla or above) will bring great advances in structural mapping of the brain. A recent DWI acquisition at 7 T was carried out with using 60 gradient directions, 7 unweighted images, and 800 μm isotropic voxels, though it took a full hour [87]. An even more powerful study of the brainstem at 11.7 T produced outstanding images detailing fiber pathways unresolvable on typical clinical scanners [88] (see Figure 1.20).

High-field DWI Scan of the Brainstem (11.7 T)

Typical Clinical Scan (3 T)
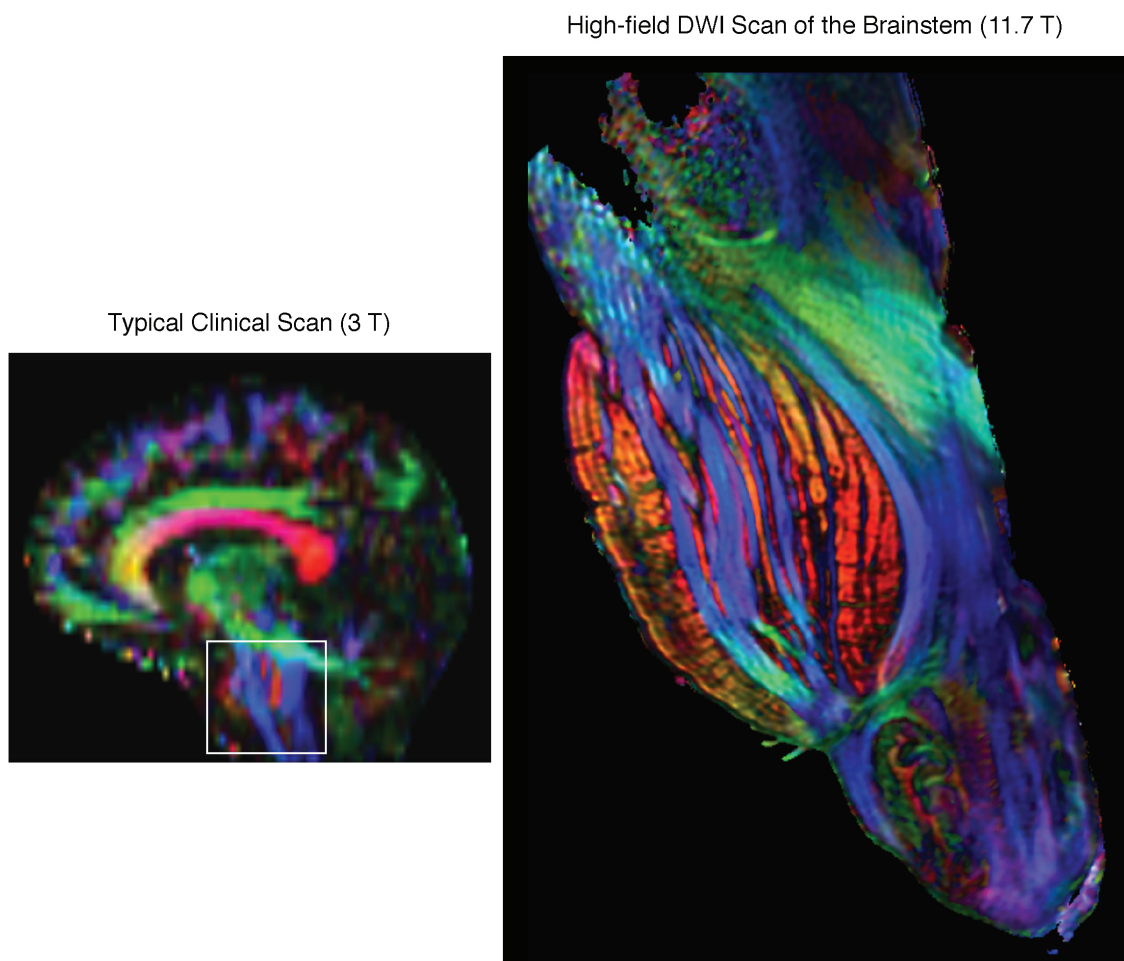
Figure 1.20: High-field diffusion imaging. Data for the image on the left comes from CHU Liège. Data for the image on the right comes from [88].

One development which appeared to be imminent in the past was diffusion-weighted functional magnetic resonance imaging (DfMRI) [89]. This acquisition strategy has revealed that there is an earlier response than the hemodynamic flow of blood to areas of neural activation [90]. This response is observed in DfMRI as a decrease in water mobility and is thought to reflect the biological mechanisms of cell swelling and membrane expansion that accompany neuronal activation. While DfMRI has not gained wide acceptance (or even name recognition) yet, it is a technique worth watching.

Electroencephalography

Electroencephalography (EEG) is a technique for the direct recording of electrical activity in the brain through a set of electrodes placed on the scalp. A basic problem that is addressed in Paper III is linking neuronal source activity in the brain to the acquired scalp recordings. This chapter provides an introduction for readers unfamiliar with EEG and/or the forward and inverse problems of source localization.

2.1 Signal & analysis

Electrical activity was first recorded on the human scalp nearly a century ago [91]. The biological origin of the EEG signal is complex and has multiple components. For an in-depth review into neuronal polarization and EEG in general, the reader is referred to [92].

Excitatory and inhibitory post-synaptic potentials at pyramidal neurons in the cortex are thought to be the primary contributors to the EEG signal. The human cerebral cortex is organized in a six-layered structure with specific cell types and connections in each sheet. Layer IV houses substantial amounts of pyramidal neurons with multiple dendrites extending from the cell body (or *soma*). Dendrites (or branches) extending from the apex of the soma are known as apical dendrites. These are particularly interesting features because of their orientation; they are generally perpendicular to the cortical surface. This directly influences the signals detectable from neural source imaging methods such as EEG and its magnetic counterpart, magnetoencephalography (MEG). MEG records magnetic fields in the brain and offers complementary information to EEG. It is a more complex, expensive, and rare technique because it relies on extraordinarily sensitive magnetometers.

A compartmental modelling study attempting to estimate the contribution of four types of cortical neurons concluded that the magnitude of the intracellular

current in a single pyramidal neuron is on the order of 0.29-0.90 picoamperes (pA) [93]. The current field detectable by MEG in the human cortex is roughly 10 nanoamperes (nA). This implies that there are tens of thousands of synchronously active neurons contributing to this signal [94]. Similarly, the EEG signal is thought to reflect thousands of neurons' synchronous activity.

In practice, EEG provides enormous quantities of data. The recording frequency is generally in the thousands of Hertz, and there are usually at least 32 electrodes on the scalp in research environments. For readers unfamiliar with the technique, a schematic of an EEG experiment is shown in Figure 2.1.
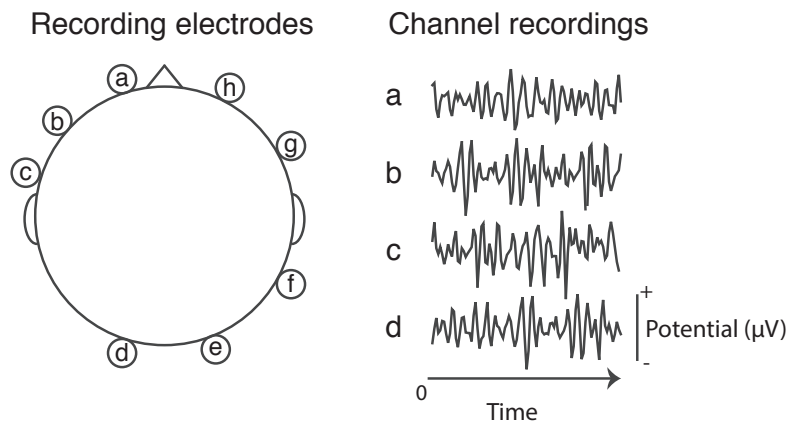
Figure 2.1: Schematic of electroencephalography (EEG). In EEG, electrical potentials are recorded over time through sensors placed on the scalp. Each sensor is treated as a distinct recording channel. The sensor potentials are generally recorded relative to a reference electrode or set of averaged sensors. The choice of reference type is known as a montage. The number of sensors placed on the scalp is generally below 256. Typical recording frequencies in EEG are on the order of 2000 Hz. Signals are usually on the order of microvolts (μV).

Once the signal is acquired the voltage values at each channel can be re-referenced to another sensor or a combination of sensors. The next steps involve cleaning artifacts such as eye blinks and eye movement from the signal, bandpass filtering to remove high-frequency noise and low-frequency drifts, and bandstop filtering to remove 50 Hz line noise.

There are a wide variety of approaches to analyze EEG data. Depending on the design and the goal of the study, signals may be averaged across numerous trials so that event-related potential spikes and troughs can be analyzed. Time-frequency analysis can be used to study event-related (de)synchronization. Blind

source separation is also frequently used to decompose the signal. Causal analysis and modelling methods (e.g. Granger causality, dynamic causal modelling) can be applied as well.

A common goal, known as source localization, is to identify the origin of signals within the head. There are a variety of software packages used for EEG/MEG analysis, such as FieldTrip [95], EEGLAB [96, 97], SPM [98], MNE [99, 100], and FASST [101]. These toolboxes do not all implement their own source localization tools, but tend to rely on those implemented in SPM, MNE, NFT [102], and OpenMEEG [103].

2.2   Source localization

Reconstructing the source of neural activity requires a number of key assumptions. The first, which is well established, is that a neural source can be approximated as an equivalent current dipole [104]. Next, a model must be chosen to approximate the geometry of the subject's head as well as the position of the electrodes. EEG electrode placement follows standard systems which makes them easy to approximate[1] given the position of the nasion, inion, and both pre-auricular points. Head models can be generated in various ways from structural (e.g. T1) MRI scans. Optimally, the electrode positions are marked using a digitization system[2] [105]. Once the head model is built, the next step is to construct a leadfield matrix to relate voltage values on the scalp with current sources in the brain. Constructing the leadfield is known as the *forward problem*.

2.2.1   The forward problem

The standard (or "direct") method for creating the leadfield matrix is to place a large number of test dipoles inside the grey matter, oriented outwards, in order to approximate neural populations. This constraint is imposed because the primary source of recorded EEG signals, as mentioned above, is thought to be pyramidal neurons [106]. Each column of the leadfield matrix then represents the potential calculated on the scalp from each dipole individually. An example of a set of leadfield dipoles (calculated using MNE) is shown in Figure 2.2. The number of dipoles (or "source positions") calculated influences the usability of the leadfield matrix. This leadfield mapping procedure is shown schematically in Figure 2.3.

---

[1]e.g. using a sphere
[2]e.g. using electromagnetic receivers, ultrasound transmitters, or digital cameras
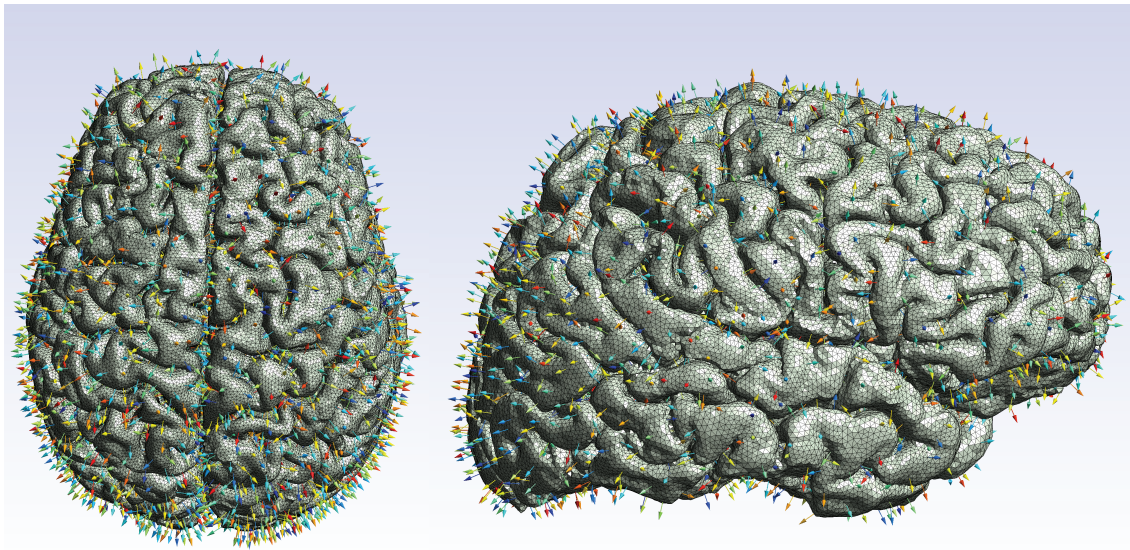
Figure 2.2: Example dipoles for the direct method of leadfield creation.
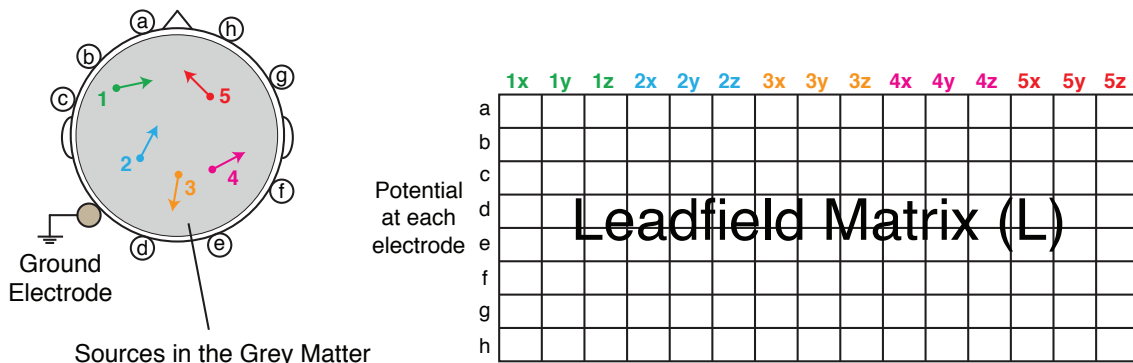
Leadfield is built three columns per iteration, until all dipoles have been simulated

Figure 2.3: Schematic of the direct method of leadfield creation.

Naturally, accurate leadfield matrices are required to reliably localize source activity. This means that large numbers of dipoles must be simulated. This approach is commonly used in boundary element modelling (BEM), where the head is defined by a set of (usually concentric) two-dimensional meshes, and each compartment's conductivity is uniform and isotropic. It is more difficult in finite element modelling (FEM), where the head is defined with a three-dimensional volumetric mesh. The main benefits of using FEM over BEM are the ability to include additional element-

wise information[3], and the relative ease involved in modelling complex geometries[4].

In Figure 2.4, we demonstrate an alternative method for constructing the leadfield matrix. Instead of simulating current sources at numerous potential source locations, the leadfield is built row-by-row by applying current at each sensor and computing the electric field induced in each element of the FEM mesh. This is known as the reciprocal approach, as it is derived from Helmholtz's principle of reciprocity [107, 108].
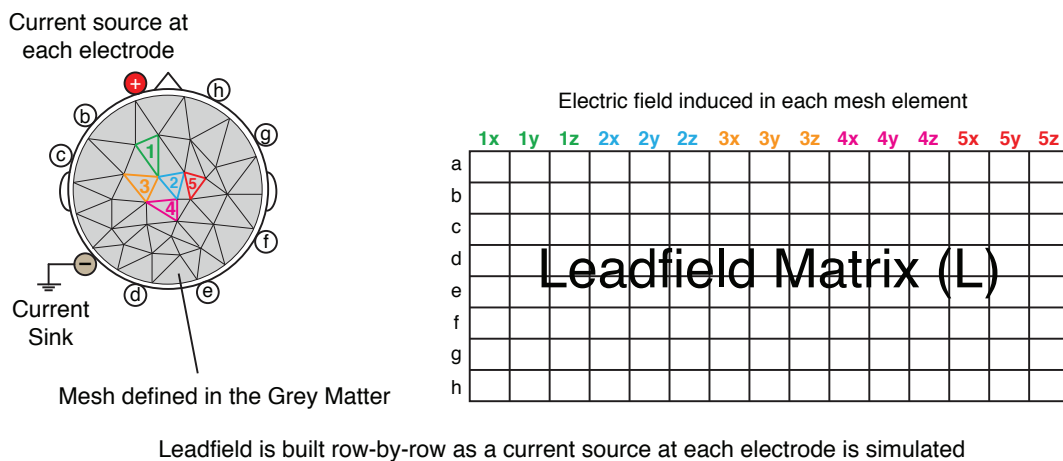
Figure 2.4: Schematic of the reciprocity method of leadfield creation.

Next, using the leadfield, algorithms are used to estimate the most likely configuration of sources that could produce the known scalp voltage profile. Creative strategies for performing this optimization are said to solve the *inverse problem* [107].

2.2.2 The inverse problem

Because EEG depends on volume conduction there is always a degree of crosstalk between electrodes, and each measurement cannot be considered independent. Furthermore, due to the characteristic folding for the cortex, signals detected at any single electrode cannot be assumed to originate from nearby patches of cortex. Inverse approaches must therefore be capable of efficiently searching the entire grey matter.

---

[3]e.g. conductivity tensors derived from diffusion-weighted imaging
[4]e.g. a skull with a hole in it

The inverse problem is analytically ill-posed, meaning that there is no unique correct solution. Algorithms must attempt to find the best possible solution given the data and adopted model. In inverse approaches, the model refers to the number and type (e.g. varying orientation and/or amplitude and/or position) of dipoles that the algorithm will try to fit. Briefly, inverse solutions can be divided into two categories: parametric, in which the locations of one or more dipoles are estimated, and non-parametric, in which dipole locations are fixed and their amplitude and orientation are estimated.

Parametric approaches, often called equivalent current dipole methods, may test systems of single and/or multiple spatially distinct current dipoles [109]. These approaches are overdetermined ($p < M$), as the number of sources (p) is less than the number of electrodes (M). In these approaches, an optimization procedure repeatedly tests head locations to identify the most likely coordinates, orientation, and strength of sources.

Non-parametric methods for inverse localization are often called distributed inverse solutions. These are linear problems in which the goal is to estimate the dipole magnitude matrix which best explains the signal. Since they aim to adequately model the entire brain (or grey matter), there are typically far more sources than scalp electrodes ($p >> M$), making the problem underdetermined.

Several basic anatomical assumptions can be used to reduce the solution space to simplify this problem. First, source dipoles are expected to originate in the grey matter, a mask of which is normally segmented from a T1-weighted MR image. Next, it is assumed that all dipoles have perpendicular orientations to the cortical sheet. Finally, constraints can be placed on the spatial coherence of the dipoles; some groups of regions may act in concert with one another, and these groups should be assumed to be nearby and oriented similarly. As an example, a group of dipoles located on a single gyrus would be considered spatially coherent, whereas two dipoles placed on opposite sides of a sulcus would not [110]. Bayesian inference can be used to estimate the conditional expectation of source configurations, and can take multimodal or user-defined constraints into account [111, 112]. A further common approach is to estimate spatial priors for source reconstruction from fMRI studies of the same task [113, 114]. One study used fMRI networks derived from independent component analysis as the covariance priors for the Parametric Empirical Bayesian approach to source reconstruction [115]. These ongoing temporally coherent blood flow patterns are usually studied using resting-state functional MRI scans and are

constantly present in the brain. The coupling between hemodynamic and electro-magnetic signals in the brain is unclear though and priors derived from functional neuroimaging must be considered probabilistic. Furthermore, the effect of spatial priors is dependent on the data in question. Strong accurate spatial priors may not improve recovery of the sources, but rather reduce the number of spuriously identified sources [110].

Unlike forward models, which can be constructed without knowledge of the study design, the inverse approach must be chosen carefully by the researcher. For a review of a vast array of inverse modelling approaches, the reader is referred to [116].

Connectomes and genetics

Genetic control over the human connectome is present at both the structural and functional level [117, 118]. Researchers aim to disentangle variance in biological traits into their additive genetic, shared environmental, and/or unique environmental components. One method for doing this is studying monozygotic and diyzgotic twins, for example, using structural equation modelling [119–121]. When twins are not available, genetically associated traits can be identified by studying highly similar population cohorts with known genetic variations. In Paper I (see Appendix A) we examined the structural connectivity of two groups with single nucleotide polymorphisms in two genes: *BDNF* and *ADA*. The study was composed of 36 healthy subjects aged 18-26. These subjects were selected based on a variety of sleep quality, chronotype, and lifestyle characteristics, as they were part of a rigorously controlled multimodal study of the genetic influences on sleep.

3.1   Background

3.1.1   Brain-derived neurotrophic factor (BDNF)

Brain-derived neurotrophic factor (BDNF) is a widely abundant neurotrophin whose activity-dependent release is essential for healthy development of the central nervous system. Outside of the brain it is also remarkably distributed in other organs, such as the skin, bladder, lung, and colon, which may signal an involvement with sensory and motor neurons [122]. BDNF is stored in axon terminals [123], promotes dendritic growth [124], and regulates long-term potentiation at excitatory glutamatergic synapses [125]. Because of its widespread distribution in the brain there are a vast amount of studies of the *BDNF* gene and its link to cognitive function and disease susceptibility, as well as both *in vivo* and *in vitro* studies of the protein's effects.

Animal and cell culture studies have identified that a common single-nucleotide polymorphism in the *BDNF* gene (G > A at nucleotide 196), known as Val66Met (dbSNP: rs6265), reduces the activity-dependent release of the BDNF protein, hampering axonal pruning and maintenance [126, 127]. Although most polymorphisms have small overall effect sizes [118], the effects of this specific polymorphism have been detected in macroscale analyses several times [128].

In one such study, the reduced secretion of BDNF in subjects with the Val66Met polymorphism was linked to alterations in experience-dependent plasticity in the motor cortex [129]. The Val66Met polymorphism has been suggested to confer susceptibility to both major depressive disorder and Alzheimer's disease. For a comprehensive review, see [128]. Its presence in the human population varies from 0.55% in Sub- Saharan Africa, to 19.9% in Europe, and 43.6% in Asia [130].

A subset of the cohort in Paper I was recently used to examine the effect of long-term potentiation on sleep-dependent memory consolidation mechanisms [131]. Overnight memory consolidation was found to be worse in the Val66Met group. As in previous studies [129], this is expected because subjects with the Val66Met polymorphism release less BDNF during memory encoding tasks.

3.1.2 Adenosine deaminase (ADA)

Slow oscillatory (< 5 Hz) activity is prominent in the recorded EEG during human non-rapid eye-movement (non-REM) sleep. These slow waves are thought to reflect synaptic plasticity at work. Their duration and intensity are driven by sleep need (i.e. homeostatically regulated) and modulated by subjects' circadian rhythms [132]. Furthermore, the quality of slow-wave sleep is considered a heritable trait. The neurotransmitter interactions that influence slow wave activity are not well understood, though the neuromodulatory agent adenosine may contribute to maintaining sleep homeostasis.

One important metabolic enzyme for adenosine is known as adenosine deaminase (ADA). A non-synonymous polymorphism (G > A at nucleotide 22, dbSNP: rs73598374) in its associated gene (*ADA*) has been reported to increase sleep pressure, subsequently lengthening non-REM sleep [133, 134].

3.2 Overview

Of the 36 subjects, 15 (9 male) were identified as carrying the Met allele at codon 66 of the *BDNF* gene. Of these 15, 12 had the rs6265 (Val66Met) single-nucleotide polymorphism, whereas the other 3 were homozygotic for the Met allele. The remaining 21 (9 male) were homozygotic for the Val allele, and are referred to as the ValVal group. Structural connectomes were created and used to compute a variety of (mostly edge-weighted) network summary metrics. Non-parametric statistical testing using the NBS [58] revealed one large and significantly different component between the connectomes of ValVal subjects and Met allele carriers.

Structural connectivity in Met allele carriers was found to be higher throughout the forebrain. Increases in edge weights were found in connections corresponding to the anterior and superior corona radiata. Inter-hemispheric connectivity was increased via the corpus callosum and anterior commissure. Inferior medial frontal polar regions in Met carriers showed very strong connections via the anterior forceps. We attributed this increase in edge weight to the known effect of BDNF on axonal pruning and suggest that in Met carriers there are more redundant and / or unnecessary connections in the brain. No structural changes were expected or identified between subjects with the tested *ADA* polymorphism. High classification accuracy between *BDNF* genotypes was demonstrated with a connectome-based classification scheme. We utilized a Gaussian Process classifier [135] through PRoNTo, a machine learning toolbox developed in MATLAB [136].

Interestingly, although the NBS revealed a large connected component of increased edge weight in the Met carriers, and their connectomes were accurately classifiable, the change in white matter architecture did not seem to affect calculated global network measures with any significance. Student's t-test revealed no significant differences between *BDNF* genotypes for any of the twelve tested network metrics. To delve further into the results, we used the "two one-sample test" (TOST) approach to evaluate equivalence between the groups [137, 138]. Figure 2 demonstrates, for the networks' global efficiency, the method through which differences and equivalence were evaluated. A set of R and ggplot2 [139] functions for performing the tests and plotting relevant figures can be found at `https://github.com/CyclotronResearchCentre/NetStats`. Our results, described in Table A.1, show that nearly all of the tested global network measures - except clustering and percentage of connected fibers - are indistinguishable between allelic

groups in our sample. Since it is unclear how best to correct for multiple comparisons when testing highly interdependent network metrics, and especially ambiguous when the tests are of statistical equivalence [140, 141], these values have not been corrected for multiple comparisons.

No significant linear correlations (after Bonferroni correction) were identified between any of the psychological assessments and the network measures studied. This is not particularly surprising since our subjects were only chosen if they fit within a narrow range of scores on each of the psychological tests.
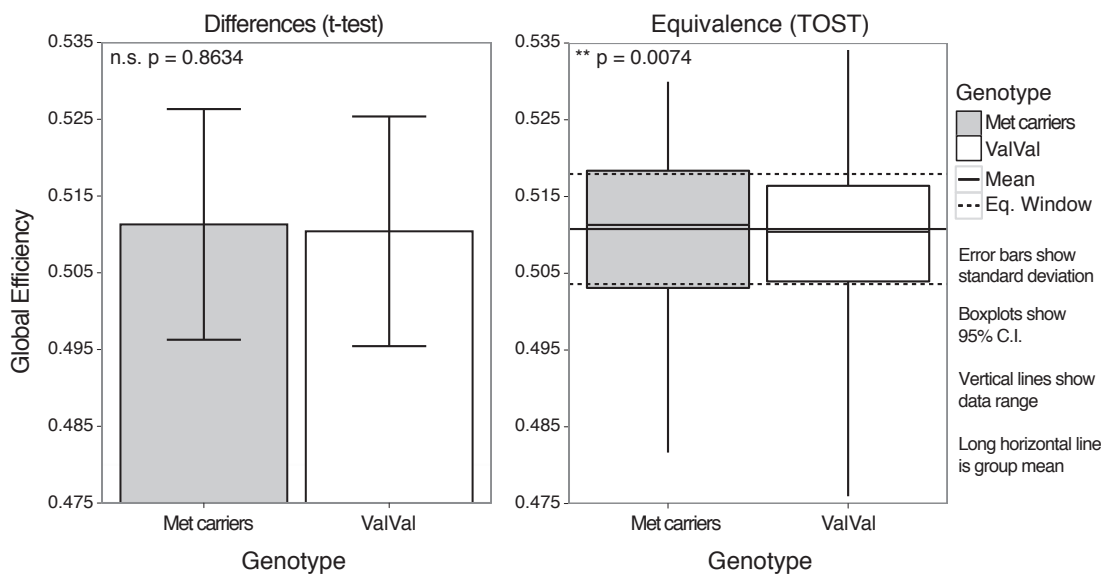
Figure 3.1: Equivalence testing of global network efficiency. A demonstration of the statistical testing for equivalence, using global efficiency, shows that there is not only no significant difference, there is no statistical distinguishability between *BDNF* allelic groups for network efficiency. C.I = Confidence Interval, Eq. = Equivalence, TOST = two one-sample test.

3.3 Discussion

Although we now know that connectivity patterns in brain networks are heritable traits, it is still extremely difficult to untangle the effects of specific genes and their alleles. The study described in Paper I appears to provide an intuitive link between the biological basis of BDNF actions and the neuroimaging literature. It is unlikely, though, that the link between axonal growth patterns and macroscopic tractography models is indeed this straightforward.

Genome-wide association studies (GWAS) provide a method for testing hundreds of thousands of single-nucleotide polymorphisms at once for their influence on neuroimaging biomarkers. A number of research groups have performed GWAS on FA maps [142–145], and more recently, structural connectome matrices [146]. Results from these and other studies show that single-nucleotide polymorphism effect sizes are generally very small, and most studies showing large effects are irreproducible [118]. An accurate criticism of this study is that it reported a seemingly large effect using a relatively small sample. Our findings, though, are coherent with those already demonstrated in several independent samples [147, 148].

Track density imaging in Parkinson's disease

The cardinal symptom of Parkinson's disease is dyskinesia. This is generally considered a consequence of the substantive loss of dopaminergic neurons in the substantia nigra and their projections to the striatum. Presynaptic dopaminergic terminal function in the striatum is easily imaged with ^{18}F-DOPA positron emission tomography (PET) [149]. Striatal dopamine storage capacity and transporter availability can also be imaged with other radiotracers. Although PET remains the gold standard for diagnosis, it is not universally available and therefore *in vivo* MRI-based biomarkers are highly sought after. Unfortunately, the substantia nigra of Parkinson's patients appears normal with conventional MRI contrasts.

A large number of DWI studies have been performed using patients with Parkinson's disease (PD) and the most common result is decreased FA in the substantia nigra [150]. In Paper II, we studied Parkinson's disease using advanced diffusion analysis techniques. The manuscript is the result of a long process of trial and error, beginning with an alternate dataset and another analysis method.

4.1   First attempts

This study began as an application of the connectome construction and network analysis methods created for Paper I. In our first two attempts, we used a low b value diffusion acquisition and a smaller number of subjects.

We began with a dataset in which seven unweighted (b = 0) volumes were acquired followed by a set of diffusion-weighted (b = 1000 s/mm^2) images using 61 non-collinear directional gradients. The field of view was 220.8 x 220.8 x 138 mm^3 (96 x 96 x 60 voxels), with isotropic voxels of 2.3 mm^3. We studied 21 (9 male, age:

67 ± 14) patients clinically diagnosed with Parkinson's disease and 21 (13 male, age: 64 ± 10) healthy control subjects.

First, connectomes were constructed (as in Paper I) using the 1015-region parcellation scheme of the Lausanne 2008 atlas, constrained spherical deconvolution with $L_{max} = 8$, and probabilistic tracking of 300,000 streamlines. We evaluated various network metrics and tested the networks using the NBS. No significant results were obtained for any measures. Next, we evaluated track density images by seeding 5 million tracks and registering the images to the FMRIB58 FA template using consecutive linear and non-linear transformations (using the FMRIB Software Library). Between-group statistics were performed using SPM8 and cluster-level FWE corrected p-values. Non-stationarity correction was used to account for local smoothness of the search volume [151]. We also tested a method for evaluating track density in each direction, using non-stationarity correction for the F-test [152]. These analyses were not totally fruitless; small areas of statistically significant increases in TDI were found in the pedunculopontine nucleus (PPN). The PPN is important for gait and is frequently a target for deep brain stimulation (DBS) in PD. We decided to move on and test this approach using the high b value dataset described in Paper II. These were useful failures, though, as they helped refine the pipelines for future analyses.

4.2   Overview

A number of studies have identified nigral atrophy using DWI, but none so far have been able to identify nigrostriatal denervation. We suspected that track quantification methods, which have validated super-resolution qualities [61, 62], could be capable of identifying damage in this pathway. The final study population (n = 53) contained 27 patients (14 male, age: 66 ± 8) clinically diagnosed with Parkinson's disease and 26 healthy control subjects (14 male, age: 64 ± 8) matched for age, gender, and education level. None of the subjects showed signs of dementia. PD patients had a mean disease duration of 5 years and mean score on the Hoehn & Yahr scale of 1.5, making this an early-stage population for a diffusion study [150].

Briefly, we performed CSD on a high b value (b = 2500 s/mm^2) HARDI dataset (120 directions) and seeded 5 million streamlines in the white matter. Track density imaging was performed with 1 mm^3 isotropic voxels. Average pathlength maps were used to create a study-specific template using iterative symmetric diffeomorphic normalization [64, 153–155]. According to a recent evaluation of non-linear

deformation algorithms, this approach is among the most accurate available [52]. Non-parametric statistical analysis was applied with estimated subject movement indices as nuisance covariates [69]. A distinct low b value (b = 1000 s/mm^2) acquisition, also with 120 gradient directions, was analyzed using tract-based spatial statistics (TBSS) [156] after tensor fitting with non-linear least squares.

Although the TBSS analysis revealed no statistically significant results, the TDI analysis identified both nigrostriatal and extra-nigral structural abnormalities in the patients with Parkinson's disease. This manifested as large clusters of significantly increased streamline density in clusters extending from the substantia nigra to the ventromedial putamen, as well as in limbic and cognitive networks. The extra-nigral abnormalities encompassed parts of the superior parietal lobule, dorsomedial thalamus, cingulum, orbitofrontal cortex, and occipital lobe bilaterally, and were remarkably symmetric.

4.3 Discussion

While our results are topologically quite expectable from what is known about PD, they signalled an increase in track density, rather than a more easily explainable decrease. This may be due to unforeseen sources of error in the method redirecting the tracking algorithm toward pathological signal variations in these regions. The track-weighted imaging method at present may not be mature enough to be applied to clinical populations.

Converging evidence is mounting that dopaminergic terminal loss and the degeneration of axons, rather than the loss of neuronal somata in the substantia nigra, is the earliest and most dominant feature of Parkinson's disease [157]. In the leucine-rich repeat kinase 2 (LRRK2) transgenic mouse model of genetic Parkinson's disease, pathological features are found in dopaminergic axons before any loss of mesencephalic dopamine neurons [158]. Similarly, in the acute phase after MPTP administration in monkeys, degeneration can be observed in the dopaminergic striatal axon terminals before any cell body loss occurs in the substantia nigra [159]. Furthermore, there is evidence that α-synuclein aggregates initially form in axons and only later culminate in the death of the somata [160]. These studies suggest that the degeneration of axons in Parkinson's disease occurs through a "dying-back" mechanism which starts distally in the axon and continues in a retrograde fashion [161, 162]. Degeneration of projections to the striatum, however, may not be

visible until DWI approaches are used with high-field scanners. It may also be possible to identify DWI markers of early axonal degeneration in murine models and subsequently apply these to humans.

The use of techniques that provide complementary information is essential in neurology. While track quantification may yet play this role, it seems unlikely that it will become a primary diagnostic imaging technique, solely due to the mountain of assumptions performed prior to analysis. Fiber track bundling and directionally encoded colour TDI maps, though, may allow clinicians to use qualitative judgements for diagnosis. Track quantification approaches provide high-resolution imaging of the white matter, but their quantitative interpretability still remains to be seen. Differential diagnosis among Parkinsonian syndromes[1] is already possible with DWI [163] and may help prevent mismedication in difficult cases.

4.4   Voxel-based quantification

In addition to examining white matter using TBSS [156] and track density imaging, we also attempted to quantify variations in other neurobiological parameters. To do this, we used a fast acquisition protocol for producing proton density (PDw), magnetization transfer (MTw), longitudinal relaxation rate (R1), and transverse relaxation rate (R2*) maps [164]. These maps reveal complementary information about the micro and macromolecular structure of the tissue studied.

Specifically, PDw maps reflect the water content of tissue. The MTw signal is thought to reflect the macromolecular content of the voxel and is particularly dependent on the quantity of myelin in brain tissue [165, 166]. Here the MTw map is only semi-quantitative and reflects the percentage signal loss of magnetization induced by a single MT pulse [167]. The R1 and R2* maps are the rates of longitudinal and transverse spin relaxation for water protons. The former relates to the mobility of water and water content within the tissue [168], whereas the latter is a marker of GM iron content [169] and WM structure [170].

The MTw map was used for (GM/WM/cerebrospinal fluid (CSF)) segmentation because it gives better contrast in the basal ganglia [171, 172]. R2* was notably suggested as a biomarker of Parkinson's disease [173]. Indeed, in a recent longitudinal study, iron content in the substantia nigra of PD patients increased over time and correlated with the worsening of motor symptoms [174]. An example of the

---

[1]i.e. disorders of multiple system degeneration, such as multiple system atrophy, progressive supranuclear palsy, and corticobasal degeneration

voxel-based quantification (VBQ) maps is shown in Figure 4.1 for a patient from another study. These multiparameter maps have shown reliable acquisitions across multiple scanning sites [175] and may soon become widespread.
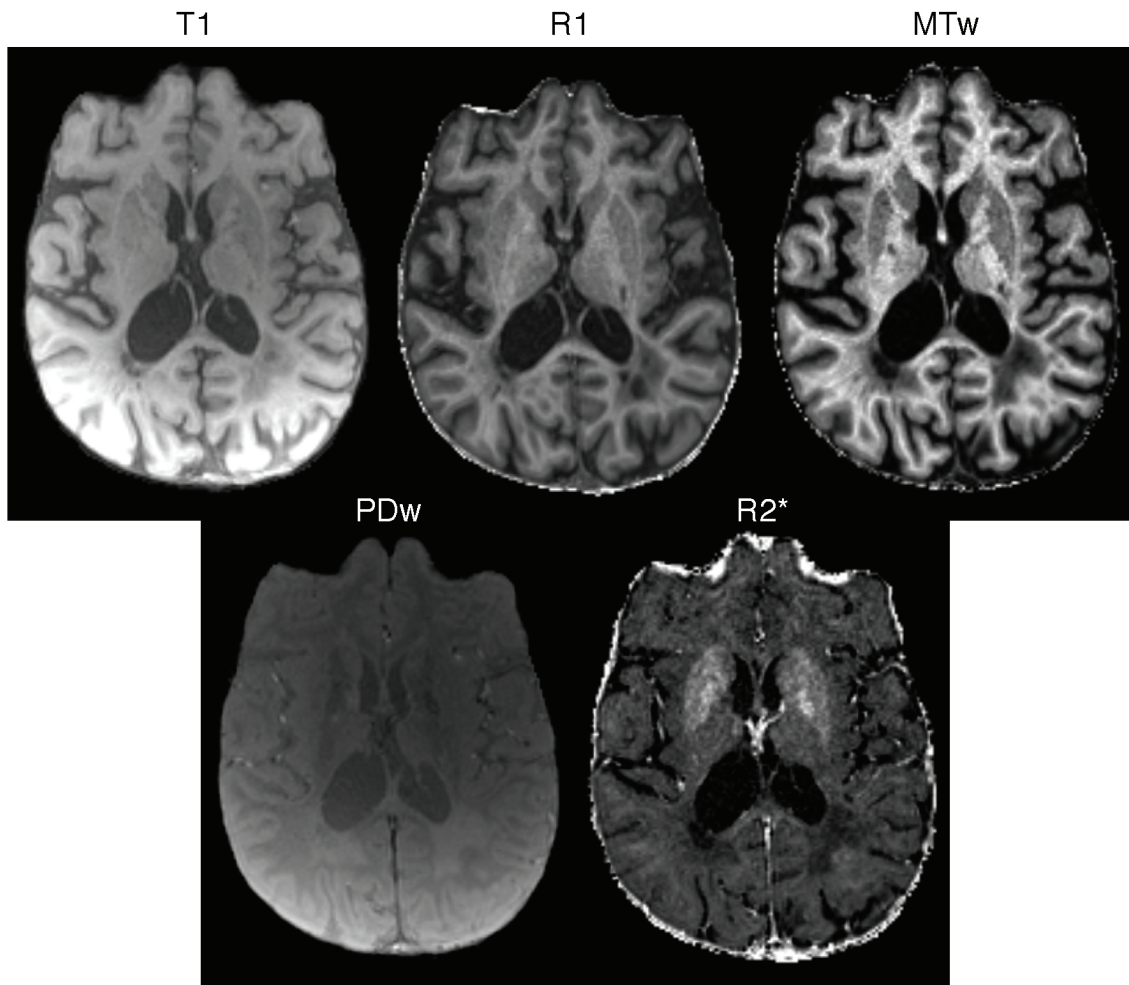
Figure 4.1: Example voxel-based quantification maps. Voxel-based quantification maps for a patient with multiple sclerosis. R1: longitudinal relaxation rate, MTw: magnetization transfer, PDw: proton density, R2*: transverse relaxation rate. Bright spots signalling high iron content are noticeable in the R2* map near the pallidum and putamen.

We created a study-specific MTw template using the Diffeomorphic Anatomical Registration Through Exponentiated Lie algebra (DARTEL) approach implemented in SPM8 [176]. Standard mass-univariate two-sample t-tests were performed for voxelwise comparison of quantitative maps (MTw, PDw, R1, and R2*) between controls and patients. No significant results were obtained. This may, in part, be due

to the "in-development" aspect of the VBQ SPM toolbox at the time. Aliasing artifacts were notable in some of the maps and it may be prudent to rerun the analysis once the toolbox can reliably produce these maps from the acquired scans.

Further analysis of this type of multiparameter data could be performed using multivariate classification. Each unique quantitative map could be included as a single feature set to help classify between healthy subjects and patients. The resulting weight maps would help determine which physiological parameters contribute most to the classification. This may provide insights into the macrostructural biological presentation of complex pathologies.

Realistic head modelling for EEG

In Paper III, a finite element reciprocity approach was used to solve the forward problem for electroencephalography.

For multi-shell spherical models there are demonstrated analytical solutions for obtaining the potential distribution on the surface of an ellipsoid given an arbitrarily located current dipole [177–179]. To evaluate our approach we constructed a four-shell (skin, skull, cerebrospinal fluid, grey matter) spherical model and contrasted the simulated leadfield against that of the analytical solution. We tested dipoles of varying depth in the spherical model and calculated relative difference and magnitude measures demonstrating the deviation from the exact solution. These metrics were also computed using two alternative state-of-the-art toolboxes, OpenMEEG's for BEM modelling, and NeuroFEM for FEM modelling. Our implementation showed superior accuracy and stability near tissue boundaries when compared to OpenMEEG [103, 180] and showed similar accuracy to NeuroFEM [181].

Next, an unstructured whole-head tetrahedral volumetric mesh was built from the T1 of a single healthy subject. Five tissue types were included: skin, skull, cerebrospinal fluid, grey matter, and white matter. Diffusion tensors were derived from DWI data with 120 gradient directions, b $= 1000$ s/mm^2, and 2.4 mm^3 isotropic voxels. Tensor eigenvalues were scaled to produce conductivity tensors and subsequently incorporated into the white matter elements of the volumetric mesh [20]. Two leadfield matrices were calculated; one in which isotropic conductivity was assumed within the white matter, and another in which conductivity tensors were included. These are referred to as the "isotropic" and "anisotropic" leadfields, respectively.

Root mean square deviation (RMSD) was calculated between the leadfield matrices, treating the x, y, and z components separately. RMSD was highest in each

direction in areas with projections from large fiber bundles. For example, in the x direction (left to right), grey matter regions connected by the corpus callosum showed the highest RMSD. Similarly, the RMSD in the y direction highlighted the anterior and posterior cingulate. In the z direction, grey matter regions near the corticospinal tracts were affected in both the superior parietal cortex and subcortical regions. This comparison indicates that these regions are misrepresented when isotropic conductivity is assumed during forward modelling. Single-dipole cost function mapping also demonstrated increased specificity toward the actual dipole location using the anisotropic leadfield matrix.

Finite element volumetric models have been repeatedly demonstrated in M/EEG source localization [182, 183] as well as simulations of transcranial magnetic stimulation (TMS) [24], transcranial direct current stimulation (tDCS) [184, 185], and transcranial alternating current stimulation (tACS) [186]. Furthermore, FEM approaches are taken when modelling mechanical deformations (e.g. for tumour growth and traumatic injury) [187, 188]. At the moment, though, these models are all built and tested using unique (and often proprietary) software and there is no open-source toolkit in use that is capable of performing all of these tasks. Conductivity tensor information is rarely incorporated.

The EEG forward modelling approach developed here is an evolution of this work in the SimNIBS package [24]. The implementation proposed uses Nipype [189] for provenance tracking and GetDP [190] for discrete problem solving. The source code is completely free and available under the GNU GPLv2 software license.

See `https://cyclotronresearchcentre.github.io/forward/`.

5.1   Future work

There are several possible avenues for extending this work:

Evaluate the reliability of the forward model

The head modelling approach here relies on an initial segmentation and tessellation of each tissue compartment and a large number of subsequent local mesh deformation and cleaning procedures. Since it relies on Freesurfer, it can be considered non-deterministic, and small variations in subject anatomy may be present if the procedure is performed repeatedly [191] or on different computers [192]. A comprehensive review and evaluation of FEM meshing strategies would be extremely

beneficial for the field (similar to [52] for non-linear deformation algorithms or the Fiber Cup [35] for tractography algorithms).

Interface the forward model with inverse solvers

Providing a bridge so that inverse approaches that are already implemented could be used with this forward model would be extremely beneficial. It is unlikely that this will be easy; solvers like FieldTrip [95], SPM [98], and MNE [100] are not written to deal with FEM-generated leadfield matrices. The inverse techniques involved are still generally applicable to these leadfield matrices [116], though, so it may be possible to adapt an available implementation.

Add support for MEG leadfields

Calculating the MEG leadfield using the reciprocity principle in a finite element (FE) mesh is non-trivial [193, 194]. The EEG reciprocity leadfield describes the electric field components in every grey matter element resulting from a unit current source at predefined scalp electrodes. The MEG reciprocity leadfield differs from the EEG leadfield in that it relates the magnetic field at each grey matter element to unit current sources placed at the MEG sensor sites small distances from the scalp, each defined with specific sensor orientations and geometries [195]. By calculating the magnetic vector potential at each element of the head model using the quasi-static approximation it is possible to create an MEG leadfield using reciprocity [194]. Implementation of the MEG leadfield should therefore be possible using the framework developed thus far.

Simulate brain stimulation

Patient-specific simulation of brain stimulation methods will help us understand their effects and tune their parameters. One such method, tDCS, has recently shown promise in the treatment of patients with disorders of consciousness [196], though the underlying basis for this improvement is unknown. Automated techniques for choosing the best placement of the electrodes, in order to maximize current to a specified region, may be useful. Simulation of tDCS and another non-invasive method, TMS, have already been demonstrated using SimNIBS; we have now removed the costly MATLAB requirement, simplifying installation and use. The FE model and simulation approach used here could also be used to simulate other techniques, such as

DBS. The pipelines that have been developed may be useful for multimodal brain simulation projects like The Virtual Brain[1] [197, 198].

Improve skull modelling

The skull is composed of three distinct layers, conducts preferentially in the radial direction, and varies in thickness throughout the head. Its geometric approximation and conductivity profile have a substantial influence on EEG source localization [199]. This issue is compounded because skull segmentation is difficult using only T1 images. In SimNIBS both T1 and T2-weighted magnetic resonance image (T2) images were used to model the skull, scalp, and CSF. Accurate skull segmentation may be possible with novel MRI techniques such as "black bone" imaging [200].

Computed tomography (CT) scans can provide excellent skull segmentation but are not typically done in healthy subjects because they expose the subject to ionizing radiation. In clinical cases, though, multimodal segmentation and meshing could provide increased accuracy for the leadfield (or whichever other simulation is being performed). Automated co-registration between the two modalities is quite difficult since CT contrast is so poor in the soft tissue, and this issue is exacerbated in subjects with complex anatomical features (e.g. implants). It may be possible to improve this co-registration by masking and co-registering the air or liquid cavities in both modalities in order to obtain the transformation matrix.

In some real-world testing I have encountered issues with meshes from T1 and CT images intersecting. Figure 5.1 shows a real-world example of meshes created from co-registered T1 and CT images. Potential explanations for the discrepancy in GM / skull boundary between the T1 and CT images are coregistration errors, segmentation / meshing errors, MRI distortion, and brain swelling.

Facilitate leadfield templates

Optimally it is best to calculate subject-specific leadfield matrices, but for very large studies it may be acceptable and substantially easier to use (or create) a template leadfield. This idea is not without a precedent [203]. The general concept is that a high-resolution leadfield is created for an average subject (i.e. the "template") and then warped to each subject's space and used to localize signals. Templates can also be created (as in Paper II) using iterative high-dimensional deformations [52, 153–155].

---

[1]This also applies to the automated connectome mapping pipelines developed for Paper I

The central choice pre-empting this strategy is how to warp the leadfield matrix. Intuitively, it seems possible to sample the leadfield regularly at each element and construct a regular hexahedral volumetric image of the matrix, similar to the dimensions of the MRI. A non-linear transformation between the template T1 and subject T1 could then be applied to the leadfield "image". The leadfield is currently of size $3N$ x M, where N is the number of mesh elements and M is the number of EEG sensors. The data could be sampled and stored as a 4D image of size (X x Y x Z x 3 x M), where X, Y, and Z would represent the dimensions of the original T1 image. The T1 could be upsampled prior to registration to allow for higher-resolution leadfield images. Subsequent source reconstruction techniques would have to be able to operate on this image, rather than the FE mesh.

The main benefit of this would be that relatively accurate EEG source reconstructions could be performed extremely quickly, as the forward modelling pipeline would only require a single step of non-linear registration. A further option could be to create study-specific leadfield templates for studies with similar but "non-standard" anatomical features[2]. It is unclear if this technique would perform better than fast BEM approaches.

---

[2]e.g. infants, or the elderly

Volume rendering of CT scan

Surface meshes

Issues with meshes from MRI and CT intersecting
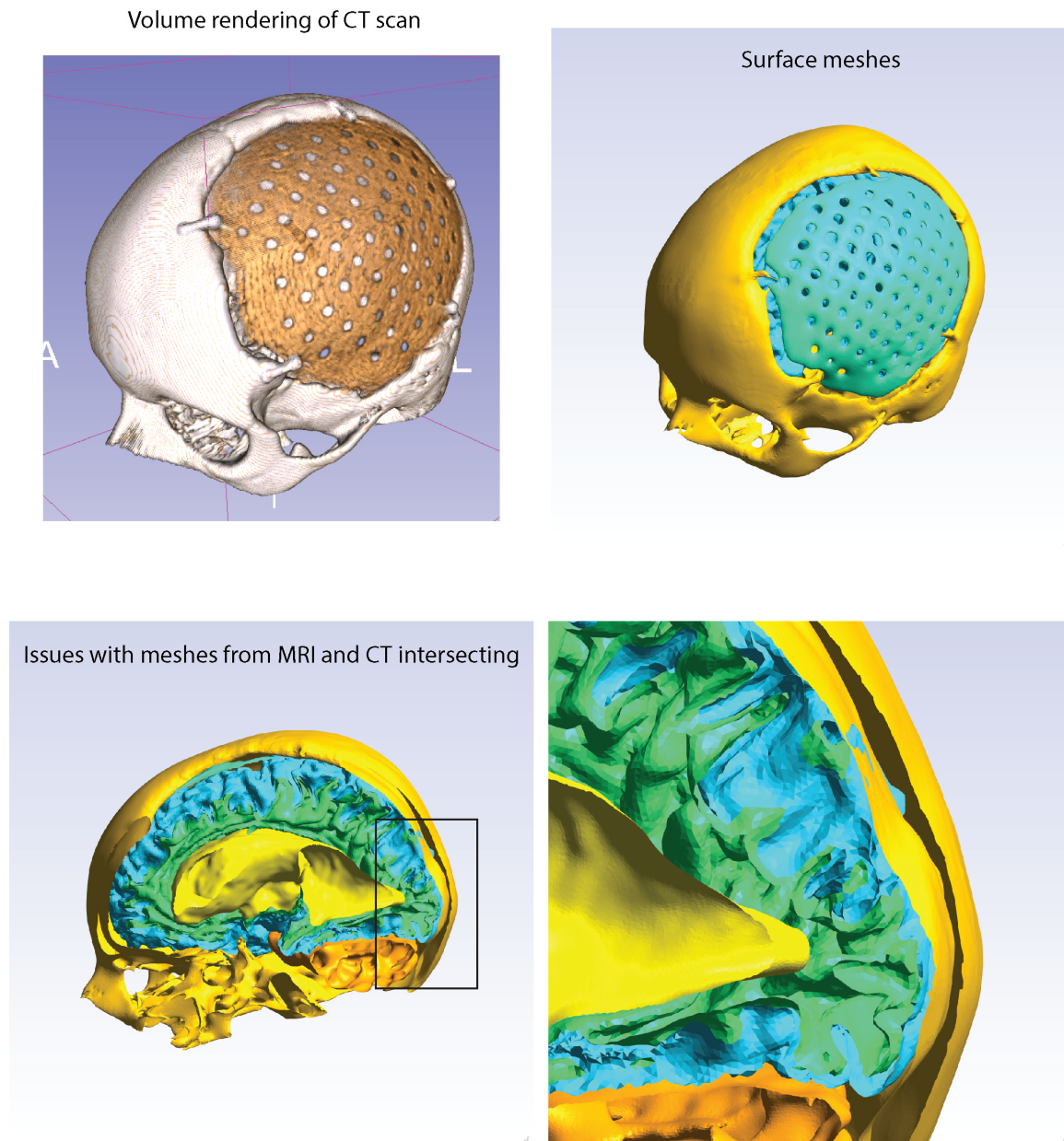
Figure 5.1: Conflicts between multimodal meshes. Volume rendering of CT data and tessellated meshes from T1 and CT. This patient is a 13 year-old male that has had a left parietal craniectomy following a traumatic injury. A porous polymer implant has been put in place below the skin. The skin mesh has been hidden for clarity. Visualized in Slicer (http://www.slicer.org) [201] and Gmsh [202].

Discussion

This work has demonstrated several methods for *in vivo* modelling and analysis of brain properties.

Diffusion-weighted MR imaging is still maturing. As shown in Figure 6.1, it is roughly the fourth most published neuroimaging method, behind fMRI, PET, and EEG. Much like with other techniques (e.g fMRI), studies will become more focused as the tools are better understood. Network analysis methods are improving, but the majority of studies still apply the methods indiscriminately and fish for results. One notable issue is that parameters often have no justification, other than their occurrence in previous papers. Small incorrect assumptions can have drastic effects on the results of this type of advanced modelling, and each parameter should be justified in the particular population under investigation.

Electroencephalography as a tool is extremely mature, but the field has left modelling behind. EEG studies could be reporting results with millimetre precision, but don't because of their poor choices of forward models. There are huge strides to be made in the EEG field by simplifying the construction and use of accurate head models with state-of-the-art inverse solvers. The excuse of computationally intensive calculations no longer has merit. Modern computers are quite capable of constructing and visualizing enormously complex (> 10 million elements) models. Scalable on-demand cloud servers are an economic solution for researchers with limited on-site hardware. Finite element models should enjoy a larger role in neuroimaging studies.

6.1   Reproducibility in neuroimaging

The current state of reproducibility in neuroscience is worrying. To illustrate my point, I will take the literature related to the study of Parkinson's disease with DWI

as an example. A recent meta-analysis has found that the published studies on this topic are inconsistent and unreliable [204]. A slightly less recent meta-analysis in a more well-renowned journal, did not share this conclusion [150].

Many poor practices are behind this confusion. One is the reporting of large effect sizes in very small samples (often less than ten subjects). Another is publication bias, in which unexpected results (or those not equivalent to the first, potentially unreliable dataset) are not given sufficient consideration. One suggested approach to avoiding these issues is to pre-review the study design prior to acquiring the data. In this manner the analysis methods are qualified and cemented prior to obtaining the results so there is a lower chance of publishing irreproducible results and drawing false conclusions.

To further avoid these issues the minimum number of acceptable subjects per study should be increased to improve the signal-to-noise ratio in the literature. Principal investigators and grant committees should start performing and/or requiring statistical power calculations (e.g. for fMRI [205]) so that studies are not irreversibly flawed from their conception. Editors and reviewers should reject studies with an unreliably low number of subjects. Researchers worried about computational time and cost should consider cloud server-based processing methods. Recently, the NITRC Computational Environment was released as a publicly available machine image. The study detailed in Paper II was performed almost entirely using on-demand online servers. This approach has the benefit of dramatically reducing processing time.

Another issue more specific to neuroimaging is that studies tend to use wildly different methods. This is compounded by the fact that they also use different scanners, sequences, and image dimensions. To an outsider it appears that the only standard methods in neuroimaging are the statistical tests. An analysis with Neurotrends, a package for parsing PubMed (an article repository) metadata revealed that, at least in fMRI studies, there are nearly as many unique methods as there are published studies [206]. These unique methods are also known to give varying, and often completely different, results [207]. It has become difficult to claim that results in a new study confirm those of previous studies when the methods are so different. Developers of neuroimaging methods should focus their time to collaboratively build standard analysis pipelines to reduce the methodological variation between studies.

There is a massive amount of research time wasted spent re-implementing code that already exists. As an example, there are at least 23 different packages capable

of fitting a diffusion tensor, most of them using the same approach[1]. Furthermore, many of these packages only operate on program-specific data formats making interoperability difficult, and leading to other researchers building tools[2] solely for conversion. Researchers should use standard formats when developing new tools and release their software to the public early and often so that the level of repetition is minimized.

Journals and reviewers should mandate source code be released alongside every published paper[3]. It is currently appallingly difficult to reproduce[4] the vast majority of published papers. What makes this worse is that reviewers can suggest the use of published, but not publicly available, methods. Implementing another author's published algorithm can often result in erroneous results, since comprehensive algorithmic details are rarely provided [208].

Collaborative open-source software libraries for research are the inevitable future. Many versions may exist as users have their individual language preferences, but highly-used algorithms (e.g. for segmentation and registration) should be standardized and optimized. The cost in research time (and money) of processing, modelling, and testing data should not be ignored. The neuroimaging field will benefit from efficient and well-written neuroimaging pipelines. To promote replication, all of the source code involved in this work has been provided online for free (as part of Nipype or other repositories).

It's important to understand the barriers to the changes I list above. By far the largest is the entrenched publisher-researcher dynamic present in academia. Governments and universities are funnelling money into privately held publishers that provide very little value to academics. Specifically, publishers facilitate peer review, automate typesetting, and provide distribution for the resulting manuscripts[5]. Institution-run preprint hosting databases, such as http://arxiv.org/, have demonstrated that hosting and distributing academic manuscripts is reasonably easy to provide. Typesetting is a simple procedure provided by open-source packages (usually LaTeX, which this thesis is written in). Peer review remains opaque at present and could be improved by community-driven publication practices (e.g. [209]). Double-blind peer review followed by transparent publication (i.e. reviewer's names are

---

[1]Camino, MRtrix, FSL, FreeSurfer, Dipy, Diffusion Toolkit, DTIStudio, ExploreDTI, AFNI, VistaSoft, SPM's Diffusion Toolbox, Slicer, DTIPrep, DTI-TK, TORTOISE, DSI Studio, dtiBrainScope, medInria, R's dti package, BioImage Suite, DoDTI, JIST, SATURN, found using NITRC and [4]

[2]e.g. Camino-TrackVis (http://www.nitrc.org/projects/camino-trackvis/)

[3]Sadly, publishers have no incentive to encourage this

[4]Not to mention, access

[5]*Some* publishers provide proofreading, though this is hardly an expensive service

published) would help prevent corruption and favouritism as well as facilitate the equal treatment of women. A precedent already exists: double-blind review practices in the field of ecology have lead to a significant increase in the share of female first-authored papers [210]. The transition to open-access journals with "unorthodox" approaches to peer review cannot come from young researchers. In the early stages of an academic career it is still mandatory to publish in "high impact" journals (practically all of which are provided by large publishers) in order to secure a post-doctoral position. The driving force must come from established principal investigators. Campaigns such as The Cost of Knowledge (`http://thecostofknowledge.com/`) should be backed by funding organizations. In 2010, Elsevier, Springer, John Wiley & Sons, and Informa all made over 32% profits on combined revenues of €3.2 billion [211, 212]. This level of profit-taking greatly reduces the breadth of scientific research that can be performed, and academics must stick to their convictions to change the status quo. Only when top journals are run for-science and not for-profit will it be possible to raise the bar of reproducibility required for publication.

The second major barrier is the lack of proper interdisciplinary training for researchers. Neuroscience especially is split between technical and non-technical researchers, neither of which generally makes a concerted effort to understand the labour of the other. Technical staff need to grasp more thoroughly the biological aspects and practical goals of the problem they're trying to solve. This could help promote the development of more robust tools that can be used more widely. Technical staff should also consider following best practices of computer science, rather than creating one-off in-house scripts to solve their problems. Developing as a team leads to more reliable tools that are easier to use and share. Non-technical researchers should spend more time trying to understand the techniques they are applying. It's irresponsible to draw conclusions that may affect future patient care based on a poor understanding of complex techniques. Neuroscientists should stop ignoring statistical best practices - even with a well thought-out *a priori* hypothesis you are not immune to false positives. All researchers should be careful interpreting their results when they are unexpected. It's best to remain skeptical, as it's far more likely that any given result is an artifact than a real effect.
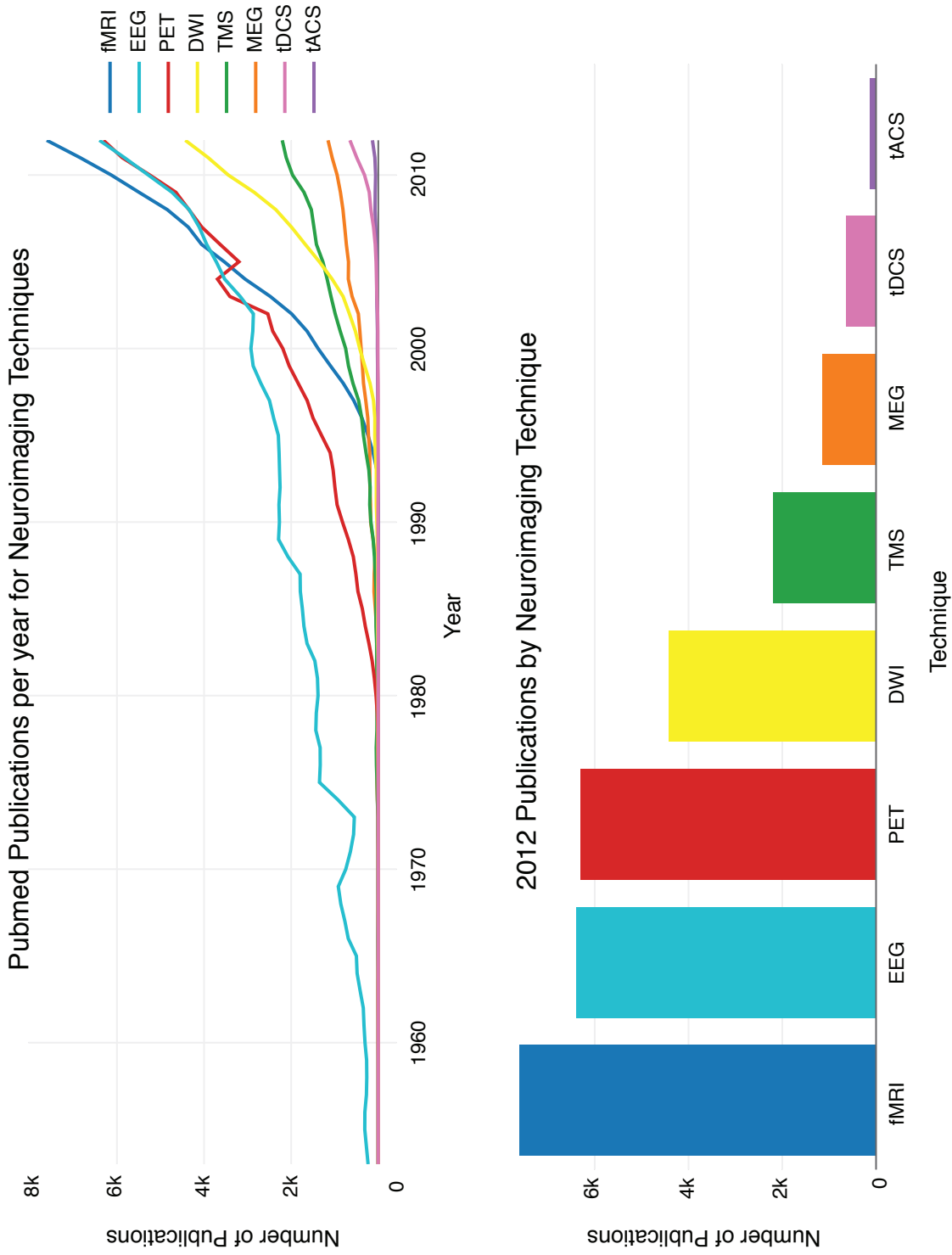
Figure 6.1: Neuroimaging publications by technique. A cursory search of PubMed (http://www.ncbi.nlm.nih.gov/pubmed/) was performed using BioPython (http://biopython.org/). The number of publications per year was recorded for the past 50 years using a set of specified terms for each modality. Despite being developed far later, fMRI quickly overtook EEG. Diffusion-weighted imaging (DWI) is following a sharp upward trajectory.

Concluding remarks

In this thesis I have developed and applied various multimodal neuroimaging modelling and analysis techniques. To summarize:

1. ***BDNF* genotype influences the architecture of white matter pathways in the human brain.** Brain network mapping pipelines were developed and applied to 36 subjects. Network analysis revealed that healthy adult carriers of the Met allele at codon 66 have increased structural connectivity bilaterally in frontal and parietal regions. Machine learning was successfully used to classify subjects' *BDNF* genotypes given only their connectomes.

2. **Patients with Parkinson's disease show extra-nigral white matter abnormalities in limbic and cognitive networks, as well as in the nigrostriatal pathway.** Super-resolution track-weighted imaging workflows were developed and applied to 27 Parkinson's patients and 26 elderly controls. Streamline quantification identified changes in disease-relevant areas in these early-stage PD patients. Classical tensor-based analysis methods were unable to identify any variation between the two groups.

3. **Finite element modelling for EEG source localization is efficient enough for wide adoption.** Modelling conductivity profiles *in vivo* from diffusion-weighted imaging is beneficial and has a negligible computational cost. The forward model developed was shown to be more accurate than the current state-of-the-art alternative. This framework could also be used to simulate various types of brain stimulation techniques.

Paper I

Altered White Matter Architecture in *BDNF* Met Carriers

Ziegler, E., Foret, A., Mascetti, L., Muto, V.,
Le Bourdiec-Shaffii, A., Stender, J., Balteau, E.,
Dideberg, V., Bours, V., Maquet, P., Phillips, C.

Altered White Matter Architecture in *BDNF* Met Carriers

Erik Ziegler[1], Ariane Foret[1], Laura Mascetti[1], Vincenzo Muto[1], Anahita Le Bourdiec-Shaffii[1], Johan Stender[1], Evelyne Balteau[1], Vinciane Dideberg[2], Vincent Bours[2], Pierre Maquet[1,3], Christophe Phillips[1,4]*

1 Cyclotron Research Centre, Université de Liège, Liège, Belgium, 2 Department of Human Genetics, CHU Sart Tilman, Liège, Belgium, 3 Department of Neurology, CHU Liège, Liège, Belgium, 4 Department of Electrical Engineering and Computer Science, University of Liège, Liège, Belgium

Abstract

Brain-derived neurotrophic factor (BDNF) modulates the pruning of synaptically silent axonal arbors. The Met allele of the *BDNF* gene is associated with a reduction in the neurotrophin's activity-dependent release. We used diffusion-weighted imaging to construct structural brain networks for 36 healthy subjects with known *BDNF* genotypes. Through permutation testing we discovered clear differences in connection strength between subjects carrying the Met allele and those homozygotic for the Val allele. We trained a Gaussian process classifier capable of identifying the subjects' allelic group with 86% accuracy and high predictive value. In Met carriers structural connectivity was greatly increased throughout the forebrain, particularly in connections corresponding to the anterior and superior corona radiata as well as corticothalamic and corticospinal projections from the sensorimotor, premotor, and prefrontal portions of the internal capsule. Interhemispheric connectivity was also increased via the corpus callosum and anterior commissure, and extremely high connectivity values were found between inferior medial frontal polar regions via the anterior forceps. We propose that the decreased availability of BDNF leads to deficits in axonal maintenance in carriers of the Met allele, and that this produces mesoscale changes in white matter architecture.

Introduction

Secretion of brain-derived neurotrophic factor is essential for synaptic plasticity in the central nervous system during neurodevelopment [1], as well as in mature brains, in which it promotes long-term potentiation and the formation of long-term memory [2,3]. A common human non-synonymous single-nucleotide polymorphism in the *BDNF* gene (Val66Met, rs6265) decreases activity-dependent BDNF release in neurons transfected with the human A allele (Met-*BDNF*) [4]. It is also associated with variation in human memory [5,6], and with several neurological and psychiatric disorders [7]. We reasoned that the persistent differential activity-dependent BDNF release implied by this polymorphism should also be associated with differences in adult brain structure. Accordingly, the polymorphism affects the anatomy of the hippocampus and prefrontal cortex [8]. In this study we examine structural connectivity in the brains of normal human participants stratified according to *BDNF* genotypic group.

Indeed, for any equivalent set of connections, there is substantial variability in the density of cortical fibers between individuals of the same species [9]. This variability is in part genetically determined. Functional MRI in monozygotic and dizygotic twins has shown that 60% or more of the inter-subject variance in transmission efficiency of cortical networks can be attributed to genetic effects [10]. However, the mechanisms by which this

genetic influence impacts human brain connectivity are not yet determined. Comparison of groups by *BDNF* genotype may be useful for assessing the impact of activity-dependent processes on brain connectivity.

Here, we originally hypothesized that there would be decreased structural connectivity in Met carriers corresponding to the reduced availability of the neurotrophin. We examined a healthy young population with diffusion-weighted MR imaging, reconstructed their white matter tracts with probabilistic tractography, and examined the effect of carrying the *BDNF* Met allele at the connectome level. Contrary to our hypothesis, we found a marked increase in connectivity strength as well as altered track topology for Met carriers.

Results

Population

In our cohort (n = 134), the studied non-synonymous coding single-nucleotide polymorphism (rs6265) was in Hardy-Weinberg equilibrium ($\chi^2 = 3.25$, p = 0.07) with genotypic frequency of 0.6 (G/G), 0.31 (G/A) and 0.09 (A/A). The final study population comprised 36 healthy subjects aged 18–25. Fifteen (9 male) were identified as carrying the Met allele. The remaining 21 (9 male) were homozygotes for the Val allele and were referred to as the Val/Val group. The groups did not vary significantly in IQ or age,

nor did their scores differ for a battery of psychological tests (**Table S1 in File S1**).

Network-based statistics

In our networks, with 1015 nodes and an average of 66,456 edges, we identified 387 connections in which the number of connecting tracks was significantly greater in carriers of the Met allele than in the Val homozygotes (p = 0.0122, permutation testing). The relative connection strengths for these edges are shown in **Fig. 1a**.

For Met carriers the strength at these edges was found to range between 1.75 and 48 times their strength in Val/Val. Of these edges, 41 (11%) were found to have between 75% and 200% more tracks in Met carriers than in Val homozygotes. Met carriers had 200% to 400% more tracks in 123 (32%) of the edges, 400% to 900% more tracks in 104 edges (27%), and even greater factors in the remaining 23 edges (6%). The affected edges were largely central connections and were not short or uncommon fiber pathways.

Roughly one quarter (96) of the edges that were identified were not present in any of the Val/Val subjects (i.e. the mean value in Met carriers was significantly greater than the value of zero, found in Val homozygotes). **Fig. 1b** shows the mean number of tracks for the 96 edges that were only present in the Met carriers. The connections unique to Met carriers appeared consistently across the group. We did not find any edges with significantly lower strength in Met carriers. The identified connectivity changes are unlikely to represent false positives because of the stringent non-parametric statistical method [11]. Moreover, the reported differences were specific to the *BDNF* polymorphism; subjects were also divided by gender (18 F, 18M), and by their adenosine

deaminase (ADA) genotype (17 GA, 19 GG), and no significant results were obtained.

Global network metrics (graph density, number of connected components, transitivity) showed no variation between groups. Local nodal metrics (degree, clustering coefficient, number of triangles, [closeness, betweenness, degree] centrality, highest *k*-core number) were averaged for each participant and also did not vary. Wiring cost and network efficiency, compared both for the whole network as well as for only corticocortical connections, were unaffected by *BDNF* genotype. The total number of tracks per connectome, out of the generated 300,000 per subject, did not differ. The lack of significant variation in any of the network metrics is understandable because the total number of altered edges (387) is less than 1% of the mean number of edges (66,456) per network.

Classifier performance

The classifier was able to discriminate between Val homozygotes and Met carriers with 86.1% global accuracy. The predictive value for the Val/Val and Met carrier groups were 94.4% (p = 0.001) and 77.8% (p = 0.003), respectively. In **Figure 2** the weights obtained by the classifier are visualized as edges in the brain network. For the classifier trained to identify gender, the global accuracy reached 63.9% (n.s.). Identifying the subjects' adenosine deaminase (ADA) genotype was only possible with an accuracy of 58.3% (n.s.).

Tractographic basis

Structural connectivity in Met allele carriers was found to be higher throughout the forebrain (**Figure 3**). Large increases were
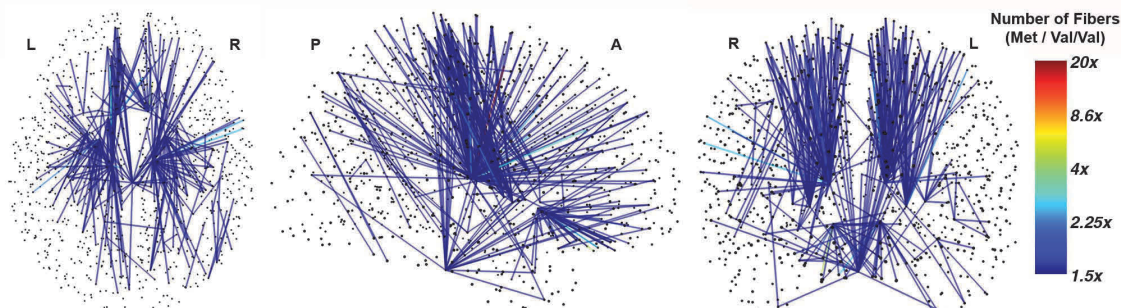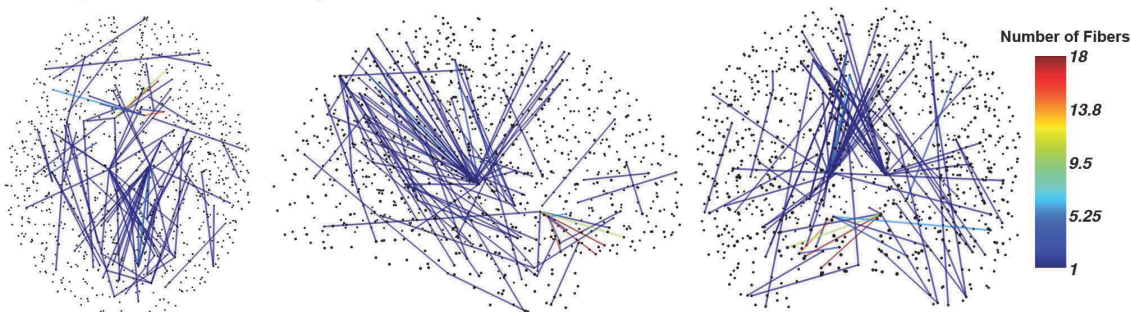
Figure 1. Significantly increased regional connectivity and topological changes in Met carriers. (**a**) Track count increase for each connected edge in Met carriers (n = 15) versus Val/Val subjects (n = 21). (**b**) Region-to-region track pathways that are present only in the Met carriers. doi:10.1371/journal.pone.0069290.g001

Spatial distribution of classifier weights
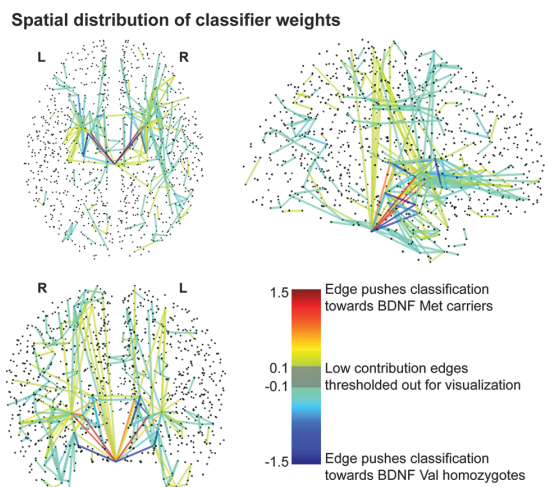
Figure 2. Classifier weight distribution. The weights obtained by the classifier have been plotted as network edges in order to show their spatial distribution. The thresholding procedure removed 99.75% of the edges for clarity. The remaining connections represent 21.69% of the absolute weight.
doi:10.1371/journal.pone.0069290.g002

found in connections corresponding to the anterior and superior corona radiata, including the corticothalamic and corticospinal projections from the sensorimotor, premotor, and prefrontal portions of the internal capsule. General interhemispheric connectivity was increased via the corpus callosum and anterior commissure. Extremely high connectivity values were found between inferior medial frontal polar regions via the anterior forceps. The Met carriers also presented novel connections within the cingulum, corpus callosum, and anterior forceps, which were not found in the Val homozygotes.

Discussion

Using high-resolution connectome mapping, we observe significant differences in structural brain connectivity between samples of normal young healthy human volunteers recruited based on the Met allele of the *BDNF* gene. These differences appear to involve specific fiber tracts; although widespread, they do not modify connectome parameters computed over the whole brain. They also appear specific to this allele; no such difference could be found for the polymorphism in the adenosine deaminase gene, or even for gender. We further demonstrate that this structural information can be used, with a reasonably high accuracy, to identify the *BDNF* genotype of an individual from his structural brain wiring.

In many regions the number of connecting tracks in Met carriers is increased by a factor of 3 or more. These are substantial changes at a mesoscopic anatomical level that are in line with previous findings by other groups. One large study examined fractional anisotropy (FA) – a measure of the restrictedness of random motion in water molecules – in 455 subjects and reported higher values, in some areas by up to 15%, in Met carriers [12]. A larger number of fibers oriented in the same direction would necessarily increase local anisotropy. Our findings confirm and extend their findings by specifying the nature and topology of these differences. It is not white matter integrity that is altered between Met carriers and Val homozygotes, but rather the strength and

architecture of their white matter tracts. The connections with increased strength in Met carriers predominantly involve the thalamus and brainstem, the sensorimotor areas of parietal and frontal cortex, and the ventral medial prefrontal cortex. The occipital, posterior parietal, and temporal areas also appear to differ between allelic groups to a lesser extent.

It must be stated that the results obtained here are dependent on the regional parcellation of the structural brain images. Previous studies have shown that the choice of region size and number greatly impacts the resulting network metrics [13,14]. In this work we chose to use a previously published and open-source parcellation scheme that depends on automated atlas-based segmentation [14–17].

Intriguingly, these anatomical changes do not translate into improved performance in either of our populations. Indeed, by design, our samples were matched for various demographic variables including IQ, age, and education level. One possible explanation for this phenomenon is that the increased connection strengths are due to redundant connections that are not essential to sustain the speed or efficiency of information processing.

The mechanisms causing these alterations cannot be derived from the current data. However, in addition to its involvement in long-term potentiation and synaptic plasticity [2], BDNF has also been implicated in axonal pruning and maintenance. BDNF is released from stimulated "winning" neurites and binds to the p75NTR receptor on nearby "losing" terminals, triggering the elimination of synaptically silent axonal terminal arbors [18,19]. It is tempting to suggest that the reduction in activity-dependent BDNF secretion accounts for the observed changes in white matter architecture. If indeed silent axons are relatively less likely to be pruned due to reduced BDNF secretion in Met carriers, brain connectivity might eventually be less profoundly shaped by experience than in homozygous Val individuals, without any conspicuous behavioral consequences.

In keeping with this hypothesis, brain maturation from childhood to adolescence is a nonlinear regionally selective process [20]. Gray matter loss is abundant, as is axonal myelination, and both continue until early adulthood. Consistent with our findings, grey matter volume in adults was shown to be lower in Met carriers in both the lateral frontal cortices and hippocampi [8]. Moreover, these differences were deemed independent of age (18 to 60) and gender, which suggests that the morphological changes are occurring prior to adulthood. It is possible that the increase we identify in connecting tracks is a result of deficits in axonal maintenance during adolescence, a key period of synaptic revision. When tested at age 11, children in a longitudinal study showed no differences in verbal reasoning that could be associated with their *BDNF* genotype. When the same cohort was tested again, the elderly Met homozygotes outperformed heterozygotes as well as their homozygous Val counterparts in both verbal and non-verbal reasoning [21]. It has also been reported that Met carriers show enhanced task-switching abilities during old age [22]. These convergent findings support the idea that the Met allele protects against age-related detriments in brain function, possibly by providing redundant or degenerate connectivity.

Finally, although we matched our population samples with great care and conducted conservative statistical analyses, our study is not immune from random sampling biases. The absence of significant results concerning ADA polymorphism and gender indicate that the reported effects are specific to *BDNF* polymorphism. However, contradictory results have been reported about the effect of *BDNF* polymorphism on cognitive performance and disease susceptibility [23], potentially caused by genetic interac-
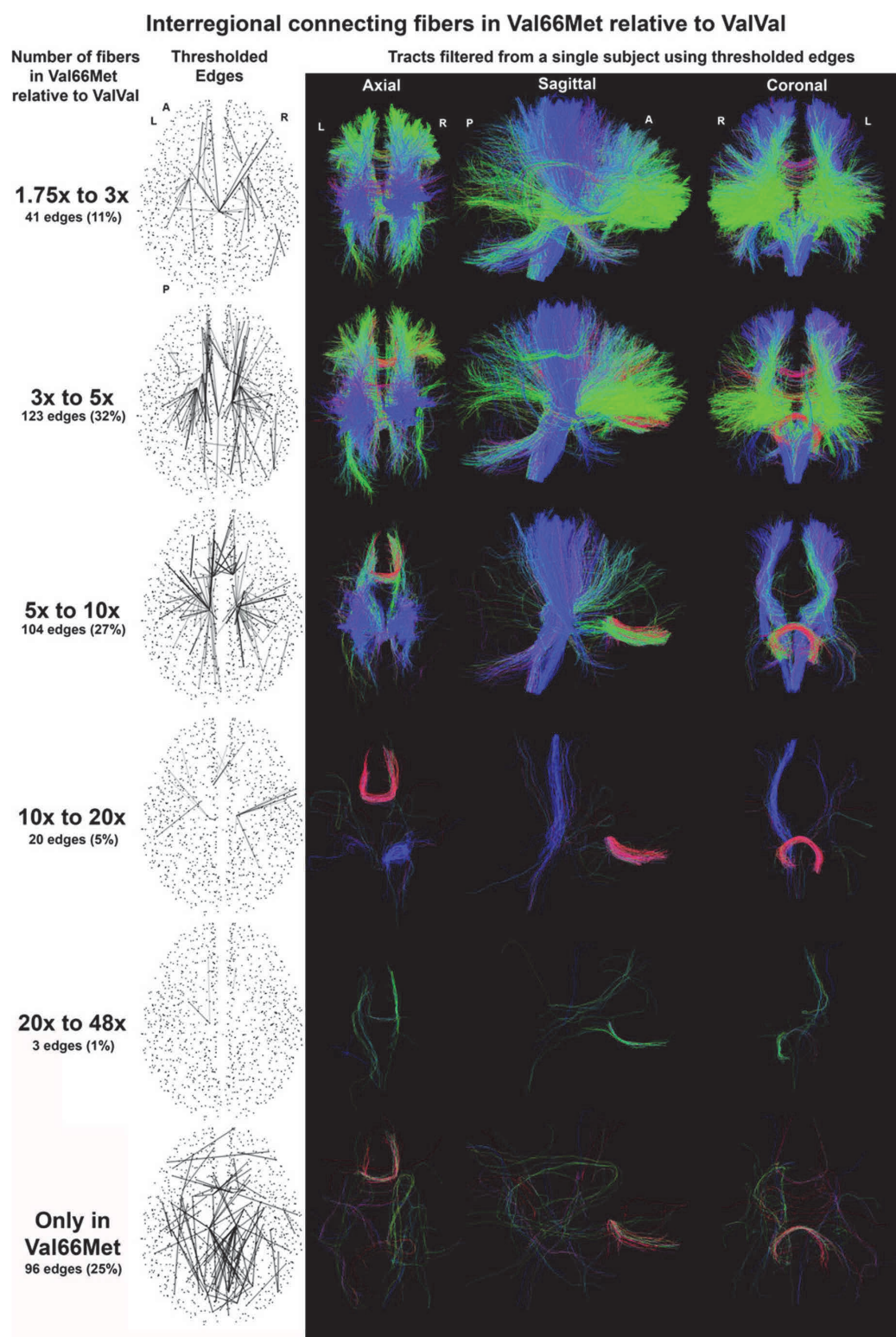
Interregional connecting fibers in Val66Met relative to ValVal

Figure 3. Connecting tracks in Met carriers. The average number of tracks connecting two regions (i.e. the edge weight) in Met carriers was found to range from 1.75 to 48x the value found in the Val/Val group. The range was so broad that it had to be analyzed in separate stages. Fibers shown are filtered from a single Met carrier.
doi:10.1371/journal.pone.0069290.g003

tions and global haplotypic diversity [24]. It is important to note that the Val66Met polymorphism has a wide variation in prevalence worldwide. Its frequency ranges from 0.55% in Sub-Saharan Africa, to 19.9% in Europe, and 43.6% in Asia [24]. Studies including subjects from different populations should take care to consider their genetic backgrounds.

Future research should confirm these findings in healthy populations of both young and old subjects, as well as during the development period from childhood to adolescence. Longitudinal neuroimaging data would clarify BDNF's effect on brain development and connectivity, and larger populations may help identify whether these changes can be fully attributed to the Met allele. It also remains to be seen if these alterations are more or less profound in Met homozygotes or in subjects with the Val66Met polymorphism. The prevalence of the Met allele [24,25] suggests that it confers some evolutionary advantages. It may be that these advantages, developed during preadolescence, are only manifested in old age.

Methods

Ethics Statement

Volunteers were recruited through advertisement on the University intranet. They gave their written informed consent to participate in the study, which was approved by the Ethics Committee of the Faculty of Medicine at the University of Liège.

Population

Participants were young (18–25 years old), healthy, and lean (Body Mass Index <26). They were all right-handed, as determined by the Edinburgh Inventory [26]. None complained about sleep disturbances, and this was reflected by the Pittsburgh Sleep Quality Index (PSQI score <6) [27]. Extreme chronotypes, according to the Horne and Ostberg morningness-eveningness questionnaire, were excluded (scores <31 or >69) [28]. Their sleep midpoint on free days was required to be between 3 and 5.99 as indicated by the Munich Chronotype Questionnaire [29]. They all scored in the normal range (0–9) on the Epworth Sleepiness Scale [30]. The absence of medical, traumatic, psychiatric, and sleep disorders was established through a semi-structured interview.

All participants had normal scores on the 21-item Beck Anxiety Inventory (score <11) and the 21-item Beck Depression Inventory-II (score <14) [31,32]. They were non-smokers and moderate caffeine and alcohol consumers. None were on medication other than oral contraceptives. No caffeine was allowed during the experiment.

Volunteers complying with these criteria were invited to perform Raven's Progressive Matrices and a blood sample was obtained for *BDNF* genotyping [33]. Participants were eventually selected based on their *BDNF* genotype. Allelic groups were formed with participants that were matched according to gender, age, education level, chronotype, PSQI score and IQ (**Table S1 in File S1**). Subjects received financial compensation for their blood test and participation in the study.

Genotyping

Genomic DNA was extracted from blood samples using a MagNA Pure LC Instrument. The DNA sequence of interest was amplified by Polymerase Chain Reaction in a final volume of 50 μl containing 0.6 μM of each primer (Thermo Scientific,

Germany), 0.5 μl Faststart Taq DNA Polymerase (Roche Diagnostics, Germany), 0.8 mM of each deoxynucleotide triphosphate (Roche Diagnostics Germany) and 20 ng of genomic DNA. After 10 min of denaturation at 95°C, samples underwent 35 cycles consisting of denaturation (95°C, 30 sec), annealing (60°C, 40 sec), and extension (72°C, 30 sec), followed by a final extension of 7 min at 72°C. The amplified DNA product was then subjected to pyrosequencing (Pyromark Q96 Vacuum Workstation, PSQ 96MA, Pyromark Gold Q96 Reagents, Qiagen, Germany). The sequences of the primers are available upon request.

Data Acquisition

Data was acquired on a 3 T head-only scanner (Magnetom Allegra, Siemens Medical Solutions, Erlangen, Germany) operated with the standard transmit-receive quadrature head coil. A high-resolution T1-weighted image was acquired for each subject (3D modified driven equilibrium Fourier transform, repetition time = 7.92 ms, echo time = 2.4 ms, inversion time = 910 ms, flip angle = 15°, field of view = $256 \times 224 \times 176$ mm^3, 1 mm isotropic spatial resolution). Seven unweighted (b = 0) volumes were acquired followed by a set of diffusion-weighted (b = 1000) images using 61 non-collinear directional gradients.

Processing & Analysis

The processing workflow was developed in Python and imports modules from the Nipype project [34]. The pipelines used for both single subjects and groups have been detailed as part of the online Nipype documentation in order to improve transparency and promote reproducibility. Every piece of software (CMTK, ConnectomeViewer, Dipy, Freesurfer, FSL, Nipype, Nibabel, MRtrix) used to process data in this paper is currently operating under an open-source license. The process began by segmenting the structural MR images using the automated labeling of Freesurfer [15]. Segmented structural images were then further parcellated using the Lausanne2008 atlas for a total of 1015 regions of interest (ROIs) [14]. Diffusion-weighted images were corrected for image distortions arising from eddy currents using linear coregistration functions from the FMRIB Software Library (FSL) [35]. Fractional anisotropy maps were generated, and a small number of single-fiber (high FA) voxels were used to estimate the spherical harmonic coefficients of the response function from the diffusion-weighted images [36,37]. Using non-negativity constrained spherical deconvolution, fiber orientation distribution (FOD) functions were obtained at each voxel. For our dataset with 61 directions, we used the maximum allowable harmonic order of 8 for both the response estimation and spherical deconvolution steps. Probabilistic tractography was performed throughout the whole brain using seeds from subject-specific white-matter masks and a predefined number of tracts. Fiber tracking settings were as follows: number of tracks = 300,000, FA/FOD amplitude cutoff for terminating tracks = 0.1, minimum track length = 10 mm, maximum track length = 200 mm, minimum radius of curvature = 1 mm, tracking algorithm step size = 0.2 mm. Using tools from Dipy (Diffusion in Python, http://nipy.sourceforge.net/dipy/), the tracks were affine-transformed into the subject's structural space. This procedure circumvents the common problem of having to downsample ROI image files – defined in structural space – so

that they can be used in diffusion space for connectivity mapping, and therefore leads to more accurate connectomes. Connectome mapping was performed by considering every contact point between each tract and the outlined regions of interest. Unlike in some past papers (e.g. [14,16]) which considered only fiber start and endpoints, we incremented our connectivity matrix every time a single fiber traversed between any two regions. This leads to a far denser network than we have seen before, presumably with more accurate network properties. The number of tracked fibers which remained in each subject's connectome was also recorded.

This method of connection mapping may need further optimisation, however, as it can potentially be linking gray matter cortical regions through unreliably tracked fibers. This is something that may be avoidable by placing limits on the propagation parameters, or with anatomically or otherwise constrained tractography approaches [38,39]. The benefits and drawbacks of different mapping techniques should be explored by future studies.

Numerous network metrics were obtained for each connectome and compared at the group level. At the nodal level we calculated the degree, clustering coefficient, and number of triangles, as well as three measures of centrality (closeness, betweenness, degree), and the highest k (i.e. degree) value for each k-core the node is encompassed by. For the network as a whole we computed the average shortest path length (i.e. the inverse of efficiency), the wiring cost (using Euclidean distance between nodes), the graph density, the number of connected components, and the graph's transitivity [40]. For a complete description of all of these metrics, the reader is referred to the Python package NetworkX [41]. Tract and network visualization were performed in TrackVis (Ruopeng Wang, Van J. Wedeen, TrackVis.org, Martinos Center for Biomedical Imaging, Massachusetts General Hospital), MRtrix, and ConnectomeViewer [42]. **Figure S2** provides, for visualization, the orientation distribution functions and generated fiber tracts for a midbrain coronal slice of a single subject. In **Figure S3**, the structural connectome and T1-weighted image are shown for the same subject, and thresholded across two distinct fiber-count ranges, so that both the core and the density of the network can be seen.

Statistical Analysis

The Network-based Statistic (NBS) was used to identify differences between *BDNF* allelic groups (**Fig. S1a**) [11]. For each permutation the t-values at each edge were thresholded above a value of 3. The supra-threshold components were then compared against the generated null distribution. The null distribution for each test was produced by permuting members of each population 5000 times and estimating the maximal component size.

A table describing a representative subject's connection matrix and edge weights is given in **Table S2 in File S1**. Since the networks in this study have a high number of regions, and we have performed whole-brain connectome mapping with a relatively low number of fibers, a large proportion of our network's edges have low fiber counts. This may be problematic for statistical testing with the NBS because these small-integer populations do not provide wide ranges for edge weights and can result in inaccurate t-values. In future, it may be prudent to generate a larger number of streamlines, reduce the number of nodes in the network, or restrict analysis to specific parts of the brain. Practically, it can be computationally intensive to deal with large streamline datasets and networks with high numbers of nodes. The trade-off between resolution and resources is something that must be decided by the researcher with the focus of the study in mind.

In **Fig. S1b** we projected the observed NBS component onto the tractography of a single subject. This projection is, in effect, a type of reverse connectome-mapping. Given the connectivity network, we filtered the set of tracts to show only those that traverse between regions with edges in the network. Global graph metrics, psychological metrics, and the total number of fibers per connectome, were compared directly between allelic groups via Student's t-test. Nodal measures were averaged for each subject and analyzed in the same manner. All distributions were plotted as combined histogram/kernel-density maps to evaluate gaussianity prior to statistical analysis. Apart from the results given by the network-based statistic, no significant differences were identified between the two genotypic groups for any of the graph-level measures. No significant differences were observed between allelic groups in any of the psychological metrics.

Classification

The multivariate statistical properties of our data were studied with a linear Gaussian Process Classification method [43] as interfaced by PRoNTo (Pattern Recognition for Neuroimaging Toolbox, http://www.mlnl.cs.ucl.ac.uk/pronto) [44]. The classifier was given the fiber-count connection matrices for each subject and their true classes (e.g. Met carrier, Female). No network metrics, topology, or spatial information was provided to the classifier. The accuracy and generalisability of the classification were assessed with a leave-one-out cross-validation procedure: one subject is left out at a time, the classifier is trained on the remaining data, and the true and predicted (by the trained classifier) classes of the left-out subject are compared. With this linear kernel method weights were also obtained indicating the contribution to the classification output (in favor of either genotypic group) of each edge in the network. The same method was employed to discriminate features related to the subjects' gender and genotype for the ADA gene. For the purposes of visualization, we thresholded the edges in **Figure 2**. The removed portion of the classification weights can be found in **Fig. S4**. Example calculations for the percent classification weight represented by the remaining edges can be found in the Supplementary Information in File S1.

Supporting Information

Figure S1   Edge weights are stronger in Met carriers. (**a**) In the structural component pictured each inter-regional connection has a significantly higher number of tracks for Met carriers. (**b**) The tracks shown are produced by filtering a single subject's tracts using the connections from the network shown in (**a**). (TIF)

Figure S2   Tracks and Orientation Distribution Functions for a single subject. Combined figure for visualizing the results of the spherical deconvolution and probabilistic fiber tractography steps in the processing pipeline. (TIF)

Figure S3   Structural connectome for a single subject. Structural connectivity network built from the Lausanne 2008 regional atlas – with each region displayed as a node – and a set of 300,000 fiber tracks. Colored edge weights represent the number of tracks that provide any connection between any pair of regions. The figure is divided into ranges of edge weights for optimal visualization of the (**a**) high-valued structural core and the (**b**) low-valued associative connections. (TIF)

Figure S4 Detailed dissection of the classification weights. (**a**) The complement of Figure 2 from the main text. This network details the edges that were filtered in the main text figure, and shows 99.75% of the edges, which represent only 78% of the total weight. (**b**) A set of very low contribution edges between genotypic groups. These very low-valued edges are difficult to interpret. (**c**) The highest valued edges that were thresholded out of Figure 2 in the main text. A pattern of posterior parietal and medial frontal connectivity can be inferred in the Met carriers, but the abundance of edges is still complex to visualize. (TIF)

File S1 Table S1– Psychological questionnaire results. Values reflect mean ± standard deviation. **Table S2– Connectome edge weights.** This table details a single random (Val)

subject's network edges. The vast majority of the edges had weights below a fiber count of 100. (PDF)

Author Contributions

Conceived and designed the experiments: PM CP. Performed the experiments: VB VD AF LM VM. Analyzed the data: EZ AL JS CP. Contributed reagents/materials/analysis tools: EZ CP EB. Wrote the paper: EZ AF LM AL JS PM CP.

References

1. Huang EJ, Reichardt LF (2001) Neurotrophins: roles in neuronal development and function. Annu Rev Neurosci 24: 677–736.
2. Patterson SL, Abel T, Deuel TA, Martin KC, Rose JC, et al. (1996) Recombinant BDNF rescues deficits in basal synaptic transmission and hippocampal LTP in BDNF knockout mice. Neuron 16: 1137–1145.
3. Bekinschtein P, Cammarota M, Katche C, Slipczuk L, Rossato JI, et al. (2008) BDNF is essential to promote persistence of long-term memory storage. Proc Natl Acad Sci U S A 105: 2711–2716.
4. Egan MF, Kojima M, Callicott JH, Goldberg TE, Kolachana BS, et al. (2003) The BDNF val66met polymorphism affects activity-dependent secretion of BDNF and human memory and hippocampal function. Cell 112: 257–269.
5. Cheeran B, Talelli P, Mori F, Koch G, Suppa A, et al. (2008) A common polymorphism in the brain-derived neurotrophic factor gene (bdnf) modulates human cortical plasticity and the response to rtms. J Physiol 586: 5717–5725.
6. Goldberg TE, Iudicello J, Russo C, Elvevg B, Straub R, et al. (2008) Bdnf val66met polymorphism significantly affects d' in verbal recognition memory at short and long delays. Biol Psychol 77: 20–24.
7. Hong CJ, Liou YJ, Tsai SJ (2011) Effects of BDNF polymorphisms on brain function and behavior in health and disease. Brain Res Bull 86: 287–297.
8. Pezawas L, Verchinski BA, Mattay VS, Callicott JH, Kolachana BS, et al. (2004) The brain-derived neurotrophic factor val66met polymorphism and variation in human cortical morphology. J Neurosci 24: 10099–10102.
9. Hilgetag CC, Grant S (2000) Uniformity, specificity and variability of corticocortical connectivity. Philos Trans R Soc Lond B Biol Sci 355: 7–20.
10. Fornito A, Zalesky A, Bassett DS, Meunier D, Ellison-Wright I, et al. (2011) Genetic influences on cost-efficient organization of human cortical functional networks. J Neurosci 31: 3261–3270.
11. Zalesky A, Fornito A, Bullmore ET (2010) Network-based statistic: identifying differences in brain networks. Neuroimage 53: 1197–1207.
12. Chiang MC, Barysheva M, Toga AW, Medland SE, Hansell NK, et al. (2011) BDNF gene effects on brain circuitry replicated in 455 twins. Neuroimage 55: 448–454.
13. Zalesky A, Fornito A, Harding IH, Cocchi L, Ycel M, et al. (2010) Whole-brain anatomical networks: does the choice of nodes matter? Neuroimage 50: 970–983.
14. Cammoun L, Gigandet X, Meskaldji D, Thiran JP, Sporns O, et al. (2012) Mapping the human connectome at multiple scales with diffusion spectrum mri. J Neurosci Methods 203: 386–397.
15. Desikan RS, Sgonne F, Fischl B, Quinn BT, Dickerson BC, et al. (2006) An automated labeling system for subdividing the human cerebral cortex on MRI scans into gyral based regions of interest. Neuroimage 31: 968–980.
16. Hagmann P, Cammoun L, Gigandet X, Meuli R, Honey CJ, et al. (2008) Mapping the structural core of human cerebral cortex. PLoS Biol 6: e159.
17. Daducci A, Gerhard S, Griffa A, Lemkaddem A, Cammoun L, et al. (2012) The connectome mapper: an open-source processing pipeline to map connectomes with mri. PLoS One 7: e48121.
18. Singh KK, Park KJ, Hong EJ, Kramer BM, Greenberg ME, et al. (2008) Developmental axon pruning mediated by BDNF-p75NTR-dependent axon degeneration. Nat Neurosci 11: 649–658.
19. Cao L, Dhilla A, Mukai J, Blazeski R, Lodovichi C, et al. (2007) Genetic modulation of BDNF signaling affects the outcome of axonal competition in vivo. Curr Biol 17: 911–921.
20. Gogtay N, Giedd JN, Lusk L, Hayashi KM, Greenstein D, et al. (2004) Dynamic mapping of human cortical development during childhood through early adulthood. Proc Natl Acad Sci U S A 101: 8174–8179.
21. Harris SE, Fox H, Wright AF, Hayward C, Starr JM, et al. (2006) The brain-derived neurotrophic factor Val66Met polymorphism is associated with age-related change in reasoning skills. Mol Psychiatry 11: 505–513.
22. Gajewski PD, Hengstler JG, Golka K, Falkenstein M, Beste C (2011) The Met-allele of the BDNF Val66Met polymorphism enhances task switching in elderly. Neurobiol Aging 32: 2327. e7–2327.19.
23. Mandelman SD, Grigorenko EL (2012) BDNF Val66Met and cognition: all, none, or some? A meta-analysis of the genetic association. Genes Brain Behav 11: 127–136.
24. Petryshen TL, Sabeti PC, Aldinger KA, Fry B, Fan JB, et al. (2010) Population genetic study of the brain-derived neurotrophic factor (BDNF) gene. Mol Psychiatry 15: 810–815.
25. Shimizu E, Hashimoto K, Iyo M (2004) Ethnic difference of the BDNF 196G/A (val66met) polymorphism frequencies: the possibility to explain ethnic mental traits. Am J Med Genet B Neuropsychiatr Genet 126B: 122–123.
26. Oldfield RC (1971) The assessment and analysis of handedness: the Edinburgh inventory. Neuropsychologia 9: 97–113.
27. Buysse DJ, Reynolds C 3rd, Monk TH, Berman SR, Kupfer DJ (1989) The Pittsburgh Sleep Quality Index: a new instrument for psychiatric practice and research. Psychiatry Res 28: 193–213.
28. Horne JA, Ostberg O (1976) A self-assessment questionnaire to determine morningness-eveningness in human circadian rhythms. Int J Chronobiol 4: 97–110.
29. Roenneberg T, Wirz-Justice A, Merrow M (2003) Life between clocks: daily temporal patterns of human chronotypes. J Biol Rhythms 18: 80–90.
30. Johns MW (1991) A new method for measuring daytime sleepiness: the Epworth sleepiness scale. Sleep 14: 540–545.
31. Beck AT, Epstein N, Brown G, Steer RA (1988) An inventory for measuring clinical anxiety: psychometric properties. J Consult Clin Psychol 56: 893–897.
32. Steer RA, Ball R, Ranieri WF, Beck AT (1997) Further evidence for the construct validity of the Beck depression Inventory-II with psychiatric outpatients. Psychol Rep 80: 443–446.
33. Raven J, Raven JC, Court JH (1998) Manual for Raven's Progressive Matrices and Vocabulary Scales. Oxford, U.K: Oxford Psychologists Press.
34. Gorgolewski K, Burns CD, Madison C, Clark D, Halchenko YO, et al. (2011) Nipype: a exible, lightweight and extensible neuroimaging data processing framework in python. Front Neuroinform 5: 13.
35. Smith SM, Jenkinson M, Woolrich MW, Beckmann CF, Behrens TEJ, et al. (2004) Advances in functional and structural MR image analysis and implementation as FSL. Neuroimage 23 Suppl 1: S208–S219.
36. Tournier JD, Calamante F, Gadian DG, Connelly A (2004) Direct estimation of the fiber orientation density function from diffusion-weighted MRI data using spherical deconvolution. Neuroimage 23: 1176–1185.
37. Tournier JD, Calamante F, Connelly A (2007) Robust determination of the fibre orientation distribution in diffusion MRI: non-negativity constrained super-resolved spherical deconvolution. Neuroimage 35: 1459–1472.
38. Smith RE, Tournier JD, Calamante F, Connelly A (2012) Anatomically-constrained tractography: improved diffusion mri streamlines tractography through effective use of anatomical information. Neuroimage 62: 1924–1938.
39. Smith RE, Tournier JD, Calamante F, Connelly A (2013) Sift: Spherical-deconvolution informed filtering of tractograms. Neuroimage 67: 298–312.
40. Rubinov M, Sporns O (2010) Complex network measures of brain connectivity: uses and interpretations. Neuroimage 52: 1059–1069.
41. Hagberg AA, Schult DA, Swart PJ (2008) Exploring network structure, dynamics, and function using NetworkX. In: Proceedings of the 7th Python in Science Conference (SciPy2008). Pasadena, CA USA, 11–15.
42. Gerhard S, Daducci A, Lemkaddem A, Meuli R, Thiran JP, et al. (2011) The connectome viewer toolkit: an open source framework to manage, analyze, and visualize connectomes. Front Neuroin form 5: 3.
43. Rasmussen CE, Williams CKI (2005) Gaussian Processes for Machine Learning (Adaptive Computation and Machine Learning). The MIT Press.
44. Schrouff J, Rosa MJ, Rondina JM, Marquand AF, Chu C, et al. (2013) Pronto: Pattern recognition for neuroimaging toolbox. Neuroinformatics.

Supplementary Information for Altered white matter architecture in BDNF Met carriers

Erik Ziegler[1,*], Ariane Foret[1], Laura Mascetti[1], Vincenzo Muto[1], Anahita Le Bourdiec-Shaffii[1], Johan Stender[1], Evelyne Balteau[1], Vinciane Dideberg[2], Vincent Bours[2], Pierre Maquet[1,3], Christophe Phillips[1,4]

1 Cyclotron Research Centre, Université de Liège, Liège, Belgium, Liège, Liège, Belgium
2 Department of Human Genetics, CHU Sart Tilman, Liège, Belgium
3 Department of Neurology, CHU Liège, Liège, Belgium
4 Department of Electrical Engineering and Computer Science, University of Liège, Belgium
∗ **E-mail: erik.ziegler@ulg.ac.be**

The following equations and figures are supplementary material.

The networks in our study have 1015 anatomically defined nodes. This leads to:

$$
\begin{aligned}
N_{edges} &= \frac{N_{nodes} * (N_{nodes} - 1)}{2} \\
N_{edges} &= \frac{1015 * (1015 - 1)}{2} \\
N_{edges} &= 514,605
\end{aligned}
\tag{1}
$$

The total of all the classifier weights was obtained by summing the absolute value of all the weights:

$$
\begin{aligned}
W_{total} &= \sum_{i=0, j=0}^{N_{nodes}} |W_{i,j}| \\
&= 2077.6096558590079
\end{aligned}
\tag{2}
$$

For each of the thresholding windows we calculated the percent of total weight represented. For example, in Figure 2 of the main text, we calculated the weight and amount of edges using the following method. First, we defined a binarizing threshold function to obtain the number of edges:

$$
f(x) = \begin{cases} 1 & x \text{ if } -0.1 \leq n \leq 0.1 \\ 0 & x \text{ if } n > 0.1 \text{ or } n < -0.1 \end{cases}
\tag{3}
$$

Next, we used this to obtain the total number of thresholded edges, and their percent of the total edges.

$$
N_{edges}^{thresh} = \sum_{i=0, j=0}^{N_{nodes}} f(W_{i,j})
\tag{4}
$$

The percent of edges that remain are simply:

$$
\begin{aligned}
Percent_{edges}^{thresh} &= \frac{N_{edges}^{thresh}}{N_{edges}} * 100 \\
Percent_{edges}^{thresh} &= \frac{1302}{514605} \\
Percent_{edges}^{thresh} &= 0.25\%
\end{aligned}
\tag{5}
$$

The total weight of the edges that are within the threshold regions can be obtained similarly:

$$
W_{total}^{thresh} = \sum_{i=0, j=0}^{N_{nodes}} f(W_{i,j}) * |W_{i,j}|
\tag{6}
$$

The percent of the total classifier weight contained within the thresholded edges is therefore:

$$
\begin{aligned}
Percent_{weight}^{thresh} &= \frac{W_{total}^{thresh}}{W_{total}} * 100 \\
Percent_{weight}^{thresh} &= \frac{450.57456206441788}{2077.6096558590079} \\
Percent_{weight}^{thresh} &= 21\%
\end{aligned}
\tag{7}
$$

For future studies it may be simpler to only consider edges that exist in at least one structural network. This will speed classification and make visualization easier. That is to say, the classification should be given a mask that contains only edges that exist in the union of all all subject's networks. This can be expressed mathematically with set theory as:

$$
Mask_{inclusive} = Subj_1 \cup Subj_2 \cup \cdots Subj_n
\tag{8}
$$

Figure Legends
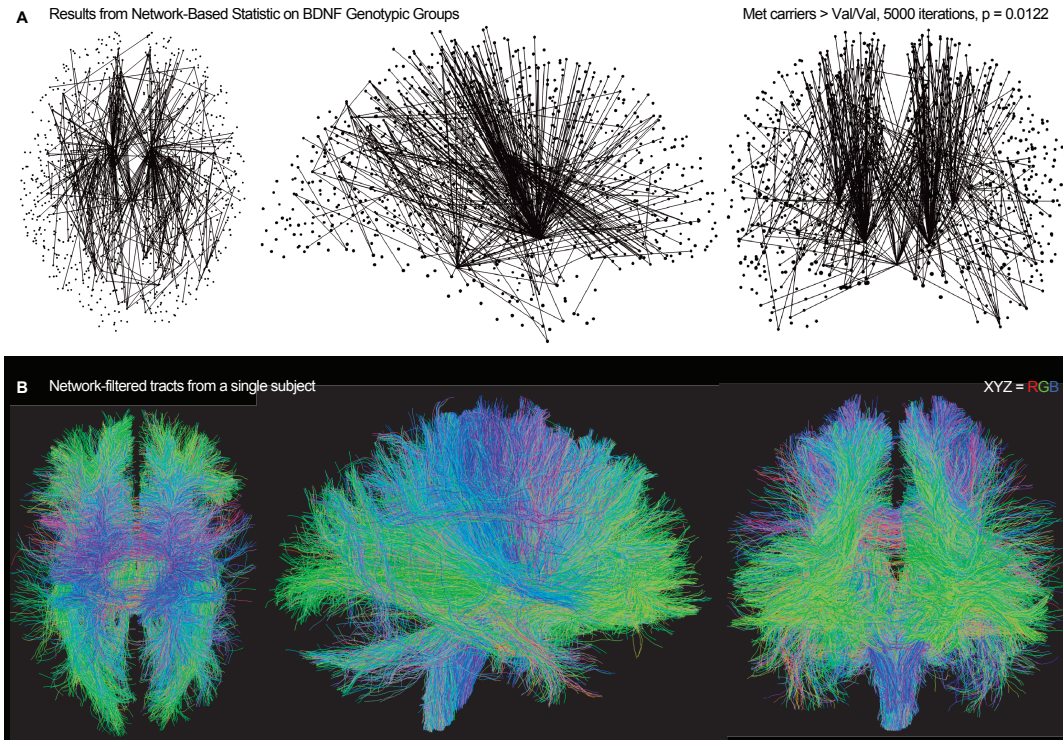
Figure 1. Edge weights are stronger in Met carriers. (**a**) In the structural component pictured each inter-regional connection has a significantly higher number of tracks for Met carriers. (**b**) The tracks shown are produced by filtering a single subject's tracts using the connections from the network shown in (**a**).
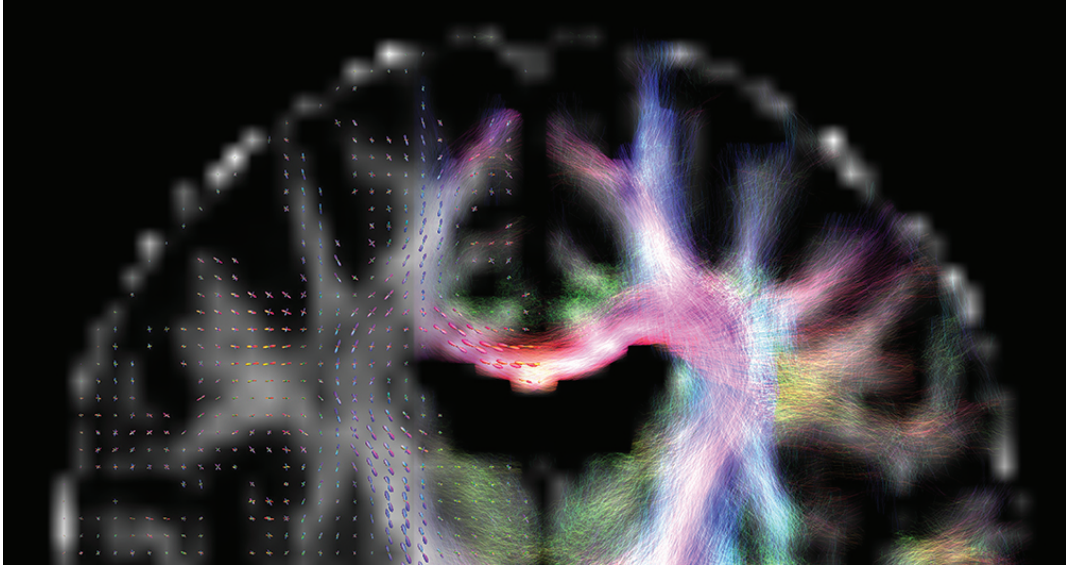
Figure 2. Tracks and Orientation Distribution Functions for a single subject. Combined figure for visualizing the results of the spherical deconvolution and probabilistic fiber tractography steps in the processing pipeline.
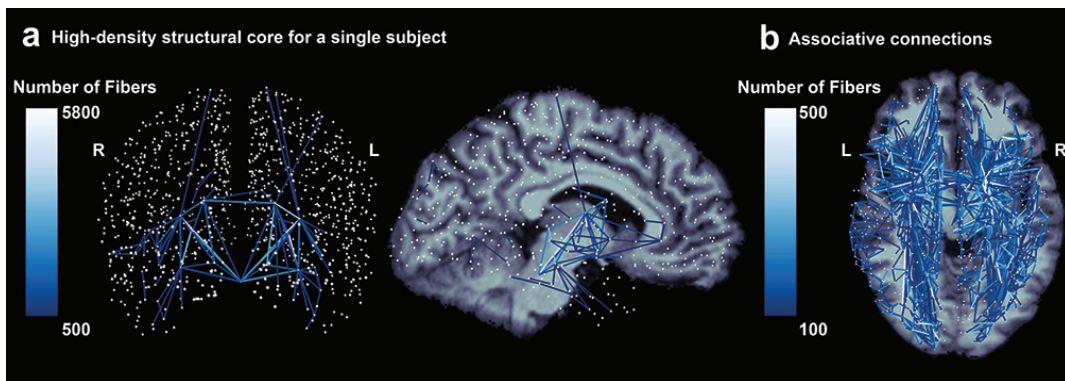
Figure 3. Structural connectome for a single subject. Structural connectivity network built from the Lausanne2008 regional atlas - with each region displayed as a node - and a set of 300,000 fiber tracks. Colored edge weights represent the number of tracks that provide any connection between any pair of regions. The figure is divided into ranges of edge weights for optimal visualization of the (**a**) high-valued structural core and the (**b**) low-valued associative connections.

Tables

4
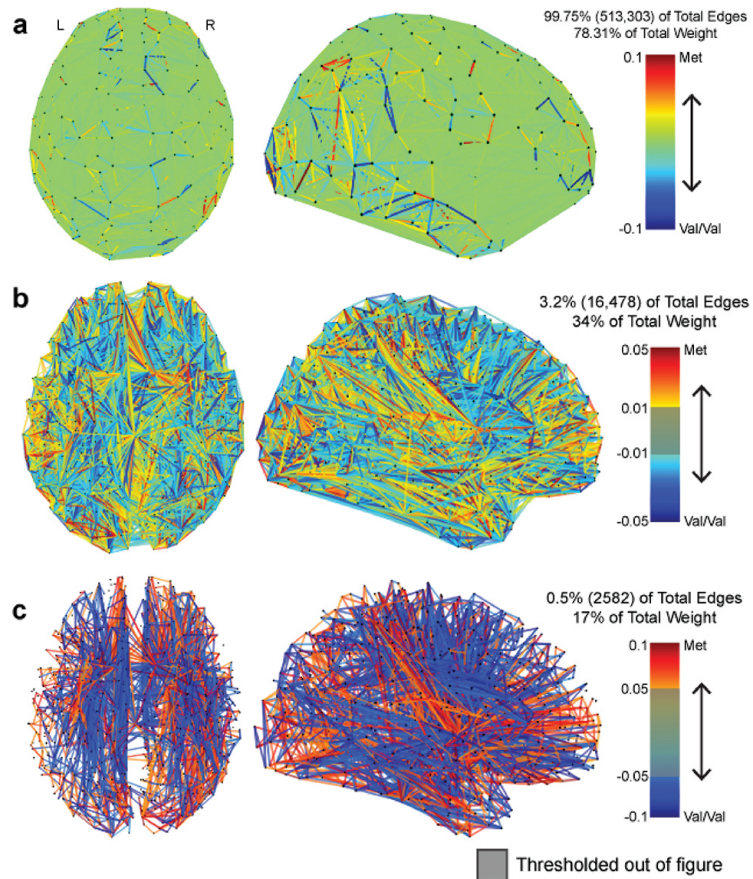
Figure 4. Detailed dissection of the classification weights. (**a**) The complement of Figure 2 from the main text. This network details the edges that were filtered in the main text figure, and shows 99.75% of the edges, which represent only 78% of the total weight. (**b**) A set of very low contribution edges between genotypic groups. These very low-valued edges are difficult to interpret. (**c**) The highest valued edges that were thresholded out of Figure 2 in the main text. A pattern of posterior parietal and medial frontal connectivity can be inferred in the Met carriers, but the abundance of edges is still complex to visualize.

Table 1. Psychological questionnaire results

Measure	Val/Val	Met carriers	t-Test p-Value	Meaning
Age	21.4 ± 1.7	20.4 ± 1.3	0.07	
IQ	55.6 ± 2.5	56.6 ± 2.6	0.26	
Timed IQ	25.2 ± 5.9	27.1 ± 9.6	0.51	
Body Mass Index (BMI)	22.3 ± 1.9	21.4 ± 2.1	0.21	
Beck Anxiety Inventory (BAI)	4.1 ± 2.7	3.9 ± 2.7	0.82	Normal
Beck Depression Inventory (BDI-II)	3.5 ± 4	1.8 ± 2.3	0.14	Normal
Pittsburgh Sleep Quality Index (PSQI)	2.9 ± 1.3	2.9 ± 1.1	0.98	Good Sleep
Horne-Osberg Chronotype (HO)	53.4 ± 6.5	56.1 ± 7.6	0.27	Neutral Chronotype
Munich Chronotype	4.3 ± 0.7	4.1 ± 0.4	0.58	Normal
Epworth Sleepiness Scale	5.2 ± 2.3	5.8 ± 3.4	0.59	Normal

Values reflect mean $\pm$ standard deviation

Table 2. Connectome edge weights

Measure	Value
Number of Edges	65,785
Graph density	12.78%
Minimum Edge Weight	1
Maximum Edge Weight	4737
Total Edge Weight	802,470
Mean Edge Weight	12.2
Standard Deviation in Edge Weight	55.8
Percent of Edges with Weight = 1	41.2%
Percent of Edges with Weight = 2	14.6%
Percent of Edges with Weight = 3	8.1%
Percent of Edges with Weight <= 5	72.9%
Percent of Edges with Weight < 100	97.6%
Percent of Edges with Weight >= 100	2.4%

This table details a single random (Val) subject's network edges. The vast majority of the edges had weights below a fiber count of 100.

Table A.1: Results from Difference (t-test) and Equivalence (TOST) Analysis

Global measures	Different *p* (Met > ValVal)	Equivalent *p* (Met ~ ValVal)
Connected Components	0.7869	0.0028**
Density	0.9636	0.0036**
Efficiency	0.8634	0.0074**
Transitivity	0.8567	0.0043**
Connected Fibers (%)	0.1559	0.0507
Averaged nodal measures		
Betweenness Centrality	0.9493	0.0043**
Closeness Centrality	0.9064	0.0161*
Load Centrality	0.9492	0.0033**
Clustering	0.0639	0.3280
Core Number	0.6294	0.0091**
Degree	0.7027	0.0061**
Triangles	0.9015	0.0018**

Measures above the double line were computed globally, while measures below were computed at the node level and averaged across all nodes for each subject. The majority of network metrics are statistically equivalent, except those that reflect an increase in fiber count between regions. *: $p < 0.05$, **: $p < 0.01$. TOST = two one-sample test.

Paper II

Mapping track density changes in nigrostriatal and extranigral pathways in Parkinson's disease

Ziegler, E., Rouillard, M., André, E., Coolen, T.,
Stender, J., Balteau, E., Phillips, C.*, Garraux, G.*

* Contributed equally

Mapping track density changes in nigrostriatal and extranigral pathways in Parkinson's disease ☆

Erik Ziegler [a], Maud Rouillard [b], Elodie André [a], Tim Coolen [b], Johan Stender [a], Evelyne Balteau [a], Christophe Phillips [a,c,*,1], Gaëtan Garraux [b,d,1]

[a] Cyclotron Research Centre, University of Liège, Liège, Belgium
[b] MoVeRe Group, Cyclotron Research Centre, University of Liège, Liège, Belgium
[c] Department of Electrical Engineering and Computer Science, University of Liège, Liège, Belgium
[d] Department of Neurology, University of Liège, Liège, Belgium

ARTICLE INFO

ABSTRACT

In Parkinson's disease (PD) the demonstration of neuropathological disturbances in nigrostriatal and extranigral brain pathways using magnetic resonance imaging remains a challenge. Here, we applied a novel diffusion-weighted imaging approach—track density imaging (TDI).

Twenty-seven non-demented Parkinson's patients (mean disease duration: 5 years, mean score on the Hoehn & Yahr scale = 1.5) were compared with 26 elderly controls matched for age, sex, and education level. Track density images were created by sampling each subject's spatially normalized fiber tracks in 1 mm isotropic intervals and counting the fibers that passed through each voxel. Whole-brain voxel-based analysis was performed and significance was assessed with permutation testing.

Statistically significant increases in track density were found in the Parkinson's patients, relative to controls. Clusters were distributed in disease-relevant areas including motor, cognitive, and limbic networks. From the lower medulla to the diencephalon and striatum, clusters encompassed the known location of the locus coeruleus and pedunculopontine nucleus in the pons, and from the substantia nigra up to medial aspects of the posterior putamen, bilaterally.

The results identified in brainstem and nigrostriatal pathways show a large overlap with the known distribution of neuropathological changes in non-demented PD patients. Our results also support an early involvement of limbic and cognitive networks in Parkinson's disease.

© 2014 Elsevier Inc. All rights reserved.

Introduction

Parkinsonism is clinically defined by the presence of motor slowness with muscle rigidity, and/or tremor, and/or postural instability (Gibb, 1988). The most common cause of degenerative Parkinsonism in adults is Parkinson's disease. The main motor features of Parkinson's disease stem from the death of pigmented neurons in the substantia nigra (SN). Neuronal loss begins in the ventrolateral SN and this remains the most severely affected region throughout the illness (Damier et al., 1999a; Fearnley and Lees, 1991). As the disease progresses, pathology extends into the dorsal tier of the nigra and ventral tegmental area (Fearnley and Lees, 1994). Post-mortem studies have shown that the loss of cells in these regions results in profound dopamine (DA) depletion in the motor region of the striatum (Kish et al., 1988), with nigral projections to the dorsal and caudal putamen being most affected. A post-mortem diagnosis of Parkinson's disease requires evidence of cell loss in the SN, as well as the presence of Lewy pathology—a term that describes variously shaped insoluble intraneuronal deposits that contain misfolded α-synuclein. These aggregated α-synuclein deposits accumulate in neurites (Lewy neurites) and in neuronal somata (Lewy bodies). Furthermore, neuropathological abnormalities can be observed in other brainstem nuclei such as the pedunculopontine nucleus, locus coeruleus, and raphe nucleus (Gesi et al., 2000; Halliday et al., 1990;

Jellinger, 1991; Zweig et al., 1993), and may extend up to the basal fore-brain and cerebral cortex, possibly according to a predictable spatiotemporal pattern (Braak et al., 2003a, 2003b).

In vivo nigral and extranigral imaging biomarkers of Parkinson's disease are highly sought after for many reasons. Candidate biomarkers may aid premotor diagnosis and help differentiate Parkinson's disease from look-alike conditions such as essential tremor and atypical Parkinsonian syndromes. Perhaps more importantly, reliable imaging biomarkers may aid the development of disease-modifying therapies, as they can be used to monitor disease progression.

To date, no *in vivo* brain imaging modality has adequately captured the widespread spatial spectrum of brain abnormalities in non-demented patients with Parkinson's disease. Because a biochemical hallmark of Parkinson's disease is a deficiency of striatal DA, many imaging studies have focused on studying the problem directly. Measurement of striatal [^{18}F]-L-dihydroxyphenylalanine (^{18}F-DOPA) uptake with positron emission tomography (PET) is regarded by many as the "gold standard" for diagnosis of Parkinson's disease. However, while decreased ^{18}F-DOPA uptake may also be observed in other brainstem regions and cortical areas (Pavese et al., 2012), it is generally acknowledged that it does not reveal the whole range of extranigral pathological abnormalities.

Despite recent advances in brain imaging, extranigral abnormalities remain difficult to capture *in vivo* in non-demented Parkinson's patients. As routine MRI is typically unremarkable in Parkinson's disease, the use of more advanced techniques is warranted. In this paper, we used track density imaging, an advanced diffusion-weighted imaging (DWI) method that allows the mapping of cerebral fiber pathways at a spatial resolution smaller than the voxel size of the original MRI (Calamante et al., 2010).

Diffusion-weighted imaging allows for the quantification of water mobility within tissue. In DWI analysis the movement of water within each voxel is modeled (e.g. using a tensor) and used for further analysis. To date, most studies have relied on scalar measures derived from the diffusion tensor model, such as fractional anisotropy (FA) and mean diffusivity (MD), which quantify the degree of anisotropy and average magnitude of local water diffusion, respectively. Most previous DWI studies in Parkinson's disease used FA and MD on focused regions of interest defined *a priori*, usually in the substantia nigra (Chan et al., 2007; Vaillancourt et al., 2009; Yoshikawa et al., 2004; Zhan et al., 2011). In general, results show decreased FA in Parkinson's patients compared to controls. Studies in rat (Soria et al., 2011) and mouse (Boska et al., 2007) models of Parkinson's disease have also reported similar decreases. Other studies using methods like tract-based spatial statistics, voxel-based FA analysis, and ROIs outside the substantia nigra, have resulted in less consistent reports. Changes in tensor-derived measures have been reported in the gyrus rectus (Ibarretxe-Bilbao et al., 2010), the genu of the corpus callosum, the superior longitudinal fasciculus (Gattellaro et al., 2009), as well as motor and frontal cortices (Zhan et al., 2011). As these past studies have relied on DWI sequences with relatively low numbers of unique gradient directions [6 to 64, (Cochrane and Ebmeier, 2013)], they may have lacked the sensitivity to show disturbances using unbiased voxel-based analyses.

Here we acquired data in 27 non-demented Parkinson's disease patients and 26 matched controls using an advanced DWI sequence, in which 120 diffusion gradients were applied, allowing for the fitting of higher order models of the signal in each voxel. We reconstructed white matter streamlines from DWI images with constrained spherical deconvolution, which generally provides far greater accuracy than alternatives like single or multi-tensor models (Tournier et al., 2004, 2008). In this paper, when referring to the results of fiber tractography, we will use the terms "fibers," "tracks," and "streamlines" interchangeably, and these should not be confused with actual biological tracts (Jones et al., 2013).

The added value of track-weighted imaging comes from the information obtained by tracking the neural pathways (Calamante et al., 2012b). Track density imaging in essence is just the resampling of the fiber track data into user-specified volumetric data (Calamante et al., 2010). Sampling the tractography dataset with a voxel size smaller than the original diffusion-weighted scan is known as "super-resolution" track-weighted imaging. In the approach presented here – track density imaging (TDI) – the manufactured signal is simply the number of streamlines passing through each voxel (Calamante et al., 2010). A similar approach, average pathlength mapping, has shown promise for evaluating traumatic brain injuries (Pannek et al., 2011). Streamline density imaging has been validated histologically for its ability to resolve white matter boundaries (Calamante et al., 2012a).

The present study also differed from most previous DWI studies by using a whole-brain voxel-based approach, rather than regions-of-interest for data analysis. This allowed us to explore and test for changes in both nigral and extranigral areas in the patients as compared with the control groups. Based on the spatial distribution of neuropathological abnormalities reported in non-demented Parkinson disease patients, we hypothesized that differences in track density would appear predominantly in the brainstem and nigrostriatal pathways.

Materials and methods

Participants

We studied 27 (14 males) patients clinically diagnosed with Parkinson's disease and 26 (14 males) healthy control subjects from a larger data sample after excluding those with poor quality imaging data. The groups were matched by age, sex, and highest achieved education level. Disease stage within the patient population was assessed in the "on" state using the Hoehn & Yahr scale (Hoehn and Yahr, 1967). Disease severity was evaluated using the Unified Parkinson's Disease Rating Scale (UPDRS) (Fahn and Elton, 1987). Quality of life was estimated using the Parkinson's Disease Questionnaire (PDQ39) (Jenkinson et al., 1997). Subjects were also administered several psychological tests: global cognitive function [Mattis Dementia Rating Scale (Mattis, 1988), MMSE (Folstein et al., 1975), Symbol Digit Modalities test, verbal fluency test], inhibition [Stroop test, random number generation (Jahanshahi et al., 2006)], episodic memory [Rey auditory verbal learning test (Rey, 1958)], updating of working memory [letter running span memory task], cognitive flexibility [Modified Wisconsin Card Sorting Test], visuospatial judgment [Judgment of Line Orientation (Benton et al., 1983)], and anxiety [Hospital Anxiety and Depression Scale (Zigmond and Snaith, 1983)].

Twenty-four of the 27 patients were taking a combination of several classes of drugs: levodopa (immediate and controlled release), nonergot-derived dopamine receptor agonists (Pramipexole, Ropinirole), and a monoamine oxidase B inhibitor (Rasagiline). The remaining 3 patients were not taking any anti-Parkinsonian medications at the time of scanning. Levodopa and dopamine agonist dosages were pooled and summarized as the levodopa equivalent daily dose [LEDD, (Hobson et al., 2002)]. Total daily L-DOPA equivalent dosages ranged from 0 to 900 mg. Demographic and clinical data are summarized in Table 1. Written informed consent was obtained from all participants in accordance with the Declaration of Helsinki. The Ethics Committee of the University of Liège approved the study.

Imaging data acquisition

Data were acquired on a 3 T head-only MR scanner (Magnetom Allegra, Siemens Medical Solutions, Erlangen, Germany) operated with an 8-channel head coil. Diffusion-weighted (DW) images were acquired with a twice-refocused spin-echo sequence with EPI readout at two distinct b-values ($b = 1000$, $b = 2500$ s/mm^2) along 120 encoding gradients that were uniformly distributed in space by an electrostatic repulsion approach (Jones et al., 1999). This sequence is designed specifically to reduce the distortions induced by eddy-currents in the diffusion-weighted images (Reese et al., 2002). For the purposes of

Table 1
Demographics for the study cohort.

	Healthy controls (n = 26)	Parkinson's patients (n = 27)	t-Test, p-value
Age	64 (8)	66 (8)	0.549
Sex (M:F)	14:12	14:13	
Years of education	13 (3)	11 (3)	0.133
ICV (mm^3)	1478 (152)	1516 (148)	0.360
BMI (kg/m^2)	25 (3)	25 (3)	0.660
Hand dominance (L:R)	2:24	2:25	
Hoehn & Yahr stage		1.5 (0.62)	
Most affected side (L:R)		10:17	
Disease duration (years)		5 (3)	
LEDD (mg)		323 (255)	
UPDRS Section 2		9 (6)	
UPDRS Section 3		14 (7)	
Mattis	139 (4)	136 (4)	0.004
MMSE	29 (1)	28 (1)	0.022
HADS total	10 (4)	13 (6)	0.066
PDQ39 mobility		20 (18)	
PDQ39 total		189 (114)	
Rey Auditory Verbal Learning Test	53 (11)	44 (11)	0.006
SDMT	51 (10)	45 (12)	0.062
JOLO	27 (4)	25 (4)	0.055

Values reflect mean (st. dev.). Two-tail t-tests were performed with an assumption of unequal variance in each group. ICV = intracranial volume, BMI = body mass index, LEDD = L-DOPA equivalent daily dose (Hobson et al., 2002), UPDRS = Unified Parkinson's Disease Rating Scale, MMSE = Mini Mental State Examination, HADS = Hospital Anxiety and Depression Scale, PDQ = Parkinson's Disease Questionnaire, SDMT = Symbol Digit Modalities Test, JOLO = Judgment of line orientation test.

motion correction, 22 unweighted ($b = 0$) volumes, interleaved with the DW images, were acquired. Volumes were acquired with a repetition time (TR) of 6800 ms, an echo time (TE) of 91 ms, and a field-of-view (FOV) of 211 mm^2. Maximum slew rate was 400 mT/(m/ms) and maximum gradient amplitude was 40 mT/m. No parallel imaging techniques were used. The multi-channel head coil was used to increase the signal-to-noise ratio, and not the speed of the acquisition. Volumes were acquired with a 6/8 partial Fourier factor. Voxels were isotropic with dimensions of $2.4 \times 2.4 \times 2.4$ mm^3 and volumes were acquired in 54 transverse slices using an 88×88 voxel matrix. Total acquisition time was approximately 35 min. MRI data were acquired while patients were on their usual anti-Parkinsonian medication so they would remain as still as possible in the scanner.

Structural and quantitative maps of T1, T2*, proton density (PD) and magnetization transfer (MT) at $1 \times 1 \times 1$ mm^3 resolution were calculated from a multi-parameter protocol based on a 3D multi-echo fast low angle shot (FLASH) sequence (Weiskopf and Helms, 2008). Three co-localized 3D multi-echo FLASH datasets were acquired with predominantly proton density weighting (PDw: TR/α = 23.7 ms/6°), T1 weighting (T1w: 18.7 ms/20°), and MT weighting (MTw: 23.7 ms/6°; excitation preceded by an off-resonance Gaussian MT pulse of 4 ms duration, 220° nominal flip angle, 2 kHz frequency offset). The PDw acquisition used eight bipolar gradient echoes at equidistant TE between 2.2 ms and 19.7 ms, whereas the T1w and MTw acquisition used six bipolar gradient echoes at equidistant TE between 2.2 ms and 14.7 ms. All three had 425 Hz/pixel bandwidth to avoid susceptibility-related distortions. Volumes were acquired in 176 sagittal slices using a 256×224 voxel matrix. The total acquisition time was approximately 19 min.

A B$_1$ map was calculated using the actual-flip-angle imaging method (Yarnykh, 2007) based on two interleaved 3D FLASH acquisitions (repetition times TR$_1$ = 33 ms, TR$_2$ = 165 ms, TE$_1$ = TE$_2$ = 3.05 ms, nominal flip angle = 60°, acquisition time = 5 min.). The B$_1$ map was used to correct the multiparameter maps for B$_1$ field bias (Volz et al., 2010).

Visual inspection of the raw images was performed to ensure that subject data had no (i) ghosting, (ii) signal dropout, (iii) major motion distortions, or (iv) scanner-induced vibration artifacts (Tournier et al., 2011).

Imaging data processing

Interleaved unweighted images from the diffusion sequence were realigned to the first unweighted volume with a rigid body transformation using SPM8 (Wellcome Trust Centre for Neuroimaging, UCL, UK). Registration was performed (rigid, mutual information) between the first unweighted volume and each of the interleaved unweighted volumes (e.g. register b0$_3$ to b0$_1$). The translation and rotation values between b0$_1$ and b0$_{22}$ were linearly interpolated and applied to the weighted volumes. The assumption behind this procedure is that the subject's displacement was linearly continuous in between unweighted volumes. This put all the weighted images in alignment with the first b0 volume without the contrast problems of co-registering weighted and unweighted images. Diffusion gradient vectors were rotated accordingly (Leemans and Jones, 2009). For each diffusion-weighted volume, a non-local mean filter was applied (Maggioni et al., 2013) and noise was corrected using power image correction adapted for multi-coil acquisitions (André et al., 2014). No further corrections were applied to correct for eddy current-induced distortions in the diffusion-weighted volumes because the diffusion sequence did a sufficient job of suppressing them.

We included motion as a nuisance regressor in our analysis by computing a version of the total motion index (Yendiki et al., 2014) from the rigid transformations between unweighted volumes. We calculated average volume-by-volume translation between unweighted images by averaging the magnitude of the translation vectors between each successive unweighted image. Similarly, average volume-by-volume rotation was computed by averaging the sum of the absolute values of the rotation values between successive unweighted images.

FA and MD maps

A brain mask was generated using the "median Otsu" method as implemented in Dipy (version 0.7.1) (Garyfallidis et al., 2014). In this method, a median filter is applied to smooth the unweighted volume, and then an automated histogram approach is used to separate the foreground and background. Using the low b-value ($b = 1000$ s/mm^2) data, tensors were fit at each voxel using non-linear least squares, and fractional anisotropy and mean diffusivity maps were also generated from the tensors.

TDI maps

The fiber response model was estimated for each subject from the high b-value ($b = 2500$ s/mm^2) diffusion-weighted images. A mask of single fiber voxels was extracted from the thresholded and eroded FA images. Only strongly anisotropic (FA > 0.7) voxels were used to estimate the spherical-harmonic coefficients of the response function (Tournier et al., 2004, 2008). Using non-negativity constrained spherical deconvolution, fiber orientation distribution (FOD) functions were obtained at each voxel.

For both the response estimation and spherical deconvolution steps we chose a maximum harmonic order of 8. Seed masks were created from white matter probability maps, estimated from signal variation in the DWIs,[2] thresholded above 0.4. This threshold was chosen by trial and error, and is in general lower than what would be used on young healthy subjects, possibly due to variations in levels of iron (Graham et al., 2000). Probabilistic tractography was performed using randomly placed seeds within subject-specific white matter masks. Fiber tracking settings were as follows: number of tracks = 5,000,000, FOD magnitude cutoff for terminating tracks = 0.1, minimum track length = 10 mm, maximum track length = 200 mm, minimum radius of curvature = 1 mm, tracking algorithm step size = 0.2 mm.

---

[2] Performed with the "gen_WM_mask" command in MRtrix.

Streamlines were terminated when they (i) extended out of the white matter mask, or (ii) could not progress along a direction with an FOD magnitude or curvature radius higher than the minimum cutoffs.

Spatial normalization of the fiber tracks followed a procedure laid out previously (Pannek et al., 2011). First, track density and total pathlength maps (TPM) were generated with $1 \times 1 \times 1$ mm³ isotropic voxels, and used to create average pathlength maps (TPM/TDI = APM) for each subject. The APMs were then rigidly aligned to the MNI152 1 mm T1 template with mutual information and averaged to create an initial template. The APMs were then used to build a template through 4 iterations, beginning with an initial affine transformation followed by greedy symmetric diffeomorphic normalization (SyN) with cross-correlation (Avants et al., 2010, 2011). For each subject, the transformations (rigid, affine, warp) were then individually inverted and applied in inverse order to a unit warp field generated in the final template space.[3] This was then used to normalize the tracks into template space with MRtrix, by warping each point along the fibers. Finally, track density images were generated from the normalized tracks, again with $1 \times 1 \times 1$ mm³ isotropic voxels. Normalization steps were performed using Advanced Normalization Tools (ANTS, http://www.picsl.upenn.edu/ANTS/). No spatial smoothing was applied.

Motion-corrected DWIs were assessed to ensure that the correction procedure performed adequately. Inspection of the scalar images, such as FA, MD, seed masks, single-fiber response estimation masks, APM, and pre- and post-normalization TDI was also performed. Track datasets were truncated to 100,000 tracks to assess registration with the template using MRview (Tournier et al., 2012). Diffusion-weighted image and fiber track processing was performed with the MRtrix package version 0.2.12 (J-D Tournier, Brain Research Institute, Melbourne, Australia, http://www.brain.org.au/software/) (Tournier et al., 2012). The tractography and spatial normalization workflows were developed in Python with the Nipype pipeline architecture and are freely available online (Gorgolewski et al., 2011).

MT maps

For display purposes, semi-quantitative MT saturation maps were calculated within SPM8. These MT maps show the percentage loss of magnetization imposed by a single MT pulse (Draganski et al., 2011). The contrast in these MT images, which is higher than in typical T1-weighted images, enables more accurate distinction between gray and white matter, especially for the basal ganglia and substantia nigra (Helms et al., 2009). MT maps were processed using unified segmentation in order to create masks of gray matter, white matter, and cerebrospinal fluid (Ashburner and Friston, 2005). Diffeomorphic registration (DARTEL) was used to normalize the MT maps to a common template (Ashburner, 2007). Target images for the DARTEL registration were modified tissue probability maps from previous MT segmentations (Draganski et al., 2011), which included detailed segmentation of subcortical regions.

To display the final results, the study mean MT map was coregistered to the average TDI map with an initial rigid and secondary affine transformation using mutual information. Greedy symmetric diffeomorphic normalization with Mattes mutual information was used register the mean TDI map with the MNI152 1 mm T1 template. The identified transformation was applied to the mean MT image. Registration was performed in ANTs and accuracy was assessed visually at each step.

Statistical analysis

FA and MD data

Voxelwise statistical analysis of the FA data was carried out using tract-based spatial statistics (TBSS) (Smith et al., 2006), part of FSL 5.1

---

[3] Performed with the "gen_unit_warp" command in MRtrix.

(Smith et al., 2004). TBSS projects all subjects' FA data onto a mean FA tract skeleton, before applying voxelwise cross-subject statistics. TBSS was also carried out on the mean diffusivity (MD) images. Non-parametric statistics were performed using FSL's Randomise (5000 iterations), and 2D Threshold-Free Cluster Enhancement (TFCE) (Smith and Nichols, 2009) with the mean-centered total motion index as a nuisance covariate.

TDI data

An optimal white matter mask was generated from all of the track density images using the SPM8 Masking toolbox and the Luo-Nichols anti-mode method of automatic thresholding (Luo and Nichols, 2003; Ridgway et al., 2009). Permutation testing was performed using Randomise (5000 iterations) with TFCE and the mean-centered total motion index as a nuisance covariate. Only clusters with $p < 0.05$ after correcting for family-wise error rate were considered statistically significant. Tentative anatomical labels were estimated from a number of freely available brain atlases. Brainstem regions were examined by comparison with a high-resolution single subject DTI scan (Aggarwal et al., 2013). Cortical clusters were localized with the JHU ICBM-DTI-81 white-matter atlas (Oishi et al., 2010), the JHU white-matter tractography atlas (Hua et al., 2008), and the Jülich Histological Atlas (Bürgel et al., 2006).

Pearson correlation was used to explore interactions with numeric clinical metrics (e.g. UPDRS III score). The Spearman rank-order correlation coefficient was used for non-numeric variables (e.g. Hoehn and Yahr stage). Bonferroni correction was used to account for the number of independent statistical tests. Between-group differences in psychological metrics, as well as total motion index, were assessed with a two-sample t-test with an assumption of unequal variance.

Data were processed using the NITRC Computational Environment for Cluster Compute Instances using Amazon Elastic Compute Cloud (EC2) servers. The virtual machine snapshot is available upon request.

Results

Behavioral data

In our cohort the Parkinson's disease patients scored significantly lower than controls on the Mattis scale, mini-mental state examination, and the episodic memory test (Rey auditory verbal learning test), suggesting mild cognitive disturbances. Apart from these, there were no statistically significant differences between the patients and controls on any of the psychological measures. Every patient's performance was above the standard cutoff threshold for the Mattis dementia rating scale (Llebaria et al., 2008), and none of them met standard criteria for dementia associated with Parkinson's disease (Emre et al., 2007). The group mean total motion index was larger in PD patients than controls, but this did not reach statistical significance ($p = 0.053$).

Tract-based spatial statistics (TBSS) on FA and MD maps

No statistically significant results were obtained from the TBSS analysis for either FA or MD images.

Voxelwise analysis of TDI map

Statistically significant increases in track density in Parkinson's disease, relative to controls, were found in brainstem and extrapyramidal motor networks, limbic, and cognitive circuits. Areas of increased TDI were strikingly symmetric between hemispheres. Fig. 1 shows axial slices of the population mean MT image, with the clusters containing significantly increased TDI overlaid. There were no statistically significant decreases in track density in the Parkinson's patients, compared to controls. To clarify the widely distributed but significant results, we lowered the statistical threshold to 0.01 (family-wise error rate corrected). The

percent signal change in PD for clusters significant at $p_{FWE} < 0.01$ is documented in Table 2.

Brainstem and extrapyramidal motor networks

The brainstem and cerebellar peduncles showed widely increased TDI in the patients. Results projected onto the brainstem portion of the superior, middle, and inferior cerebellar peduncles, as well as the pontine crossing tract and the medial lemnisci. Brainstem nuclei also affected were the locus coeruleus, pedunculopontine nucleus, ventral tegmental area, and raphe nucleus.

Increased track density was found bilaterally in a pattern appearing to connect the substantia nigra and striatum. The significant regions encompassed the caudal ventral substantia nigra and extended dorsally toward the medial aspects of the posterior putamen. A coronal slice through the substantia nigra with the significantly ($p_{FWE} < 0.01$) affected areas overlaid is shown in Fig. 2.

Limbic circuits

TDI increases were found in the ventral tegmental area and in white matter regions surrounding the ventral striatum both medially and laterally. The pallidum, as well as the anterior and dorsomedial nuclei of the thalamus were also affected. At the cortical level, the entire cingulum was affected heavily in the right hemisphere, but only in posterior regions of the left hemisphere. Bilateral increases in TDI were also found in the orbitofrontal cortex. Fig. 3 shows slices of affected areas in the limbic system.

Cognitive circuits

Increased streamline density in Parkinson's patients was found in many areas of the cerebral white matter. Major associative pathways such as the superior and inferior longitudinal fasciculi (SLF, ILF) showed sections of increased TDI.

In the frontal cortex, the genu of the corpus callosum and areas of the anterior corona radiata were affected. The superior parietal lobule was widely affected, ostensibly by changes to the superior longitudinal fasciculi. Regions in the primary somatosensory cortices (BA2, BA3b) were notably affected. The anterior temporal poles were clearly affected by variations along the inferior longitudinal fasciculi. The occipital cortex was also affected, specifically in regions of the inferior fronto-occipital fasciculi, posterior thalamic radiations, optic radiations, and the forceps major. Fig. 4 shows affected areas involved in cognition.

Discussion

This whole brain voxel-based advanced MRI study identified brainstem and nigrostriatal pathways as significantly affected brain areas in non-demented Parkinson's disease patients as compared with controls. To the best of our knowledge, this is the first time a single MRI method has identified abnormalities projecting onto these areas. This is consistent with the known distribution of neuropathological abnormalities in early-stage Parkinson's disease (Braak et al., 2003b).

Our whole-brain voxel-based analysis also revealed significantly increased streamline density in cognitive and limbic networks. Since patients enrolled in the present study were in the first years after the diagnosis, dementia-free, and without major cognitive or behavioral deficits at the time of scanning (Table 1), it would be valuable to test if these imaging findings are predictive of further clinical deterioration.

Brainstem and extrapyramidal motor circuits

Dopaminergic denervation within the nigrostriatal pathway is the most well described neuropathological feature of Parkinson's disease, but to date, no MRI modality has been sensitive enough to clearly identify alterations to this pathway. The method used here was able to capture microstructural abnormalities within both the SN and fiber tracts to the striatum. Track density abnormalities predominated in the ventrolateral portion of the substantia nigra. This is consistent with neuropathological observations in Parkinson's disease (Fearnley and Lees, 1991), as the greatest dopaminergic cell loss occurs in nigrosome 1 of the substantia nigra *pars compacta*, which is in the caudal and ventrolateral region of the SN (Damier et al., 1999b).

Compared to controls, patients showed increased fiber density from the SN to the posterior part of the putamen, which is predominantly involved in motor circuits with the (pre)motor cortices. This finding is in agreement with post-mortem studies in Parkinson's patients that typically show profound dopamine depletion in the motor region of the striatum (Kish et al., 1988), with nigral terminals in the dorsal and caudal putamen being most affected.

We were unable to replicate findings of decreased FA at the level of the substantia nigra (Chan et al., 2007; Peran et al., 2010; Vaillancourt et al., 2009; Yoshikawa et al., 2004; Zhan et al., 2011). There are many possible factors that could explain the lack of significant changes in tensor-derived indices in our sample. First, DWI scanning parameters differ enormously between studies, with many of the previously published studies reporting data with 1.5 T scanners, using thick slices (which can include peri-nigral fiber tracts), and applying very few diffusion directions. Second, nearly all of these studies use ROIs drawn on FA or T1-weighted images, neither of which clearly delineates the substantia nigra. Third, the number of subjects is also quite low in many studies, and patient disease stage varies both within and between studies. Furthermore, our patient population is fairly early stage (mean Hoehn and Yahr stage: 1.5), and though pathological damage to the SN occurs well before symptom onset, it also continues as the disease progresses. A recent meta-analysis of the literature concluded that there is no significant disease effect on mean diffusivity (Schwarz et al., 2013), and that there is extremely large variation in the results presented on FA. They also reported that after excluding studies with unusually high values of nigral FA in the control groups, there was no disease effect on FA, either.

Increased TDI was found in caudal brainstem areas mainly in its posterior aspect. We must acknowledge that the spatial resolution of diffusion weighted MRI might be insufficient for accurate labeling of results given the anatomical complexity of the brainstem. Anatomical labeling of the involved structures is tentative, rather than definitive, and should be interpreted with caution. Significant clusters projected onto the known location of the locus coeruleus and pedunculopontine nucleus, ventral tegmental area, raphe nucleus, and pontine crossing tract.

The pedunculopontine area is heterogeneous in composition and contains cholinergic, GABAergic, and glutamatergic neurons. The PPN is heavily affected in Parkinson's disease, and the loss of roughly 50% of its cholinergic neurons (Jellinger, 1988) has been correlated with disease stage (Rinne et al., 2008). Neuropathological abnormalities in the pedunculopontine area and its connections with basal ganglia, cerebral cortex, cerebellum, and spinal cord are considered to be pivotal, not only for disturbances of gait and posture, but also for non-motor problems related to arousal and cognition (Benarroch, 2013; Stefani et al., 2013).

These results are also consistent with the reduction in medium-sized locus coeruleus neurons found in Parkinson's disease (Patt and Gerhard, 1993). In the post-mortem brain tissue of Parkinson's patients the

---

Fig. 1. Overview of the increases in track density. Group-level statistical map of increased streamline density throughout the brain. Clusters are overlaid on the group-mean magnetization transfer image. MNI coordinates in millimeters are displayed on top of each slice. Clusters shown in blue are significant at $p_{FWE} < 0.05$ and those in red are significant below $p_{FWE} < 0.01$, estimated with threshold-free cluster enhancement.
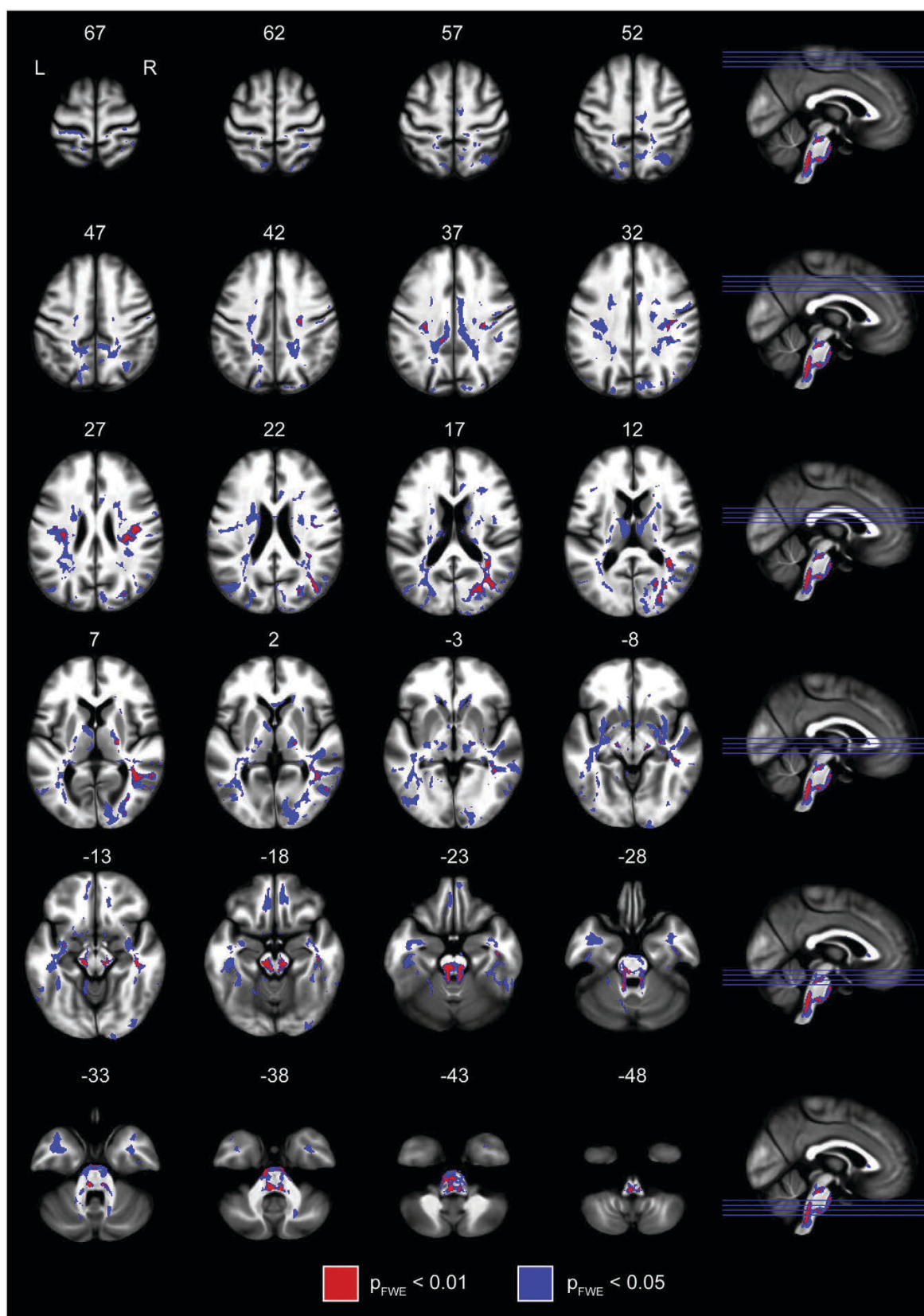
Table 2
Cluster details.

Size (mm^3)	Mean number of tracks per voxel			Location	Side	Centroid (mm)	Peak (mm)
	Controls	Parkinson's disease	Percent signal change in PD				
3062	416.5	708.6	70%	Brainstem, substantia nigra, superior cerebellar peduncle, nigrostriatal pathway	Bilateral	0, −31, −26	−2, −40, −49
1267	511.3	733.0	43%	Optic radiation	Right	32, −72, 16	39, −70, 18
1030	674.5	981.7	46%	Posterior inferior fronto-occipital fasciculus	Right	41, −48, 9	38, −45, 11
814	685.6	959.6	40%	Superior longitudinal fasciculus, parietal lobe	Right	36, −18, 31	37, −24, 29
434	324.2	517.2	60%	Middle cerebellar peduncle	Bilateral	−3, −23, −39	6, −17, −39
302	477.2	697.4	46%	Anterior inferior longitudinal fasciculus	Right	44, −23, −15	46, −14, −25
133	114.2	246.4	116%	Lateral occipital cortex	Right	55, −62, 1	59, −62, −1
109	935.9	1474.1	58%	Superior longitudinal fasciculus, parietal lobe	Left	−33, −20, 27	−32, −18, 26
97	539.6	767.6	42%	Superior longitudinal fasciculus, parietal lobe	Right	42, −36, 34	45, −37, 35
85	816.3	1218.7	49%	Superior longitudinal fasciculus, parietal lobe	Left	−29, −23, 37	−30, −21, 37
75	1112.5	1684.6	51%	Superior longitudinal fasciculus, parietal lobe	Right	35, −39, 23	36, −40, 23
38	231.9	433.8	87%	Posterior cingulum	Left	−11, −36, 37	−11, −36, 36
34	713.7	1035.9	45%	Corona radiata near somatosensory cortex	Left	−20, −44, 43	−20, −44, 44
25	370.6	544.7	47%	Anterior superior longitudinal fasciculus	Left	−41, −13, 28	−41, −12, 27
20	657.9	1044.8	59%	External capsule	Left	−32, −4, −12	−33, −4, −12
18	538.6	790.9	47%	External capsule	Right	30, −13, −9	30, −14, −9
17	982.3	1478.5	51%	Posterior optic radiation	Right	32, −56, 18	32, −55, 18
14	206.1	320.5	56%	Occipital cortex	Right	29, −79, 27	29, −78, 26
10	318.5	604.1	90%	Precuneus	Right	16, −42, 43	16, −42, 43

Information about significant ($p_{FWE} < 0.01$) clusters identified in the study. Percent signal change in Parkinson's disease within each cluster was calculated using ($TDI_{PD} − TDI_{HC})/TDI_{HC}$. Clusters were largely bilateral. The largest cluster encompassed the substantia nigra and extended upwards to the striatum, bilaterally.

average loss of noradrenergic neurons compared to controls in this region is around 70% (Bertrand et al., 1997; Zarow et al., 2003). Furthermore, connections between the locus coeruleus and the cerebellum, thalamus, and cerebral cortex are known to influence locomotion (Watson and McElligott, 1984) and arousal. Detriments in both of these systems are considered cardinal signs of Parkinson's disease (Lima, 2013).

In this study the proximal parts of middle and superior cerebellar peduncles were affected bilaterally. Previous ROI-based studies did not identify any changes in these areas in Parkinson's disease (Nicoletti et al., 2008; Paviour et al., 2007), although both relied on relatively poor quality diffusion data. The superior cerebellar peduncles contain fibers that connect the locus coeruleus and pedunculopontine nucleus with deep cerebellar nuclei and the cortex (Hazrati and Parent, 1992; Liu, 2012). Clinically relevant cerebellar involvement is uncommon in Parkinson's disease, though, and methodological issues may contribute collectively to the results identified in this region.

In the raphe nucleus, evidence for neuronal loss is less consistent. Some post-mortem studies of patients with Parkinson's disease have revealed a profound loss of 5-HT neurons (Jellinger, 1991) and their terminals (Birkmayer and Birkmayer, 1987; Kish et al., 2008), although other studies have not. This variability may contribute to the heterogeneity in mood disturbances found in Parkinson's patients.

Limbic network

Increased TDI was found bilaterally in limbic areas including the ventral tegmental area, ventral striatum, medial thalamus, orbitofrontal and anterior cingulate cortices.

The VTA loses considerable amounts of dopaminergic neurons in patients with Parkinson's disease (Uhl et al., 1985). The ventral tegmentum is populated largely by dopaminergic neurons and is tightly linked with the reward circuit of the nucleus accumbens (Sesack and Grace, 2009). It projects to the forebrain and limbic system and a loss of integrity in these pathways may influence patients' emotional state. In this study the patients showed a trend toward increased anxiety and depression, but scores on the HADS scale did not reach the threshold for the diagnosis of depression (Table 1).

Regions corresponding to the anterior and dorsomedial thalamic nuclei were found to have increased TDI in PD. The anterior, dorsomedial, and ventral anterior thalamic nuclei have previously been shown to have reduced FA in Parkinson's disease (Planetta et al., 2013). Both the anterior and dorsomedial nuclei are involved in the limbic system. The anterior nucleus projects to the cingulate gyrus, whereas the dorsomedial nucleus connects to the amygdala, anterior cingulate, and prefrontal cortices.

Cognitive circuits

The patients in this study were in early stages of the disease and showed no evidence of dementia. For this reason we did not expect to find substantial abnormalities in the cerebral cortical areas. Neuropsychological testing, however, did indicate very mild cognitive disturbances in the patients.

Clusters of significantly increased TDI in patients projected primarily onto posterior areas of the cerebral white matter. The corresponding cortical areas consistently show disturbed resting-state activity in PD populations studied using functional imaging methods such as ^{18}F-fluorodeoxyglucose PET and arterial spin labeling (Garraux et al., 2011; Hu et al., 2000; Melzer et al., 2011; Tang et al., 2010). Our study supports the hypothesis that altered activity in these areas may be related to damage within white matter pathways targeting these areas. This may contribute to the mild cognitive disturbances found in PD patients when compared with controls. Our transversal study design does not allow us to test whether or not altered white matter tracts in posterior areas are predictive of future cognitive deterioration.

Methodological considerations

Our analysis, unexpectedly, showed an increase in streamline density in the PD patients. The reason for this increase is unclear, though, so we are forced to speculate as to its cause. We have identified several potential sources of error. The first relates to the calibration and use of constrained spherical deconvolution to fit fiber orientation distribution models to the DWI data.

The key assumption behind spherical deconvolution approaches is that the measured signal in any voxel is a convolution of the fiber orientation distribution in that voxel and the diffusion-weighted signal response for a single-fiber population. The single-fiber response in this study is estimated on a subject-by-subject basis and assumed to be constant throughout the brain. The fiber response functions are approximated by a linear combination of spherical harmonic basis functions, which in this study, were truncated at the 8th order harmonic. The
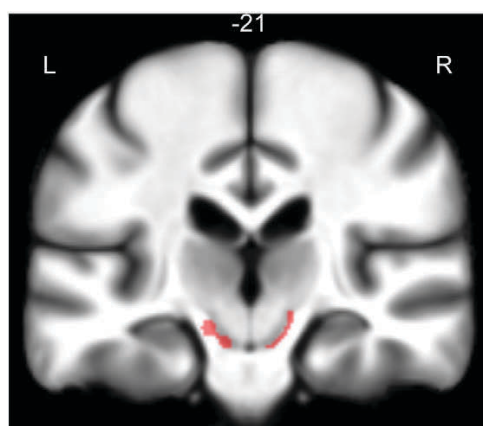
Fig. 2. Substantia nigra cluster. Single coronal slice showing the cluster that encompasses the substantia nigra ($p_{FWE} < 0.01$). The cluster is overlaid on the study mean MT map, so that the SN is more visible. This cluster extends upward through the cerebral peduncles and terminates at the posterior medial putamen.

impact of higher harmonic orders (than 8) on the spherical harmonic fit has recently been shown to be negligible for the b-value used in this study ($b = 2500$ s/mm^2) (Tournier et al., 2013). In this study, highly anisotropic (FA > 0.7) voxels were assumed to contain a fiber population oriented in a single direction, and used for fiber response calibration. These were extracted from an eroded FA image so that voxels at the edges of the brain, which are more prone to artifacts, were not considered. Future studies may consider adding a calculation of tensor mode (Ennis and Kindlmann, 2006) to help select voxels for calibration. Iterative (Tournier et al., 2013) and recursive (Tax et al., 2014) methods for CSD calibration have also recently been demonstrated. In our study the calibration values were not found to differ between groups (two sample t-test, unequal variance, data not shown).

One possible source of error is potential incongruity between the approximated fiber response function and the actual fiber response function found in chronically damaged fiber tracts. It has been demonstrated that poor estimates of fiber response function, (e.g. caused by calibrating the response function from voxels with multiple fiber populations) can lead to spurious fiber orientations being resolved (Parker et al., 2013). These artifactual fiber orientations may be especially apparent in regions with complex micro- and macro-structural properties, multiple fiber populations, or partial volume effects. We applied the standard threshold of FOD magnitude > 0.1, which substantially reduces the number of spurious peaks capable of disrupting the tractography algorithm (Parker et al., 2013).

It remains unclear how researchers should proceed when performing spherical deconvolution within pathological populations containing local changes in microstructural properties. Image-wide

fiber response calibration may not be the best solution for pathological brains. Lowering the maximum harmonic order allowed in constrained spherical harmonic deconvolution (CSD) can reduce its sensitivity to miscalibration (Parker et al., 2013). Other alternatives to CSD that may reduce spurious fiber orientations are damped Richardson–Lucy deconvolution (Dell'Acqua et al., 2010) and voxel-by-voxel response estimation (Anderson, 2005).

The second concern involves the white matter masking and tractography seeding used in this study. We estimated white matter masks from the signal variation in the DWIs, and because this technique was used, they may have differed in spatial extent between subjects. White matter masks should be segmented carefully from high-resolution structural images and subsequently co-registered to diffusion space. It may also be beneficial to seed a specific number of tracks from every white matter voxel, rather than a large number from randomly chosen masked voxels.

One notable subjective choice in this study was the resolution of the TDI and APM maps. We chose 1 mm^3 isotropic voxels based on our own testing and because track quantification studies at this resolution have been previously published (Besseling et al., 2012; Pannek et al., 2011). The primary requirement for the TDI and APM resolution is that it should provide reliable maps with small variability across subjects, so that template building and normalization are performed accurately. The choice of spatial resolution for track quantification studies is highly dependent on the amount of tracks the image is being sampled from. In our study, each subject was seeded with 5 million tracks, and we found that this led to reliable TDI maps with 1 mm^3 isotropic voxels. Smaller voxel sizes led to maps with distributed empty voxels and greatly increased the computational cost during both TDI generation and normalization. Optimal settings for track quantification need to be standardized for it to become widely adopted.

This study was performed carefully and differences between groups were assessed conservatively. Our results demonstrate that TDI is affected in Parkinson's disease in specific areas of the brain, many of which have been previously linked to known dysfunctions. If these changes were global or randomly located they would not have been identified as significant by group-wise statistical tests.

Track-weighted imaging is inherently a non-local analysis technique. That is, biological changes or artifacts that are present in one region will impact the track-weighted measures sampled in other voxels traversed by the same tracks. This quality of track density imaging also likely contributed to our widely spatially distributed results. Even if the above issues are resolved, TWI may be more appropriate (and interpretable) in pathologies where there are only a small number of affected tracts.

The clinical relevance of neuroimaging findings when patient and control groups are compared is usually appreciated by testing for a simple relationship between clinical and imaging data. Our analysis did not identify any significant linear correlation between streamline density and individual performance in motor and cognitive tests: individuals
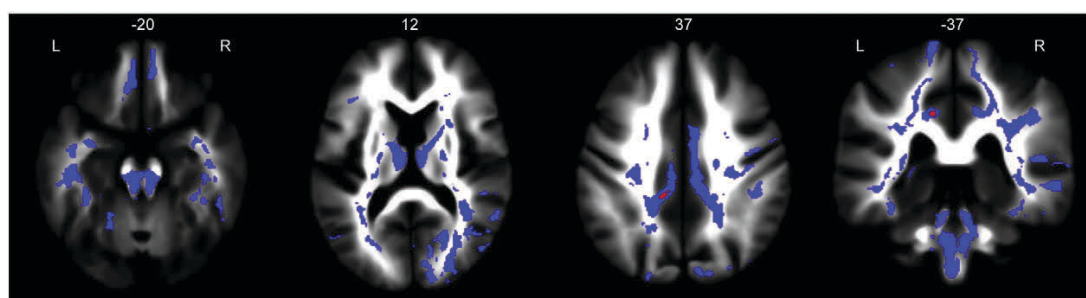

Fig. 3. Limbic system clusters. Limbic involvement was widespread, involving the cingulum, orbitofrontal cortex, anterior and dorsomedial thalamus. Clusters are overlaid on the study mean TDI map. Clusters in blue are significant below $p_{FWE} < 0.05$ and clusters in red are significant at $p_{FWE} < 0.01$.
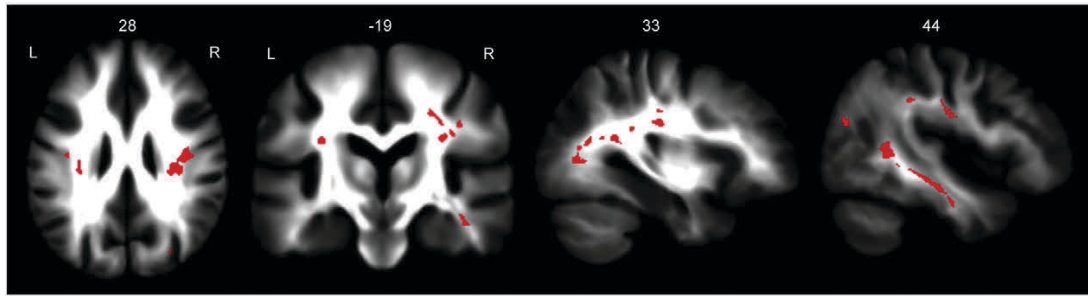
Fig. 4. Cognitive network clusters. White matter tracts involved in cognitive function were notably affected. The superior and inferior longitudinal fasciculi, superior parietal lobule, and occipital cortex showed increased track density. Clusters are overlaid on the study mean TDI map. Clusters shown are significant at $p_{FWE} < 0.01$.

with poorer performance did not show more severe imaging disturbances. This may suggest that the streamline density imaging method used in the present study is a biomarker of disease traits but may not be appropriate to monitor disease severity. Several other effects also need to be considered including compensatory mechanisms by exogenous factors, such as anti-Parkinsonian medications at the time of clinical testing, endogenous processes (i.e., neural network compensatory mechanisms), or a combination of both.

Potential future track quantification studies may want to consider using (i) outlier rejection methods like HOMOR (Pannek et al., 2012), (ii) lower maximum harmonic orders for CSD, or damped Richardson-Lucy deconvolution (Parker et al., 2013), (iii) templates created from subjects' FOD (Raffelt et al., 2011), (iv) anatomically constrained tractography (Smith et al., 2012) and filtering of tractograms given information from spherical-deconvolution (Smith et al., 2013), and (v) more reliable track-weighted imaging approaches (Besseling et al., 2012; Willats et al., 2014). Another method to consider may be direct comparison of FOD functions using apparent fiber density, which has proven successful in motor neuron disease (Raffelt et al., 2012). Global tractography approaches are also becoming feasible for widespread use (Reisert et al., 2010) and can provide more biologically plausible tractograms.

Conclusion

We have performed track density imaging within a large population of early-stage patients with Parkinson's disease and a group of matched healthy controls. Our cross-sectional analysis revealed increased streamline counts in Parkinson's disease within various white matter pathways traditionally involved in brainstem and extrapyramidal functions, limbic, and cognitive processes. The most remarkable result is the involvement of the nigrostriatal pathways extending dorsally from the ventrolateral part of the SN and terminating at the medial posterior putamen bilaterally.

Various sources of error and/or processing steps taken may have contributed to the increase in track density we observed in our patient population. At this point this confounds a biological interpretation of our results. What is clear is that track quantification can provide complementary information to standard diffusion analysis methods, and that it can be used to map both nigral and extranigral abnormalities in Parkinson's disease.

Acknowledgments

References

Aggarwal, M., Zhang, J., Pletnikova, O., Crain, B., Troncoso, J., Mori, S., 2013. Feasibility of creating a high-resolution 3D diffusion tensor imaging based atlas of the human brainstem: a case study at 11.7 T. Neuroimage 74, 117–127. http://dx.doi.org/10.1016/j.neuroimage.2013.01.061.

Anderson, A.W., 2005. Measurement of fiber orientation distributions using high angular resolution diffusion imaging. Magn. Reson. Med. 54, 1194–1206. http://dx.doi.org/10.1002/mrm.20667.

André, E.D., Grinberg, F., Farrher, E., Maximov, I.I., Shah, N.J., Meyer, C., Jaspar, M., Muto, V., Phillips, C., Balteau, E., 2014. Influence of noise correction on intra- and inter-subject variability of quantitative metrics in diffusion kurtosis imaging. PLoS One 9, e94531. http://dx.doi.org/10.1371/journal.pone.0094531.

Ashburner, J., 2007. A fast diffeomorphic image registration algorithm. Neuroimage 38, 95–113. http://dx.doi.org/10.1016/j.neuroimage.2007.07.007.

Ashburner, J., Friston, K.J., 2005. Unified segmentation. Neuroimage 26, 839–851. http://dx.doi.org/10.1016/j.neuroimage.2005.02.018.

Avants, B.B., Yushkevich, P., Pluta, J., Minkoff, D., Korczykowski, M., Detre, J., Gee, J.C., 2010. The optimal template effect in hippocampus studies of diseased populations. Neuroimage 49, 2457–2466. http://dx.doi.org/10.1016/j.neuroimage.2009.09.062.

Avants, B.B., Tustison, N.J., Song, G., Cook, P.A., Klein, A., Gee, J.C., 2011. A reproducible evaluation of ANTs similarity metric performance in brain image registration. Neuroimage 54, 2033–2044. http://dx.doi.org/10.1016/j.neuroimage.2010.09.025.

Benarroch, E.E., 2013. Pedunculopontine nucleus: functional organization and clinical implications. Neurology 80, 1148–1155. http://dx.doi.org/10.1212/WNL.0b013e3182886a76.

Benton, A.L., Sivan, A., Hamsher, K., Varney, N., 1983. Contributions to Neuropsychological Assessment: A Clinical Manual. Oxford University Press, New York.

Bertrand, E., Lechowicz, W., Szpak, G.M., Dymecki, J., 1997. Qualitative and quantitative analysis of locus coeruleus neurons in Parkinson's disease. Folia Neuropathol. 35, 80–86.

Besseling, R.M.H., Jansen, J.F.A., Overvliet, G.M., Vaessen, M.J., Braakman, H.M.H., Hofman, P.A.M., Aldenkamp, A.P., Backes, W.H., 2012. Tract specific reproducibility of tractography based morphology and diffusion metrics. PLoS One 7, e34125. http://dx.doi.org/10.1371/journal.pone.0034125.t002.

Birkmayer, J.G., Birkmayer, W., 1987. Improvement of disability and akinesia of patients with Parkinson's disease by intravenous iron substitution. Ann. Clin. Lab. Sci. 17, 32–35.

Boska, M.D., Hasan, K.M., Kibuule, D., Banerjee, R., McIntyre, E., Nelson, J.A., Hahn, T., Gendelman, H.E., Mosley, R.L., 2007. Quantitative diffusion tensor imaging detects dopaminergic neuronal degeneration in a murine model of Parkinson's disease. Neurobiol. Dis. 26, 590–596. http://dx.doi.org/10.1016/j.nbd.2007.02.010.

Braak, H., Rüb, U., Gai, W.P., Del Tredici, K., 2003a. Idiopathic Parkinson's disease: possible routes by which vulnerable neuronal types may be subject to neuroinvasion by an unknown pathogen. J. Neural Transm. 110, 517–536. http://dx.doi.org/10.1007/s00702-002-0808-2.

Braak, H., Tredici, K.D., Rüb, U., de Vos, R.A.I., Jansen Steur, E.N.H., Braak, E., 2003b. Staging of brain pathology related to sporadic Parkinson's disease. Neurobiol. Aging 24, 197–211. http://dx.doi.org/10.1016/S0197-4580(02)00065-9.

Bürgel, U., Amunts, K., Hoemke, L., Mohlberg, H., Gilsbach, J.M., Zilles, K., 2006. White matter fiber tracts of the human brain: three-dimensional mapping at microscopic resolution, topography and intersubject variability. Neuroimage 29, 1092–1105.

Calamante, F., Tournier, J.-D., Jackson, G.D., Connelly, A., 2010. Track-density imaging (TDI): super-resolution white matter imaging using whole-brain track-density mapping. Neuroimage 53, 1233–1243. http://dx.doi.org/10.1016/j.neuroimage.2010.07.024.

Calamante, F., Tournier, J.-D., Kurniawan, N.D., Yang, Z., Gyengesi, E., Galloway, G.J., Reutens, D.C., Connelly, A., 2012a. Super-resolution track-density imaging studies of mouse brain: comparison to histology. Neuroimage 59, 286–296. http://dx.doi.org/10.1016/j.neuroimage.2011.07.014.

Calamante, F., Tournier, J.-D., Smith, R.E., Connelly, A., 2012b. A generalised framework for super-resolution track-weighted imaging. Neuroimage 59, 2494–2503. http://dx.doi.org/10.1016/j.neuroimage.2011.08.099.

Chan, L.-L., Rumpel, H., Yap, K., Lee, E., Loo, H.-V., Ho, G.-L., Fook-Chong, S., Yuen, Y., Tan, E.-K., 2007. Case control study of diffusion tensor imaging in Parkinson's disease. J. Neurol. Neurosurg. Psychiatry 78, 1383–1386. http://dx.doi.org/10.1136/jnnp.2007.121525.

Cochrane, C.J., Ebmeier, K.P., 2013. Diffusion tensor imaging in parkinsonian syndromes: a systematic review and meta-analysis. Neurology 80, 857–864. http://dx.doi.org/10.1212/WNL.0b013e318284070c.

Damier, P., Hirsch, E.C., Agid, Y., Graybiel, A.M., 1999a. The substantia nigra of the human brain. I. Nigrosomes and the nigral matrix, a compartmental organization based on calbindin D(28K) immunohistochemistry. Brain 122 (Pt 8), 1421–1436.

Damier, P., Hirsch, E.C., Agid, Y., Graybiel, A.M., 1999b. The substantia nigra of the human brain. II. Patterns of loss of dopamine-containing neurons in Parkinson's disease. Brain 122 (Pt 8), 1437–1448.

Dell'Acqua, F., Scifo, P., Rizzo, G., Catani, M., Simmons, A., Scotti, G., Fazio, F., 2010. A modified damped Richardson–Lucy algorithm to reduce isotropic background effects in spherical deconvolution. Neuroimage 49, 1446–1458. http://dx.doi.org/10.1016/j.neuroimage.2009.09.033.

Draganski, B., Ashburner, J., Hutton, C., Kherif, F., Frackowiak, R.S.J., Helms, G., Weiskopf, N., 2011. Regional specificity of MRI contrast parameter changes in normal ageing revealed by voxel-based quantification (VBQ). Neuroimage 55, 1423–1434. http://dx.doi.org/10.1016/j.neuroimage.2011.01.052.

Emre, M., Aarsland, D., Brown, R., Burn, D.J., 2007. Clinical diagnostic criteria for dementia associated with Parkinson's disease. Mov. Disord. 22, 1689–1707. http://dx.doi.org/10.1002/mds.21507.

Ennis, D.B., Kindlmann, G., 2006. Orthogonal tensor invariants and the analysis of diffusion tensor magnetic resonance images. Magn. Reson. Med. 55, 136–146. http://dx.doi.org/10.1002/mrm.20741.

Fahn, S., Elton, R.L., 1987. UPDRS Development Committee. The Unified Parkinson's Disease Rating Scale. Recent Developments in Parkinsons Disease, pp. 153–163 (293–304).

Fearnley, J.M., Lees, A.J., 1991. Ageing and Parkinson's disease: substantia nigra regional selectivity. Brain 114 (Pt 5), 2283–2301.

Fearnley, J., Lees, A., 1994. Pathology of Parkinson's disease. Neurodegenerative DiseasesSaunders, Philadelphia, pp. 545–554.

Folstein, M.F., Folstein, S.E., McHugh, P.R., 1975. "Mini-mental state." A practical method for grading the cognitive state of patients for the clinician. J. Psychiatr. Res. 12, 189–198.

Garraux, G., Bahri, M.A., Lemaire, C., Degueldre, C., Salmon, E., Kaschten, B., 2011. Brain energization in response to deep brain stimulation of subthalamic nuclei in Parkinson's disease. J. Cereb. Blood Flow Metab. 31, 1612–1622. http://dx.doi.org/10.1038/jcbfm.2011.41.

Garyfallidis, E., Brett, M., Amirbekian, B., Rokem, A., Van Der Walt, S., Descoteaux, M., Nimmo-Smith, I., 2014. Dipy, a library for the analysis of diffusion MRI data. Front. Neuroinform. 8. http://dx.doi.org/10.3389/fninf.2014.00008.

Gattellaro, G., Minati, L., Grisoli, M., Mariani, C., Carella, F., Osio, M., Ciceri, E., Albanese, A., Bruzzone, M.G., 2009. White matter involvement in idiopathic parkinson disease: a diffusion tensor imaging study. Am. J. Neuroradiol. 30, 1222–1226. http://dx.doi.org/10.3174/ajnr.A1556.

Gesi, M., Soldani, P., Giorgi, F.S., Santinami, A., Bonaccorsi, I., Fornai, F., 2000. The role of the locus coeruleus in the development of Parkinson's disease. Neurosci. Biobehav. Rev. 24, 655–668. http://dx.doi.org/10.1016/S0149-7634(00)00028-2.

Gibb, W.R., 1988. Accuracy in the clinical diagnosis of parkinsonian syndromes. Postgrad. Med. J. 64, 345–351.

Gorgolewski, K., Burns, C.D., Madison, C., 2011. Nipype: a flexible, lightweight and extensible neuroimaging data processing framework in python. Front. Neuroinform. 5. http://dx.doi.org/10.3389/fninf.2011.00013.

Graham, J.M., Paley, M.N., Grünewald, R.A., Hoggard, N., Griffiths, P.D., 2000. Brain iron deposition in Parkinson's disease imaged using the PRIME magnetic resonance sequence. Brain 123 (Pt 12), 2423–2431.

Halliday, G.M., Gai, W.P., Blessing, W.W., Geffen, L.B., 1990. Substance P-containing neurons in the pontomesencephalic tegmentum of the human brain. Neuroscience 39, 81–96. http://dx.doi.org/10.1016/0306-4522(90)90223-Q.

Hazrati, L.N., Parent, A., 1992. Projection from the deep cerebellar nuclei to the pedunculopontine nucleus in the squirrel monkey. Brain Res. 585, 267–271.

Helms, G., Draganski, B., Frackowiak, R., Ashburner, J., Weiskopf, N., 2009. Improved segmentation of deep brain grey matter structures using magnetization transfer (MT) parameter maps. Neuroimage 47, 194–198. http://dx.doi.org/10.1016/j.neuroimage.2009.03.053.

Hobson, D.E., Lang, A.E., Martin, W.R.W., Razmy, A., Rivest, J., Fleming, J., 2002. Excessive daytime sleepiness and sudden-onset sleep in Parkinson disease: a survey by the Canadian Movement Disorders Group. JAMA 287, 455–463.

Hoehn, M.M., Yahr, M.D., 1967. Parkinsonism: onset, progression and mortality. Neurology 17, 427–442.

Hu, M.T.M., Taylor-Robinson, S.D., Chaudhuri, K.R., Bell, J.D., Labbe, C., Cunningham, V.J., Koepp, M.J., Hammers, A., Morris, R.G., Turjanski, N., Brooks, D.J., 2000. Cortical dysfunction in non-demented Parkinson's disease patients: a combined 31P-MRS and 18FDG-PET study. Brain 123, 340–352. http://dx.doi.org/10.1093/brain/123.2.340.

Hua, K., Zhang, J., Wakana, S., Jiang, H., Li, X., Reich, D.S., Calabresi, P.A., Pekar, J.J., van Zijl, P.C.M., Mori, S., 2008. Tract probability maps in stereotaxic spaces: analyses of white matter anatomy and tract-specific quantification. Neuroimage 39, 336–347. http://dx.doi.org/10.1016/j.neuroimage.2007.07.053.

Ibarretxe-Bilbao, N., Junque, C., Marti, M.-J., Valldeoriola, F., Vendrell, P., Bargallo, N., Zarei, M., Tolosa, E., 2010. Olfactory impairment in Parkinson's disease and white matter

abnormalities in central olfactory areas: a voxel-based diffusion tensor imaging study. Mov. Disord. 25, 1888–1894. http://dx.doi.org/10.1002/mds.23208.

Jahanshahi, M., Saleem, T., Ho, A.K., Dirnberger, G., Fuller, R., 2006. Random number generation as an index of controlled processing. Neuropsychology 20, 391–399. http://dx.doi.org/10.1037/0894-4105.20.4.391.

Jellinger, K., 1988. The pedunculopontine nucleus in Parkinson's disease, progressive supranuclear palsy and Alzheimer's disease. J. Neurol. Neurosurg. Psychiatry 51, 540–543.

Jellinger, K.A., 1991. Pathology of Parkinson's disease. Changes other than the nigrostriatal pathway. Mol. Chem. Neuropathol. 14, 153–197.

Jenkinson, C., Fitzpatrick, R., Peto, V., Greenhall, R., Hyman, N., 1997. The Parkinson's Disease Questionnaire (PDQ-39): development and validation of a Parkinson's disease summary index score. Age Ageing 26, 353–357.

Jones, D.K., Horsfield, M.A., Simmons, A., 1999. Optimal strategies for measuring diffusion in anisotropic systems by magnetic resonance imaging. Magn. Reson. Med. 42, 515–525. http://dx.doi.org/10.1002/(SICI)1522-2594(199909)42:3<515::AID-MRM14>3.0.CO;2-Q.

Jones, D.K., Knösche, T.R., Turner, R., 2013. White matter integrity, fiber count, and other fallacies: The do's and don'ts of diffusion MRI. Neuroimage 73, 239–254.

Kish, S.J., Shannak, K., Hornykiewicz, O., 1988. Uneven pattern of dopamine loss in the striatum of patients with idiopathic Parkinson's disease. Pathophysiologic and clinical implications. N. Engl. J. Med. 318, 876–880. http://dx.doi.org/10.1056/NEJM198804073181402.

Kish, S.J., Tong, J., Hornykiewicz, O., Rajput, A., Chang, L.-J., Guttman, M., Furukawa, Y., 2008. Preferential loss of serotonin markers in caudate versus putamen in Parkinson's disease. Brain 131, 120–131. http://dx.doi.org/10.1093/brain/awm239.

Leemans, A., Jones, D.K., 2009. The B-matrix must be rotated when correcting for subject motion in DTI data. Magn. Reson. Med. 61, 1336–1349. http://dx.doi.org/10.1002/mrm.21890.

Lima, M.M.S., 2013. Sleep disturbances in Parkinson's disease: the contribution of dopamine in REM sleep regulation. Sleep Med. Rev. 17, 367–375. http://dx.doi.org/10.1016/j.smrv.2012.10.006.

Liu, H.M., 2012. Biology and Pathology of Nerve Growth. Elsevier.

Llebaria, G., Pagonabarraga, J., Kulisevsky, J., García-Sánchez, C., Pascual-Sedano, B., Gironell, A., Martínez-Corral, M., 2008. Cut-off score of the Mattis Dementia Rating Scale for screening dementia in Parkinson's disease. Mov. Disord. 23, 1546–1550. http://dx.doi.org/10.1002/mds.22173.

Luo, W.-L., Nichols, T.E., 2003. Diagnosis and exploration of massively univariate neuroimaging models. Neuroimage 19, 1014–1032. http://dx.doi.org/10.1016/S1053-8119(03)00149-6.

Maggioni, M., Katkovnik, V., Egiazarian, K., Foi, A., 2013. Nonlocal transform-domain filter for volumetric data denoising and reconstruction. IEEE Trans. Image Process. 22, 119–133. http://dx.doi.org/10.1109/TIP.2012.2210725.

Mattis, S., 1988. Dementia Rating Scale Professional ManualOdessa, Odessa, FL.

Melzer, T.R., Watts, R., MacAskill, M.R., Pearson, J.F., Rüeger, S., Pitcher, T.L., Livingston, L., Graham, C., Keenan, R., Shankaranarayanan, A., Alsop, D.C., Dalrymple-Alford, J.C., Anderson, T.J., 2011. Arterial spin labelling reveals an abnormal cerebral perfusion pattern in Parkinson's disease. Brain 134, 845–855. http://dx.doi.org/10.1093/brain/awq377.

Nicoletti, G., Tonon, C., Lodi, R., Condino, F., Manners, D., Malucelli, E., Morelli, M., Novellino, F., Paglionico, S., Lanza, P., Messina, D., Barone, P., Morgante, L., Zappia, M., Barbiroli, B., Quattrone, A., 2008. Apparent diffusion coefficient of the superior cerebellar peduncle differentiates progressive supranuclear palsy from Parkinson's disease. Mov. Disord. 23, 2370–2376. http://dx.doi.org/10.1002/mds.22279.

Oishi, K., Faria, A.V., van Zijl, P.C.M., Mori, S., 2010. MRI Atlas of Human White Matter, 2nd edition. Academic Press.

Pannek, K., Mathias, J.L., Bigler, E.D., Brown, G., Taylor, J.D., Rose, S.E., 2011. The average pathlength map: a diffusion MRI tractography-derived index for studying brain pathology. Neuroimage 55, 133–141. http://dx.doi.org/10.1016/j.neuroimage.2010.12.010.

Pannek, K., Raffelt, D., Bell, C., Mathias, J.L., Rose, S.E., 2012. HOMOR: higher order model outlier rejection for high b-value MR diffusion data. Neuroimage 63, 835–842. http://dx.doi.org/10.1016/j.neuroimage.2012.07.022.

Parker, G.D., Marshall, D., Rosin, P.L., Drage, N., Richmond, S., Jones, D.K., 2013. A pitfall in the reconstruction of fibre ODFs using spherical deconvolution of diffusion MRI data. Neuroimage 65, 433–448. http://dx.doi.org/10.1016/j.neuroimage.2012.10.022.

Patt, S., Gerhard, L., 1993. A Golgi study of human locus coeruleus in normal brains and in Parkinson's disease. Neuropathol. Appl. Neurobiol. 19, 519–523.

Pavese, N., Simpson, B.S., Metta, V., Ramlackhansingh, A., Chaudhuri, K.R., Brooks, D.J., 2012. [18F]FDOPA uptake in the raphe nuclei complex reflects serotonin transporter availability. A combined [18F]FDOPA and [11C]DASB PET study in Parkinson's disease. Neuroimage 59, 1080–1084. http://dx.doi.org/10.1016/j.neuroimage.2011.09.034.

Paviour, D.C., Thornton, J.S., Lees, A.J., Jäger, H.R., 2007. Diffusion-weighted magnetic resonance imaging differentiates Parkinsonian variant of multiple-system atrophy from progressive supranuclear palsy. Mov. Disord. 22, 68–74. http://dx.doi.org/10.1002/mds.21204.

Peran, P., Cherubini, A., Assogna, F., Piras, F., Quattrocchi, C., Peppe, A., Celsis, P., Rascol, O., Demonet, J.F., Stefani, A., Pierantozzi, M., Pontieri, F.E., Caltagirone, C., Spalletta, G., Sabatini, U., 2010. Magnetic resonance imaging markers of Parkinson's disease nigrostriatal signature. Brain 133, 3423–3433. http://dx.doi.org/10.1093/brain/awq212.

Planetta, P.J., Schulze, E.T., Geary, E.K., Corcos, D.M., Goldman, J.G., Little, D.M., Vaillancourt, D.E., 2013. Thalamic projection fiber integrity in de novo Parkinson disease. Am. J. Neuroradiol. 34, 74–79. http://dx.doi.org/10.3174/ajnr.A3178.

Raffelt, D., Tournier, J.D., Fripp, J., Crozier, S., Connelly, A., Salvado, O., 2011. Symmetric diffeomorphic registration of fibre orientation distributions. Neuroimage 56, 1171–1180. http://dx.doi.org/10.1016/j.neuroimage.2011.02.014.

Raffelt, D., Tournier, J.D., Rose, S., Ridgway, G.R., Henderson, R., Crozier, S., Salvado, O., Connelly, A., 2012. Apparent fibre density: a novel measure for the analysis of diffusion-weighted magnetic resonance images. Neuroimage 59, 3976–3994. http://dx.doi.org/10.1016/j.neuroimage.2011.10.045.

Reese, T.G., Heid, O., Weisskoff, R.M., Wedeen, V.J., 2002. Reduction of eddy-current-induced distortion in diffusion MRI using a twice-refocused spin echo. Magn. Reson. Med. 49, 177–182. http://dx.doi.org/10.1002/mrm.10308.

Reisert, M., Mader, I., Anastasopoulos, C., Weigel, M., Schnell, S., Kiselev, V., 2010. Global fiber reconstruction becomes practical. Neuroimage 54, 955–962. http://dx.doi.org/10.1016/j.neuroimage.2010.09.016.

Rey, A., 1958. L'examen clinique en psychologie. Presses Universitaries De France, Paris, France.

Ridgway, G.R., Omar, R., Ourselin, S., Hill, D.L.G., Warren, J.D., Fox, N.C., 2009. Issues with threshold masking in voxel-based morphometry of atrophied brains. Neuroimage 44, 99–111. http://dx.doi.org/10.1016/j.neuroimage.2008.08.045.

Rinne, J.O., Ma, S.Y., Lee, M.S., Collan, Y., Röyttä, M., 2008. Loss of cholinergic neurons in the pedunculopontine nucleus in Parkinson's disease is related to disability of the patients. Parkinsonism Relat. Disord. 14, 553–557. http://dx.doi.org/10.1016/j.parkreldis.2008.01.006.

Schwarz, S.T., Abaei, M., Gontu, V., Morgan, P.S., Bajaj, N., Auer, D.P., 2013. Diffusion tensor imaging of nigral degeneration in Parkinson's disease: a region-of-interest and voxel-based study at 3 T and systematic review with meta-analysis. YNICL 3, 481–488. http://dx.doi.org/10.1016/j.nicl.2013.10.006.

Sesack, S.R., Grace, A.A., 2009. Cortico-basal ganglia reward network: microcircuitry. Neuropsychopharmacology 35, 27–47. http://dx.doi.org/10.1038/npp.2009.93.

Smith, S.M., Nichols, T.E., 2009. Threshold-free cluster enhancement: addressing problems of smoothing, threshold dependence and localisation in cluster inference. Neuroimage 44, 83–98. http://dx.doi.org/10.1016/j.neuroimage.2008.03.061.

Smith, S.M., Jenkinson, M., Woolrich, M.W., Beckmann, C.F., Behrens, T.E.J., Johansen-Berg, H., Bannister, P.R., De Luca, M., Drobnjak, I., Flitney, D.E., Niazy, R.K., Saunders, J., Vickers, J., Zhang, Y., De Stefano, N., Brady, J.M., Matthews, P.M., 2004. Advances in functional and structural MR image analysis and implementation as FSL. Neuroimage 23 (Suppl. 1), S208–S219. http://dx.doi.org/10.1016/j.neuroimage.2004.07.051.

Smith, S.M., Jenkinson, M., Johansen-Berg, H., Rueckert, D., Nichols, T.E., Mackay, C.E., Watkins, K.E., Ciccarelli, O., Cader, M.Z., Matthews, P.M., Behrens, T.E.J., 2006. Tract-based spatial statistics: voxelwise analysis of multi-subject diffusion data. Neuroimage 31, 1487–1505. http://dx.doi.org/10.1016/j.neuroimage.2006.02.024.

Smith, R.E., Tournier, J.-D., Calamante, F., Connelly, A., 2012. Anatomically-constrained tractography: improved diffusion MRI streamlines tractography through effective use of anatomical information. Neuroimage 62, 1924–1938. http://dx.doi.org/10.1016/j.neuroimage.2012.06.005.

Smith, R.E., Tournier, J.-D., Calamante, F., Connelly, A., 2013. SIFT: spherical-deconvolution informed filtering of tractograms. Neuroimage 67, 298–312. http://dx.doi.org/10.1016/j.neuroimage.2012.11.049.

Soria, G., Aguilar, E., Tudela, R., Mullol, J., Planas, A.M., Marin, C., 2011. In vivo magnetic resonance imaging characterization of bilateral structural changes in experimental Parkinson's disease: a T2 relaxometry study combined with longitudinal diffusion tensor imaging and manganese-enhanced magnetic resonance imaging in the 6-hydroxydopamine rat model. Eur. J. Neurosci. 33, 1551–1560. http://dx.doi.org/10.1111/j.1460-9568.2011.07639.x.

Stefani, A., Peppe, A., Galati, S., Bassi, M.S., D'Angelo, V., Pierantozzi, M., 2013. The serendipity case of the pedunculopontine nucleus low-frequency brain stimulation: chasing a gait response, finding sleep, and cognition improvement. Front. Neurol. 4. http://dx.doi.org/10.3389/fneur.2013.00068.

Tang, C.C., Poston, K.L., Dhawan, V., Eidelberg, D., 2010. Abnormalities in metabolic network activity precede the onset of motor symptoms in Parkinson's disease. J. Neurosci. 30, 1049–1056. http://dx.doi.org/10.1523/JNEUROSCI.4188-09.2010.

Tax, C.M.W., Jeurissen, B., Vos, S.B., Viergever, M.A., Leemans, A., 2014. Recursive calibration of the fiber response function for spherical deconvolution of diffusion MRI data. Neuroimage 86, 67–80. http://dx.doi.org/10.1016/j.neuroimage.2013.07.067.

Tournier, J.D., Calamante, F., Gadian, D.G., Connelly, A., 2004. Direct estimation of the fiber orientation density function from diffusion-weighted MRI data using spherical deconvolution. Neuroimage 23, 1176–1185. http://dx.doi.org/10.1016/j.neuroimage.2004.07.037.

Tournier, J.D., Yeh, C.-H., Calamante, F., Cho, K.-H., Connelly, A., Lin, C.-P., 2008. Resolving crossing fibres using constrained spherical deconvolution: validation using diffusion-weighted imaging phantom data. Neuroimage 42, 617–625. http://dx.doi.org/10.1016/j.neuroimage.2008.05.002.

Tournier, J.-D., Mori, S., Leemans, A., 2011. Diffusion tensor imaging and beyond. Magn. Reson. Med. 65, 1532–1556. http://dx.doi.org/10.1002/mrm.22924.

Tournier, J.D., Calamante, F., Connelly, A., 2012. MRtrix: diffusion tractography in crossing fiber regions. Int. J. Imaging Syst. Technol. 22, 53–66. http://dx.doi.org/10.1002/ima.22005.

Tournier, J.D., Calamante, F., Connelly, A., 2013. Determination of the appropriate b value and number of gradient directions for high-angular-resolution diffusion-weighted imaging. NMR Biomed. 26, 1775–1786. http://dx.doi.org/10.1002/nbm.3017.

Uhl, G.R., Hedreen, J.C., Price, D.L., 1985. Parkinson's disease: loss of neurons from the ventral tegmental area contralateral to therapeutic surgical lesions. Neurology 35, 1215–1218.

Vaillancourt, D.E., Spraker, M.B., Prodoehl, J., Abraham, I., Corcos, D.M., Zhou, X.J., Comella, C.L., Little, D.M., 2009. High-resolution diffusion tensor imaging in the substantia nigra of de novo Parkinson disease. Neurology 72, 1378–1384. http://dx.doi.org/10.1212/01.wnl.0000340982.01727.6e.

Volz, S., Nöth, U., Rotarska-Jagiela, A., Deichmann, R., 2010. A fast B1-mapping method for the correction and normalization of magnetization transfer ratio maps at 3 T. Neuroimage 49, 3015–3026. http://dx.doi.org/10.1016/j.neuroimage.2009.11.054.

Watson, M., McElligott, J.G., 1984. Cerebellar norepinephrine depletion and impaired acquisition of specific locomotor tasks in rats. Brain Res. 296, 129–138.

Weiskopf, N., Helms, G., 2008. Multi-parameter mapping of the human brain at 1 mm resolution in less than 20 minutes. Presented at the Proc Intl SocMagn Res Med., Toronto.

Willats, L., Raffelt, D., Smith, R.E., Tournier, J.D., Connelly, A., Calamante, F., 2014. Quantification of track-weighted imaging (TWI): characterisation of within-subject reproducibility and between-subject variability. Neuroimage 87, 18–31. http://dx.doi.org/10.1016/j.neuroimage.2013.11.016.

Yarnykh, V.L., 2007. Actual flip-angle imaging in the pulsed steady state: a method for rapid three-dimensional mapping of the transmitted radiofrequency field. Magn. Reson. Med. 57, 192–200. http://dx.doi.org/10.1002/mrm.21120.

Yendiki, A., Koldewyn, K., Kakunoori, S., Kanwisher, N., Fischl, B., 2014. Spurious group differences due to head motion in a diffusion MRI study. Neuroimage 88, 79–90. http://dx.doi.org/10.1016/j.neuroimage.2013.11.027.

Yoshikawa, K., Nakata, Y., Yamada, K., Nakagawa, M., 2004. Early pathological changes in the parkinsonian brain demonstrated by diffusion tensor MRI. J. Neurol. Neurosurg. Psychiatry 75, 481–484.

Zarow, C., Lyness, S.A., Mortimer, J.A., Chui, H.C., 2003. Neuronal loss is greater in the locus coeruleus than nucleus basalis and substantia nigra in Alzheimer and Parkinson diseases. Arch. Neurol. 60, 337–341. http://dx.doi.org/10.1001/archneur.60.3.337.

Zhan, W., Kang, G.A., Glass, G.A., Zhang, Y., Shirley, C., Millin, R., Possin, K.L., Nezamzadeh, M., Weiner, M.W., Marks Jr., W.J., Schuff, N., 2011. Regional alterations of brain microstructure in Parkinson's disease using diffusion tensor imaging. Mov. Disord. 27, 90–97. http://dx.doi.org/10.1002/mds.23917.

Zigmond, A.S., Snaith, R.P., 1983. The Hospital Anxiety and Depression Scale. Acta Psychiatr. Scand. 67, 361–370. http://dx.doi.org/10.1111/j.1600-0447.1983.tb09716.x.

Zweig, R.M., Cardillo, J.E., Cohen, M., Giere, S., Hedreen, J.C., 1993. The locus ceruleus and dementia in Parkinson's disease. Neurology 43, 986–991.

Paper III

A finite-element reciprocity solution for EEG forward modeling with accurate individual head models

Ziegler, E., Chellappa, S. L., Gaggioni, G., Ly, J. Q. M., Vandewalle, G., André, E., Geuzaine, C.*, Phillips, C.*

* Contributed equally
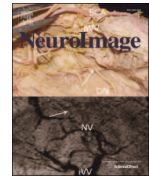
Technical Note

A finite-element reciprocity solution for EEG forward modeling with realistic individual head models

Erik Ziegler [a], Sarah L. Chellappa [a], Giulia Gaggioni [a], Julien Q.M. Ly [a], Gilles Vandewalle [a], Elodie André [a], Christophe Geuzaine [b,1], Christophe Phillips [a,b,1,*]

[a] *Cyclotron Research Centre, University of Liège, Liège, Belgium*
[b] *Department of Electrical Engineering and Computer Science, University of Liège, Liège, Belgium*

ARTICLE INFO

ABSTRACT

We present a finite element modeling (FEM) implementation for solving the forward problem in electroencephalography (EEG). The solution is based on Helmholtz's principle of reciprocity which allows for dramatically reduced computational time when constructing the leadfield matrix. The approach was validated using a 4-shell spherical model and shown to perform comparably with two current state-of-the-art alternatives (OpenMEEG for boundary element modeling and SimBio for finite element modeling).

We applied the method to real human brain MRI data and created a model with five tissue types: white matter, gray matter, cerebrospinal fluid, skull, and scalp. By calculating conductivity tensors from diffusion-weighted MR images, we also demonstrate one of the main benefits of FEM: the ability to include anisotropic conductivities within the head model. Root-mean square deviation between the standard leadfield and the leadfield including white-matter anisotropy showed that ignoring the directional conductivity of white matter fiber tracts leads to orientation-specific errors in the forward model.

Realistic head models are necessary for precise source localization in individuals. Our approach is fast, accurate, open-source and freely available online.

© 2014 Published by Elsevier Inc.

Introduction

Identifying the sources of neuronal activity is a key step in many studies using electroencephalography (EEG) or magnetoencephalography (MEG). The problem itself is ill-posed as there can be an infinite number of solutions describing the origin of the neural activity that has been recorded (Helmholtz, 1853). There are two problems to solve if one wants to identify the location of neuronal activity from a set of electrode recordings. The first is known as the forward problem, and its basis is building an electromagnetic model of the subject's head. Once this is created, one can attempt to identify neural sources by solving the inverse problem. The inverse problem is essentially an optimization problem, where the procedure is to work backwards from the scalp recordings in order to identify one or more current dipoles which best explain the acquired data. In this paper we focus on the forward problem, which has not been given a great deal of attention in neuroimaging. Despite many published studies demonstrating high-quality head models and forward modeling approaches (Güllmar et al., 2010; Hallez et al., 2005; Rullmann et al., 2009; Shirvany et al., 2013; Vanrumste et al., 2001; Vorwerk et al., 2014; Wolters et al., 2006), most functional neuroimaging studies still rely on relatively poor quality electromagnetic head models when performing source localization.

There are generally three types of head modeling methods. The first and easiest is the simplification of the head to a spherical model. The second, and most common, is boundary element modeling (BEM), in which distinct shells of the head are meshed as two-dimensional surfaces and the volume in between them is treated as distinct tissue types (e.g. BEM meshes may represent the inner and outer borders of the skull). The third is finite element modeling (FEM), which operates similarly to boundary element modeling with the exception that meshes are constructed in three dimensions (e.g. using tetrahedra).

Researchers have learned to avoid oversimplified spherical head models, and most now use boundary element solutions built-in to packages like SPM (Litvak et al., 2011), NFT (Acar and Makeig, 2010), MNE (Gramfort et al., 2013, 2014), and OpenMEEG (Gramfort et al., 2010). Boundary element models are known to perform quickly and with high accuracy, though they suffer some drawbacks due to their

geometric limitations. Simply put, these methods fail in situations with complex geometries. Their largest fault is that they assume isotropic conductivity within all regions of each tissue type, an assumption that is well known to be incorrect (Gramfort et al., 2010). Although efforts have been made to include anisotropic conductivity into BEM methods (Olivi et al., 2011), it is technically very challenging.

Approaches for solving the forward problem aim to create what is known as a leadfield matrix. The leadfield matrix allows for the computation of the potential distribution on the sensors from a current source (e.g. synchronously firing neurons) placed inside the brain. The relationship between the leadfield matrix (L) and the remainder of the system can be written as:

$$\Phi = L \cdot j + n \tag{1}$$

where Φ is the recorded sensor potential, j is the neural source represented as a current dipole, and n represents the noise in the system. An analytical solution has been derived for obtaining the potential distribution on the surface of an ellipsoid given an arbitrarily located current dipole (Kariotou, 2004; Munck and Peters, 1993; Sarvas, 1987). The analytical approach is used as the ground truth when testing new methods.

The most common approach to computing the leadfield, known as the direct method, is to place several thousand current dipoles in the brain within the cortical ribbon, oriented tangentially to the white matter surface. For each dipole, the scalp potential is obtained by solving the forward problem. The leadfield matrix is then created from the chosen dipole positions and the calculated sensor potentials. Realistic finite element (FE) models of the human head require hundreds of thousands of elements to provide accurate solutions. Due to the high mesh complexity, the typical direct method for computing the leadfield matrix becomes unreasonably slow for finite element models. To overcome this, alternative methods for calculating the leadfield matrix, such as the adjoint (Vallaghé et al., 2009), subtraction (Schimpf et al., 2002; Wolters et al., 2007), and reciprocity (Rush and Driscoll, 1969; Weinstein et al., 2000) approaches have been devised. The approach taken here was derived from Helmholtz's principle of reciprocity and first applied to EEG by Rush and Driscoll (Helmholtz, 1853; Rush and Driscoll, 1969). Reciprocity explains that the roles of the dipole and sensor can be reversed, compared to the direct method. A full leadfield matrix can be created by applying current between each sensor and a ground electrode, and storing the electric field induced in each element of the head model. In this framework only $M - 1$ iterations of the forward problem are necessary to create a leadfield matrix, where M is the number of sensors. The direct method, in contrast, requires thousands of iterations to create a leadfield from a dense array of sources. A number of previous studies have demonstrated the use of reciprocity for FEM solutions (Hallez et al., 2005; Shirvany et al., 2013; Vanrumste et al., 2001; Weinstein et al., 2000). This article draws heavily on the work of Weinstein et al. for its basis (Weinstein et al., 2000).

It is well known that white matter fiber structures in the human brain are highly directional (i.e. anisotropic) in both their structure and properties. Diffusion-weighted imaging (DWI) allows for the quantification and modeling of water movement within tissues and can be used to compute the anisotropy profile of brain structures (e.g. by fitting a tensor at each voxel) (Le Bihan and Johansen-Berg, 2012). It has also been established that through a remapping of the tensor's eigenvalues, electrical conductivity can be approximated from the water diffusion tensor (Tuch et al., 2001). This allows finite element models to include local information about the conductivity of the tissues which boundary element methods are incapable of integrating.

To our knowledge there is currently only one freely available solution for realistic FEM forward modeling — NeuroFEM, part of SimBio (Fingberg et al., 2003). The developers of NeuroFEM have created a number of forward solvers and efforts are underway to bring an easily accessible wrapper to MATLAB through integration with Fieldtrip (Oostenveld et al., 2011). The installation and use of NeuroFEM remain complex, though, as it must be compiled directly by the user, and this is often non-trivial on modern operating systems. SimBio also relies on many outdated file formats which makes interoperability difficult. There is also no standard or reproducible meshing procedure available in SimBio; in recent publications skin and skull meshing has been performed, at least in part, using commercial software (Vorwerk et al., 2014; Wagner et al., 2014).

We therefore aimed to create an alternative toolbox for accurate and fast subject-specific finite element modeling in EEG studies. The approach was evaluated using a four-shell spherical model and real data from a human subject. We have developed our software in the open under a free software license and welcome contributions from the community (see Technical details).

Methods

We have split the Methods section into three parts. The first describes our implementation and approach to calculating the leadfield matrix. The second section describes our evaluation of the approach against the analytical solution using a four-shell spherical model. The third section details our tests with real-world MRI and DWI data.

Finite element reciprocity solution

In neuroscience patches of active cortex are often approximated as dipolar current sources with extremely small distances between their poles. These equivalent current dipoles have three-dimensional orientations and units of current times length ($A \cdot m$). The reciprocity principle explains that in order to identify the voltage (ϕ) difference between any two points resulting from a single current dipole (j), it is sufficient to know the electric field (E) at the dipole location produced by injecting a known current (I) through two points (A, B).

$$\phi_A - \phi_B = \frac{E \cdot j}{I}. \tag{2}$$

This allows us to switch the role of the dipoles and sensors compared to the typical direct method. We place surface leads on the scalp and calculate the electric field in each element of the gray matter. Given a dipole location and orientation, using Eq. (2) will provide us with each sensor potential, relative to a ground electrode.

The forward problem is redefined for each source electrode and the FEM calculations are performed using GetDP with the Galerkin approach. In-depth mathematical details can be found in the Supplementary material. The current density, electric field, and potential are calculated at each element. The process of creating and comparing the leadfield matrix, in practice, is as follows:

1. An arbitrary ground electrode is chosen by the user.
2. A unit current source is defined at one of the (non-ground) sensor locations.
3. The induced electric field in each element of the 3D mesh is calculated with GetDP.
4. Steps 2 and 3 are repeated for all non-ground sensors. The electric field vector for each element is stored and these rows are later stacked to create the leadfield matrix defined in Eq. (3).
5. To calculate the potential on the sensors from a dipole at any given location, one must first identify the mesh element (N) closest to the dipole location. The potential at each sensor caused by a dipole in that element is the dot product of the dipole orientation vector (j^N) and the leadfield vector (L^N) for the element (see Eq. (1)).

Once the leadfield is pre-computed, it is trivial to calculate the sensor potential produced by a dipole in any element.

$$
\begin{bmatrix}
L_1^{1,x} & L_1^{1,y} & L_1^{1,z} & \cdots & L_1^{N,x} & L_1^{N,y} & L_1^{N,z} \\
L_2^{1,x} & L_2^{1,y} & L_2^{1,z} & \cdots & L_2^{N,x} & L_2^{N,y} & L_2^{N,z} \\
\vdots & \vdots & \vdots & \vdots & \vdots & \vdots & \vdots \\
L_M^{1,x} & L_M^{1,y} & L_M^{1,z} & \cdots & L_M^{N,x} & L_M^{N,y} & L_M^{N,z}
\end{bmatrix}
\cdot
\begin{bmatrix}
j^{1,x} \\ j^{1,y} \\ j^{1,z} \\ \vdots \\ j^{N,x} \\ j^{N,y} \\ j^{N,z}
\end{bmatrix}
=
\begin{bmatrix}
\Phi_1 \\ \Phi_2 \\ \vdots \\ \Phi_M
\end{bmatrix}
\tag{3}
$$

The benefits of reciprocity are clear, as the forward problem need only be solved $M - 1$ times, where M is the number of EEG electrodes. In comparison, the standard direct method requires a dense array (usually thousands) of dipole sources (and independent calculations) throughout the gray matter.

Validation in a spherical model

In this section we compare our implementation with two other freely available solvers, OpenMEEG and SimBio. We calculate two parameters: the relative difference and relative magnitude. These parameters are used to describe the error between the numerically calculated solution and the analytically derived solution. The relative difference measure (RDM) is defined as:

$$
\text{RDM}\left(\widetilde{\Phi}, \Phi_a\right) = \left\| \frac{\widetilde{\Phi}}{\left\|\widetilde{\Phi}\right\|} - \frac{\Phi_a}{\left\|\Phi_a\right\|} \right\|
\tag{4}
$$

where $\widetilde{\Phi}$ represents the potential on the electrodes computed numerically, and Φ_a is the analytically calculated potential. The relative magnitude (MAG) between these values is calculated using Eq. (5):

$$
\text{MAG}\left(\widetilde{\Phi}, \Phi_a\right) = \frac{\left\|\widetilde{\Phi}\right\|}{\left\|\Phi_a\right\|}.
\tag{5}
$$

In these equations the norm ($\|\Phi\|$) indicates the Euclidean (ℓ^2) norm over the recorded electrode measurements. Relative difference in magnitude (RDM) is better the closer it is to zero, whereas relative magnitude (MAG) should as close as possible to 1.

Four spherical 2D meshes were created in Gmsh and volumetric meshes were created between them. Volumes between the shells were considered to represent, from inside outward, (i) brain, (ii) cerebrospinal fluid, (iii) skull, and (iv) skin. The characteristic length of the triangular and tetrahedral elements was 3 mm in the brain and 7 mm in the cerebrospinal fluid, skull, and skin. In total the mesh contained 52,510 nodes and 336,000 elements. The same volumetric mesh was used for simulations performed in SimBio.

Electrode locations were selected by creating a unit icosahedron, scaling the vertex locations by the radius of the sphere (100 mm), and selecting the closest tetrahedra of the spherical mesh. The number of electrodes depends on the number of vertices in the icosahedron, which in this case was 42. The spherical model is shown in Fig. 1 and the conductivity values used can be found in Table 1. A matching spherical boundary element model was created in OpenMEEG (Gramfort et al., 2010) and the leadfield was calculated. The boundary element model had 42 nodes and 80 triangles per spherical shell, for a total of 168 nodes and 320 elements. To enable comparison with the analytical solution, the leadfields from OpenMEEG and SimBio were re-referenced by subtracting the value at the user-selected ground electrode from all other electrode potentials. Probe dipoles were placed at distances 4 mm apart from the center of the sphere up to the boundary between brain and CSF, oriented outwards, for a total of 22 probe positions. The RDM and MAG were calculated for OpenMEEG, SimBio, and our implementation.

Application to real data

Participants

Written informed consent was obtained from our subject in accordance with the Declaration of Helsinki. The Ethics Committee of the University of Liège approved the study. Data used in the Supplementary material was acquired at the University of Tübingen and is freely available online (Windhoff et al., 2013).

Images were acquired on a 3 T head-only MR scanner (Magnetom Allegra, Siemens Medical Solutions, Erlangen, Germany) operated with an 8-channel head coil. Diffusion-weighted (DW) images were acquired with a twice-refocused spin-echo sequence with EPI readout at two distinct b-values (b = 1000, b = 2500 s/mm^2) along 120 encoding gradients that were uniformly distributed in space by an electrostatic repulsion approach (Jones et al., 1999). This sequence is designed specifically to reduce the distortions induced by eddy currents in the diffusion-weighted images (Reese et al., 2003). For the purposes of motion correction, 22 unweighted (b = 0) volumes, interleaved with the DW images, were acquired. Volumes were acquired with a repetition time (TR) of 6800 ms, an echo time (TE) of 91 ms, and a field-of-view (FOV) of 211 mm^2. Maximum slew rate was 400 mT/(m/ms) and maximum gradient amplitude was 40 mT/m. No parallel imaging techniques were used. The multi-channel head coil was used to increase the signal-to-noise ratio, and not the speed of the acquisition. Volumes were acquired with a 6/8 partial Fourier factor. Voxels were isotropic with dimensions of $2.4 \times 2.4 \times 2.4$ mm^3 and volumes were acquired in 54 transverse slices using an 88×88 voxel matrix. A high-resolution T1-weighted image was also acquired for each subject (3D modified driven equilibrium Fourier transform, repetition time = 7.92 ms, echo time = 2.4 ms, inversion time = 910 ms, flip angle = 15°, field of view = $256 \times 224 \times 176$ mm^3, 1 mm isotropic spatial resolution).

Interleaved unweighted images from the diffusion sequence were realigned to the first unweighted volume with a rigid body transformation using SPM8 (Wellcome Trust Centre for Neuroimaging, UCL, UK). Registration was performed (rigid, mutual information) between the first unweighted volume and each of the interleaved unweighted volumes (e.g. register $b0_3$ to $b0_1$). The translation and rotation values between $b0_1$ and $b0_{22}$ were linearly interpolated and applied to the weighted volumes. This put all the weighted images in alignment with the first b0 volume without the contrast problems of co-registering weighted and unweighted images. Diffusion gradient vectors were rotated accordingly (Leemans and Jones, 2009). For each diffusion-weighted volume, a non-local mean filter was applied (Maggioni et al., 2013) and noise was corrected using power image correction adapted for multi-coil acquisitions (André et al., 2014). No further corrections were applied to correct for eddy current-induced distortions in the diffusion-weighted volumes because the diffusion sequence did a sufficient job of suppressing them. Diffusion analysis in this study was performed exclusively on the volumes acquired at b = 1000 s/mm^2.

T1-weighted structural meshing

The structural meshing pipeline is an evolution of the "mri2mesh" Unix shell script provided in the Simulation of Non-invasive Brain Stimulation (SimNIBS, http://simnibs.org/) package (Windhoff et al., 2013). The workflow begins with automated whole-brain segmentation of Freesurfer (Desikan et al., 2006). It relies on MeshFix (Attene, 2010) for repairing, dilating, merging, smoothing, remeshing, and otherwise modifying surface meshes of the various sections of the brain. Broadly, the segmented regions of the gray matter, white matter, cerebrospinal fluid, skull, and skin are meshed in two dimensions and refined so that there are no intersections between the meshes of each tissue type. These 2D meshes are then processed using Gmsh (Geuzaine and Remacle, 2009) and used to create distinct 3D volume meshes for each tissue compartment. The FEM node closest to each of the EEG electrodes was obtained by computing the Euclidean distance between the
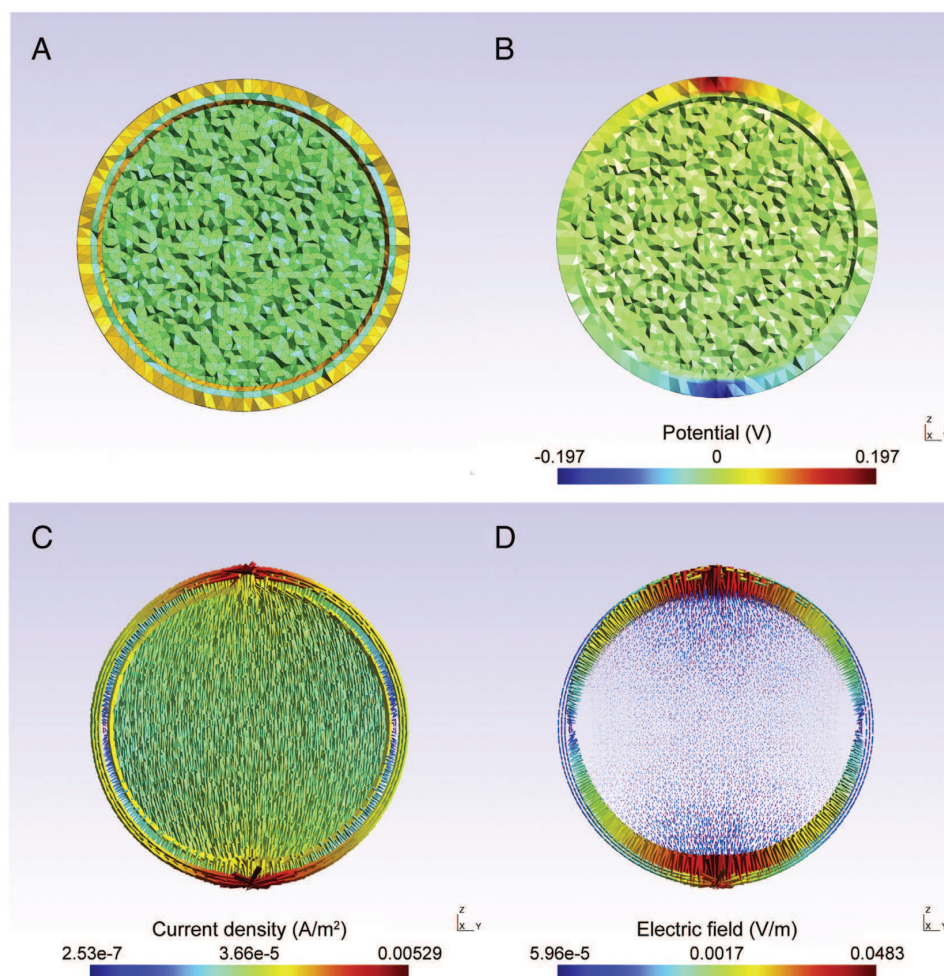
Fig. 1. Spherical mesh example. A) Sphere mesh geometry: Four-shell mesh including the brain, CSF, skull, and scalp. B) Potential distribution across the sphere (V): Single solution of the forward problem. Low potential is found at the sink electrode, and high potential is found at the current source. C) Current density distribution (A/m²). D) Electric field distribution (volts/m). Colors in C and D are on a logarithmic scale.

sensor location and the nodes of the scalp mesh. Electrodes were saved in the Gmsh mesh file as new distinct physical volumes, so that they could be assigned as current sources during the forward modeling. Fig. 2 shows the surface and volumetric meshes created for our subject alongside the original T1. The whole-head mesh contained 857,011 nodes and 5,916,850 tetrahedral elements.

Mapping conductivity tensors

Tensors were fit at each voxel using linear least squares as implemented in the FMRIB Software Library (Smith et al., 2004) build 504. A fractional anisotropy map was generated and linear registration was performed to align the FA to the T1-weighted structural image. The tensors were then registered to the structural image using the calculated

Table 1
Conductivity values and radii of the 4-shell spherical model.

Shell	Radius (mm)	Conductivity (S/m)
Brain	85	0.33
Cerebrospinal fluid	88	1.79
Skull	92	0.0042
Skin	100	0.33

transformation matrix and rotated accordingly. Diffusion tensor eigenvalues were remapped to produce conductivity tensors (Opitz et al., 2011) using functions from Dipy (Garyfallidis et al., 2014). The primary eigenvectors and mean conductivity map were assessed to check that the tensors had proper orientation and magnitude.

In order to include the diffusion tensors in the finite element structural model, the centroid of all tetrahedrons in the white matter 3D mesh was computed, and their location in the volumetric conductivity tensor data was obtained. If the centroid of the element was within a voxel, and that voxel had a fractional anisotropy greater than or equal to 0.1, then the tensor within that voxel was assigned to the element. The fractional anisotropy threshold is used solely to prevent inconsequential tensors from being included, and not to create a white matter mask. White matter elements whose centroids did not lie in a voxel (e.g. due to differing fields-of-view between the T1 and the DWI) were assigned isotropic conductivity values of 0.33 S/m. A coronal slice of the head model including the primary eigenvectors of the conductivity tensor can be found in Fig. 3. The full conductivity tensor is taken into account within the finite element model calculations, not just the anisotropy or principal direction.

In Table 4 we recorded the clock time and disk usage required to process the described subject (See Fig 4). These calculations were
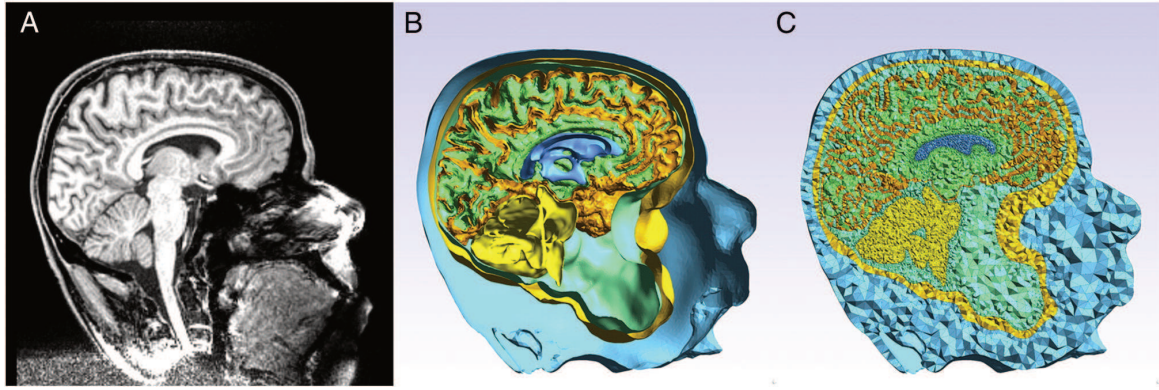
Fig. 2. Human head model. A) T1-weighted MRI image for our subject. B) Surface meshes: The head model output from the structural meshing pipeline consists of several 2D shells representing the gray matter, white matter, cerebellum, ventricles, CSF, scalp, and skin. C) 3D volume meshes. Volumetric meshes representing the scalp (light blue), skull (bright yellow), ventricles (blue), cerebrospinal fluid (green), gray matter (orange), white matter (light green), and cerebellum (yellow) are created from the 2D shells.

performed on a quad-core Xeon 2.6 GHz with 16 GB of RAM. The pipelines were run serially using a single CPU, and the total processing time was roughly 24 h.

Isotropic vs. anisotropic conductivity

Two leadfields were created: one with isotropic conductivity (L_{iso}) within the white matter and another incorporating the conductivity tensors described above (L_{aniso}). These two leadfields were compared by computing the root mean square deviation (RMSD) between the leadfield components, for each sensor–sink pair, in every element (N) of the gray matter. The RMSD was computed for each direction (i) of the electric field, because we felt averaging would ignore clear directional effects induced by the brain's white matter structure. The reader should recall that M is a list of EEG sensors.

$$\text{RMSD}^{N,i} = \frac{\sqrt{\sum_M \left(L_{iso}^{N,i} - L_{aniso}^{N,i}\right)^2}}{\left\| L_{iso}^{N,i} \right\|} \tag{6}$$

This provides a method for visualizing the spatial distribution of the effects of anisotropic white matter conductivity on the leadfield matrix.
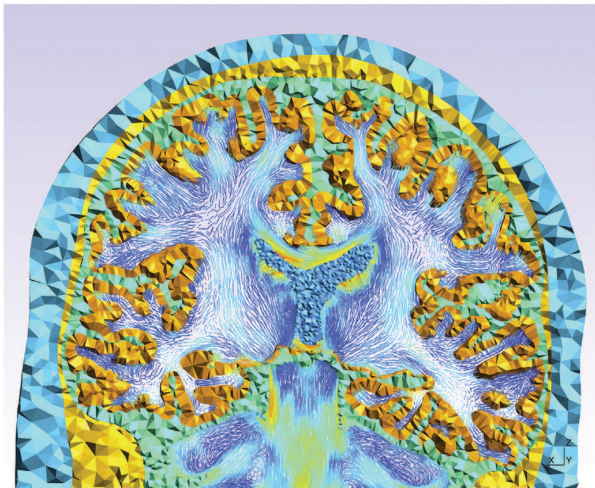

Fig. 3. Coronal slice of head model. Primary eigenvectors of the conductivity tensor are shown within the white matter. The 3D gray matter (orange), cerebrospinal fluid (green), ventricles (blue), skull (yellow), and scalp (light blue) meshes are also shown.

Areas of high RMSD may be prone to source reconstruction errors in studies where isotropic conductivity is assumed.

Residual function mapping

We further tested our forward model by calculating single-dipole residual fields for both the isotropic and anisotropic leadfields. The residual function relays the misfit between the scalp potential obtained from a pre-specified dipole and the potential that would be produced if optimally oriented dipoles were placed in each element.

First, a current dipole is placed inside one element and the "measured" scalp potential is obtained (Φ). Within each element, any dipole (j) will produce a scalp potential ($\hat{\Phi}$) that can be derived from the precomputed leadfield (L):

$$Lj = \hat{\Phi}. \tag{7}$$

The optimal location of a single dipole can be found by minimization of the residual function (R):

$$R = \left(\hat{\Phi} - \Phi\right)^T \left(\hat{\Phi} - \Phi\right). \tag{8}$$

Table 2
Summary statistics of RDM and MAG.

Method	RDM	MAG
GetDP	0.013 (0.003)	1.033 (0.060)
OpenMEEG	0.125 (0.408)	1.345 (2.400)
SimBio	0.008 (0.002)	1.018 (0.031)

Summary of RDM and MAG values across varying dipole depths in the spherical model. Values represent mean (standard deviation). See Fig. 5.

Table 3
Summary statistics of RMSD between isotropic and anisotropic leadfields.

Direction	RMSD
Left–right (X)	0.378 (0.237)
Anterior–posterior (Y)	0.312 (0.188)
Inferior–superior (Z)	0.295 (0.191)
Average	0.328 (0.125)

Summary of root mean squared deviation between leadfields created from meshes with isotropic white matter conductivity and anisotropic white matter conductivity tensors. Values represent mean (standard deviation). See Fig. 6.

Table 4
Computational cost and storage required for each step.

Task	Time (HH:MM:SS)	Disk usage (GB)
Initial reconstruction	14:16:16	0.4
Structural meshing	04:05:11	2.4
Diffusion tensor processing	00:36:35	0.9
Electrode incorporation	00:01:00	0.6
Leadfield creation	04:21:17	19.5
Total	23:20:19	23.8

Initial reconstruction was performed with FreeSurfer 5.3 using the "recon-all" command with the option "–autorecon-all".

If $\hat{\Phi}$ is set to the measured potential (Φ), the best moment of this dipole is given by Eq. (9).

$$j = L^+\Phi \tag{9}$$

where L^+ represents the Moore–Penrose pseudo-inverse ($L^+ = (L^TL)^{-1}L^T$) of the leadfield matrix. Since the optimal orientation can be calculated in this manner, the residual can be calculated as:

$$R = \hat{\Phi}^T\left[I - LL^+\right]\hat{\Phi}. \tag{10}$$

The location of the global minimum of the residual function reflects the best guess for the position of the dipole within the mesh.

Results

The relative difference (RDM) and relative magnitude (MAG) between our method and the analytical solution across the 22 tested dipole positions can be found in Fig. 5. Summary statistics calculated from these data points are available in Table 2.

We found that both our implementation and that of SimBio provide more spatially stable and accurate solutions than the boundary element approach available in OpenMEEG. At locations near the tissue boundaries (<15 mm) the OpenMEEG solution differed substantially (RDM > 0.05) from the analytical solution, whereas both FEM approaches remained relatively accurate (RDM < 0.02). SimBio appears to be the most accurate approach overall as it marginally outperforms our implementation on both RDM and MAG.

Notable jaggedness is present in the RDM and MAG plots for the GetDP solution. This is because probe dipoles are snapped into the closest mesh elements (by Euclidean distance) in order to calculate the potential at the sensors. SimBio and OpenMEEG, in contrast, provide continuous solutions. This issue can be mitigated by reducing the characteristic length of the mesh elements (i.e. increasing mesh resolution)
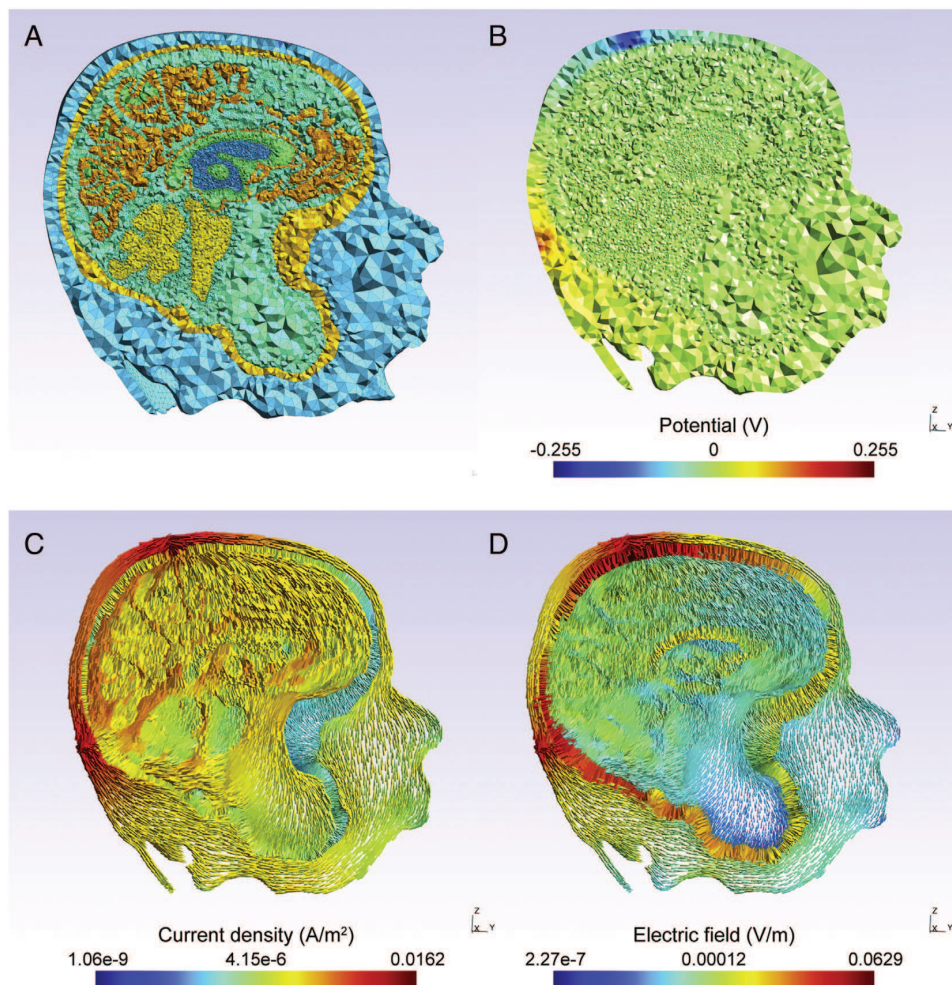

Fig. 4. Whole-head example. A) Head model geometry: Four-shell mesh including the brain, CSF, skull, and scalp. B) Potential distribution throughout the head (V). C) Current density distribution (A/m^2). D) Electric field distribution (V/m). Colors in C and D are on a logarithmic scale.
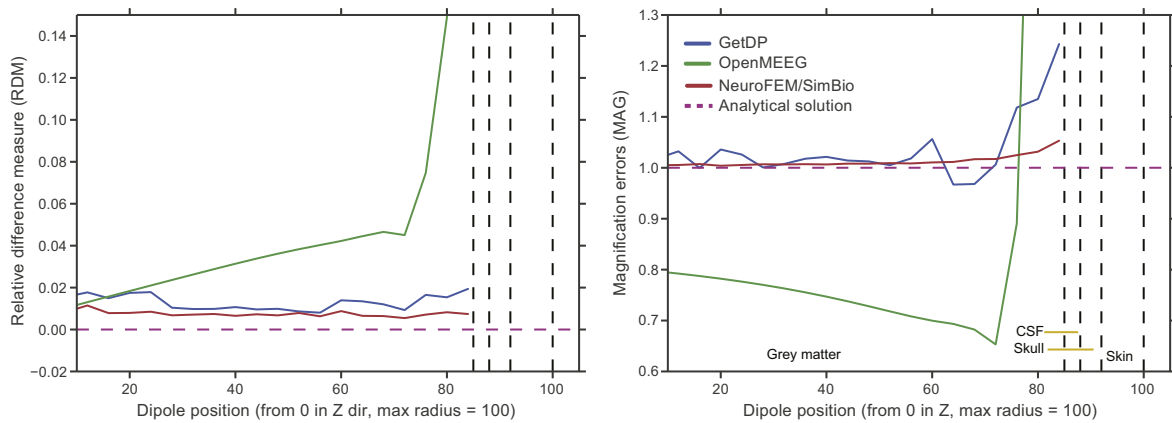
Fig. 5. Accuracy comparison between forward modeling methods. Comparison between the relative difference measure (RDM) and relative magnitude (MAG) for our FEM reciprocity implementation (in blue), the FEM solution implemented in NeuroFEM/SimBio (in red), and the symmetric BEM solution implemented in OpenMEEG (Gramfort et al., 2010) (in green). The horizontal pink dashed line shows the analytical solution. Vertical black dashed lines show the boundaries between tissue shells.

or widening the probe dipole sampling distance to a value larger than the characteristic length of the elements. In this case, we chose to place dipoles every 4 mm because our tetrahedra were defined with characteristic lengths of 3 mm.

In the human brain model, the incorporation of DWI-derived conductivity tensors substantially influenced the leadfield matrices that were created. The influence of incorporating anisotropic conductivity information into the leadfield matrix was most pronounced in regions connected by large fiber bundles. As shown in Fig. 6, we found that the root mean squared deviation (RMSD) between the "isotropic" and "anisotropic" leadfields followed the pattern of major fiber tracts in the brain. Along the left–right axis (x direction), the largest RMSD between isotropic and anisotropic leadfields was found in gray matter regions connected by the corpus callosum. RMSD in the left–right axis was also particularly high in the precuneus and occipital lobe. Along the anterior–posterior axis (y direction), the largest RMSD was found

near the anterior and posterior cingulate. Along the inferior–superior axis (z direction), the largest RMSD was found near the corticospinal tracts at both the mesencephalic and cortical levels. The left–right RMSD showed the highest mean (0.378) and widest deviation (0.237) between the isotropic and anisotropic leadfields, likely due to the influence of the corpus callosum. The influence of anisotropy, measured as the mean degree of error between leadfields, was smallest along the inferior–superior axis (0.295). Table 3 shows the influence of anisotropy by direction.

In Fig. 7 the residual function fields for a dipole in the left superior frontal lobe are shown. The residual function in the leadfield with isotropic conductivity showed a wider distribution of low residual values throughout the brain and across hemispheres compared to the more realistic anisotropic head model. This lack of specificity in the isotropic head model is likely to result in errors when attempting to localize sources using an inverse solver.
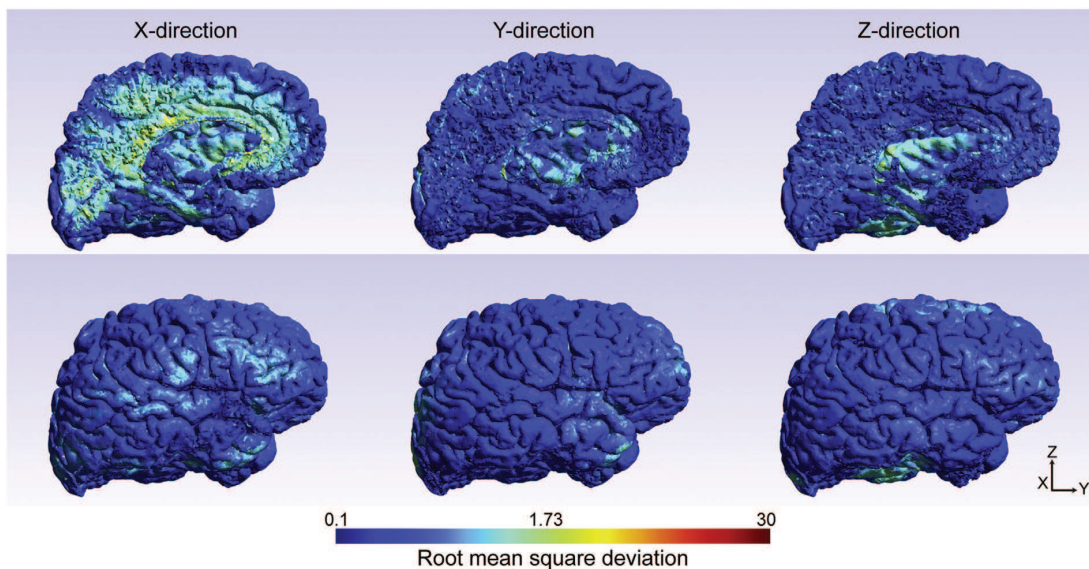

Fig. 6. Root mean square deviation between leadfields created with and without white matter conductivity tensors. Leadfield root mean square deviation maps show the influence of including white matter conductivity tensors on the created leadfield matrices. Color is on a logarithmic scale.
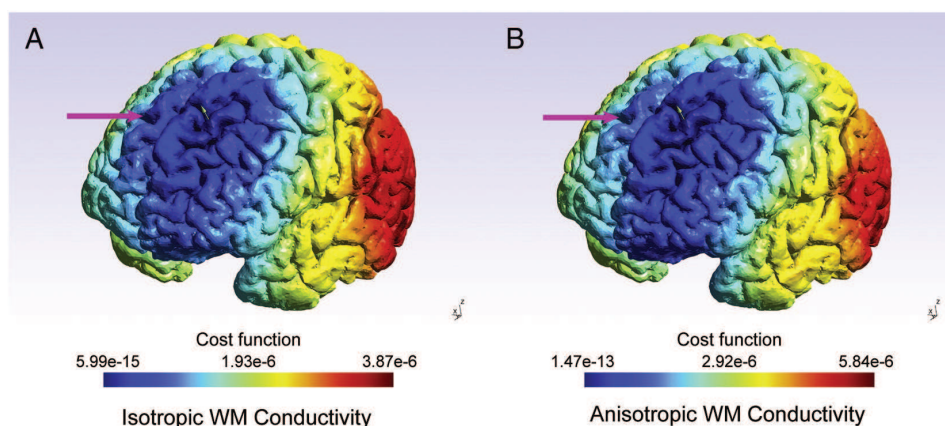
Fig. 7. Single-dipole residual fields. Residual field for A) the leadfield with isotropic WM conductivity, and B) the leadfield including realistic WM conductivity tensors. The residual field is calculated by placing a single dipole within the mesh, and then obtaining the difference between the scalp potential produced by this dipole, and the potential produced by an optimal dipole placed in each other element, individually. The minimum of this field represents the dipole position. As shown by the pink arrows, the residual minima bleed further into the opposite hemisphere within the isotropic leadfield, compared to the more realistic conductivity model.

Discussion

Here we have demonstrated a solution for calculating the EEG leadfield matrix using realistic, heterogeneous, and anisotropically conducting head models. The accuracy of the current forward modeling method was validated by its agreement with the analytical solution in a four-shell spherical model. The approach was found to perform better than the current state-of-the-art symmetric BEM approach (OpenMEEG) and marginally worse than the only other available FEM implementation (SimBio). The ability to take into account anisotropic conductivity information was demonstrated with real human MRI data.

Two recent simulation studies have extended simple three-compartment head models to complex six-compartment models step-by-step to study the effects of modeling various aspects of the human head (Vorwerk et al., 2014; Wagner et al., 2014). Both studies also included anisotropic conductivity information derived from diffusion tensors. They found that anisotropic conductivity information has a strong effect on the EEG/MEG forward model, second only to the effect of including a separate CSF compartment and including distinct compartments for both gray and white matter (Vorwerk et al., 2014).

It has now been established that current flows in the brain (e.g. following transcranial direct current stimulation) along trajectories parallel to the primary direction of the fiber tracts (Wagner et al., 2014; Wolters et al., 2006). Sources located deep in the brain, as well as those bordering strongly anisotropic tissue, are misrepresented in EEG localization when neglecting the effects of white matter anisotropy (Wolters et al., 2006). One recent study that included an inverse analysis found that sulcal sources localized in EEG studies may be mislocalized outside of the sulci if white matter anisotropy is neglected (Güllmar et al., 2010). The dipole shift for these sources tended to be parallel to the principal direction of the nearby white matter. An earlier study estimated that ignoring white matter anisotropy could lead to dipole localization errors greater than 10 mm on average (Hallez et al., 2005). Our results show strong errors in the leadfield nearby large white matter tracts. Deviation between leadfields in all directions was more pronounced in sulci than gyri, reaffirming previously reported results (Güllmar et al., 2010). Anisotropic conductivity information should not be ignored in neural source imaging studies.

While we have not yet integrated our approach with available inverse solvers, we have shown that our forward model is stable and accurate. The meshing pipelines provided here may also prove useful for other types of finite-element simulations, such as those evaluating neurotrauma mechanics (Kraft et al., 2012). The finite element solution used during leadfield creation may also be adaptable for other types of simulations, such as the modeling of transcranial direct current stimulation. At present the toolbox is incapable of producing magnetoencephalography (MEG) leadfield matrices. Reciprocity solutions for MEG leadfields have been previously demonstrated (Schimpf, 2007), however, and this framework could be extended to allow for their creation.

Our approach contains many advantages over other competing methods. Whereas boundary element methods are usually restricted to nested shells (Kybic et al., 2006), finite element methods allow for complex geometry in the head models. This means that an individual head model could be created, for example, for a patient with a hole, fracture, or implant in their skull. Furthermore, our FE mesh is of higher quality than many previous studies, as we use an unstructured tetrahedral mesh, rather than structured hexahedral grids (used in e.g. Güllmar et al., 2010; Wagner et al., 2014). This allows us to refine the mesh for more realistic calculations within highly curved regions of the brain. It may also be beneficial to implement anisotropy-adaptive mesh generation (Lee and Kim, 2012). The non-uniformly tessellated mesh also sets the FEM approach apart from finite difference methods (FDM). One such finite difference reciprocity method has recently been demonstrated, though the publication only reports results in a head model with four distinct tissue types, and does not include realistic directional conductivity information (Strobbe et al., 2014).

There is one major electromagnetic property of the human head that we have overlooked in this study: the conductivity profile of the skull. Errors in skull segmentation are known to cause substantial issues in source localization (Lanfer et al., 2012). The skull is actually composed of three layers: one layer of spongy bone encased by two layers of more compact bone, each with distinct conductivities (Akhtari et al., 2002). Furthermore, it contains some air cavities (e.g. near the sinuses), and varies in thickness around the head (Law, 1993). It is also well known that the skull conducts faster radially than tangentially, leading to a smearing effect on the recorded scalp EEG (Rush and Driscoll, 1968). It has recently been shown, however, that geometrical modeling errors of the skull have a larger effect on electromagnetic source localization than the conductivity model assigned to the skull region(s) (Montes-Restrepo et al., 2014). At present our implementation uses a simple single-shell skull with an isotropic conductivity of 0.0042 S/m (roughly 1/80th that of the gray matter) (Rush and Driscoll, 1968). Segmenting the skull into three compartments is difficult from T1-weighted MR images and additional sequences may be necessary. Future avenues for reducing localization error by improving the skull model are (i) including a three-layer model, and (ii) including tensor-based anisotropy measures based on radial and tangential skull conductivity measurements.

Skull and CSF segmentation guided by T1 and T2-weighted MRI is available in the processing pipelines (using BET Jenkinson et al., 2005; Smith, 2002), though they were not demonstrated specifically here. A comparison of FE models generated from a single T1-weighted image and an optimal set of four images (T1, T2, and fat-suppressed T1/T2 images) is available in the Supplementary information. Qualitatively, the optimal set of images allows for more accurate segmentation, but the mesh generated from a single T1 image does appear to be of sufficient quality.

The primary disadvantage of our implementation versus those currently in use is the computational requirements and data storage cost. It is clear from our study and others, though, that accuracy in the conductivity model used for forward modeling is imperative for realistic source localization. Data storage issues for the triangular surface meshes may be mitigated in the future by incorporating entropy-reduction techniques and entropy encoding. One such available option is the OpenCTM format (Geelnard, 2010), which can losslessly encode triangular meshes to 5–6% of their size in the commonly used Standard Tessellation Language (STL) mesh format.

This work is a suitable basis for future finite element electromagnetic modeling studies of the human head. It performs quickly and with better accuracy than the current state-of-the-art boundary element modeling approach, and proves more stable near tissue boundaries. Its accuracy was found to be comparable to that of SimBio, a mature package for electromagnetic finite element modeling. Future work should interface this forward modeling approach with common EEG inverse solvers so the FEM approach becomes more widely adopted.

Technical details

The source code behind this manuscript is available at the online repository service Github (https://CyclotronResearchCentre.github.io/forward/, GNU GPL v2 software license). Minimum recommended system requirements are a quad-core 2.0 GHz processor and 4 GB of RAM. Dependencies are Nipype (Gorgolewski et al., 2011), Dipy (Garyfallidis et al., 2014), the FMRIB Software Library (Smith et al., 2004), Gmsh (Geuzaine and Remacle, 2009), and GetDP (Dular et al., 1998). The MRI data for the example subject demonstrated in this manuscript is automatically downloaded when running any of the examples in the software package.

Input data files for the software are high-quality T1-weighted magnetic resonance images. T1-weighted images should have previously been segmented using FreeSurfer (Desikan et al., 2006), and the subject's white matter surfaces, pial surfaces, bias-corrected T1-weighted image, and segmented ROI map (using FreeSurferColorLUT labeling) should be available. If available, the pipelines will accept an additional T2-weighted image, or a set of four images (T1, T2 and fat-suppressed T1 and T2-weighted images), as in SimNIBS (Windhoff et al., 2013). The tool will also accept diffusion-weighted images so that conductivity tensors can be derived for the subject. Diffusion preprocessing (e.g. correction for subject motion, eddy current-induced distortions, and table vibrations) should be performed prior to using the pipelines.

Primary output files are the leadfield matrix and volumetric head mesh (Gmsh MSH). The leadfield, which can become several hundred megabytes, depending on the mesh complexity, is stored as an HDF5 data file (The HDF Group. Hierarchical data format version 5, 2000–2010. http://www.hdfgroup.org/HDF5). Other outputs are the surface meshes of the skin, skull, cerebrospinal fluid, ventricles, gray matter, and white matter. Volumetric masks of the segmented structures are also provided in the NIfTI-1 data format. Part of this work included migrating the SimNIBS meshing scripts to use Nipype (Gorgolewski et al., 2011). The provenance tracking in Nipype allows users to easily stop and restart the pipelines without any fear of lost data. This is enormously helpful for using and improving long-running, complex pipelines. Furthermore, Nipype allows jobs to be executed on distributed systems,

such as cloud processing services, as well as locally on multi-core systems. The meshes created from the structural meshing pipeline can also be easily re-used in SimNIBS, if desired. If multimodal meshes are to be included in place of the T1-derived mesh (e.g. the skull segmented from a CT scan), they must be centered at the RAS center (i.e. right, anterior, and superior are the positive x, y, and z directions) of the T1 image used for segmentation. The source code contains Gmsh example scripts for manually creating the 3D mesh file.

Appendix A. Supplementary data

Supplementary data to this article can be found online at http://dx.doi.org/10.1016/j.neuroimage.2014.08.056.

References

Acar, Z.A., Makeig, S., 2010. Neuroelectromagnetic forward head modeling toolbox. J. Neurosci. Methods 190, 258–270.

Akhtari, M., Bryant, H., Mamelak, A., Flynn, E., Heller, L., Shih, J., Mandelkem, M., Matlachov, A., Ranken, D., Best, E., et al., 2002. Conductivities of three-layer live human skull. Brain Topogr. 14, 151–167.

André, E., Grinberg, D.F., Farrher, E., Maximov, I.I., Shah, N.J., Meyer, C., Jaspar, M., Muto, V., Phillips, C., Balteau, E., 2014. Influence of noise correction on intra- and inter-subject variability of quantitative metrics in diffusion kurtosis imaging. PLoS ONE 9, e94531.

Attene, M., 2010. A lightweight approach to repairing digitized polygon meshes. Vis. Comput. 26, 1393–1406.

Desikan, R.S., Ségonne, F., Fischl, B., Quinn, B.T., Dickerson, B.C., Blacker, D., Buckner, R.L., Dale, A.M., Maguire, R.P., Hyman, B.T., Albert, M.S., Killiany, R.J., 2006. An automated labeling system for subdividing the human cerebral cortex on MRI scans into gyral based regions of interest. NeuroImage 31, 968–980.

Dular, P., Geuzaine, C., Henrotte, F., Legros, W., 1998. A general environment for the treatment of discrete problems and its application to the finite element method. IEEE Trans. Magn. 34, 3395–3398.

Fingberg, J., Berti, G., Hartmann, U., Basermann, A., Zimmermann, F., Wolters, C., Anwander, A., McCARTHY, A., Woods, S., 2003. Bio-numerical simulations with SimBio. NEC Res. Dev. 44, 140–145.

Garyfallidis, E., Brett, M., Amirbekian, B., Rokem, A., Van Der Walt, S., Descoteaux, M., Nimmo-Smith, I., 2014. Dipy, a library for the analysis of diffusion MRI data. Front. Neuroinf. 8, 8.

Geelnard, M., 2010. OpenCTM, the Open Compressed Triangle Mesh File Format.

Geuzaine, C., Remacle, J.-F., 2009. Gmsh: a 3-D finite element mesh generator with built-in pre-and post-processing facilities. Int. J. Numer. Methods Eng. 79, 1309–1331.

Gorgolewski, K., Burns, C.D., Madison, C., Clark, D., Halchenko, Y.O., Waskom, M.L., Ghosh, S.S., 2011. Nipype: a flexible, lightweight and extensible neuroimaging data processing framework in Python. Front. Neuroinf. 5, 13.

Gramfort, A., Papadopoulo, T., Olivi, E., Clerc, M., 2010. OpenMEEG: opensource software for quasistatic bioelectromagnetics. Biomed. Eng. Online 9, 45.

Gramfort, A., Luessi, M., Larson, E., Engemann, D.A., Strohmeier, D., Brodbeck, C., Goj, R., Jas, M., Brooks, T., Parkkonen, L., Hämäläinen, M., 2013. MEG and EEG data analysis with MNE-Python. Front. Neurosci. 7, 267.

Gramfort, A., Luessi, M., Larson, E., Engemann, D.A., Strohmeier, D., Brodbeck, C., Parkkonen, L., Hämäläinen, M.S., 2014. MNE software for processing MEG and EEG data. NeuroImage 86, 446–460.

Güllmar, D., Haueisen, J., Reichenbach, J.R., 2010. Influence of anisotropic electrical conductivity in white matter tissue on the EEG/MEG forward and inverse solution. A high-resolution whole head simulation study. NeuroImage 51, 145–163.

Hallez, H., Vanrumste, B., Van Hese, P., D'Asseler, Y., Lemahieu, I., Van de Walle, R., 2005. A finite difference method with reciprocity used to incorporate anisotropy in electroencephalogram dipole source localization. Phys. Med. Biol. 50, 3787.

Helmholtz, H.V., 1853. Ueber einige gesetze der vertheilung elektrischer ströme in körperlichen leitern mit anwendung auf die thierisch-elektrischen versuche. Ann. Phys. 165, 211–233.

Jenkinson, M., Pechaud, M., Smith, S., 2005. BET2: MR-based estimation of brain, skull and scalp surfaces. In Eleventh Annual Meeting of the Organization for Human Brain Mapping.

Jones, D.K., Horsfield, M.A., Simmons, A., 1999. Optimal strategies for measuring diffusion in anisotropic systems by magnetic resonance imaging. Magn. Reson. Med. 42, 515–525.

Kariotou, F., 2004. Electroencephalography in ellipsoidal geometry. J. Math. Anal. Appl. 290, 324–342.

Kraft, R.H., Mckee, P.J., Dagro, A.M., Grafton, S.T., 2012. Combining the finite element method with structural connectome-based analysis for modeling neurotrauma: connectome neurotrauma mechanics. PLoS Comput. Biol. 8, e1002619.

Kybic, J., Clerc, M., Faugeras, O., Keriven, R., Papadopoulo, T., 2006. Generalized head models for MEG/EEG: boundary element method beyond nested volumes. Phys. Med. Biol. 51, 1333.

Lanfer, B., Scherg, M., Dannhauer, M., Knösche, T.R., Burger, M., Wolters, C.H., 2012. Influences of skull segmentation inaccuracies on EEG source analysis. NeuroImage 62, 418–431.

Law, S.K., 1993. Thickness and resistivity variations over the upper surface of the human skull. Brain Topogr. 6, 99–109.

Le Bihan, D., Johansen-Berg, H., 2012. Diffusion MRI at 25: exploring brain tissue structure and function. NeuroImage 61, 324–341.

Lee, W.H., Kim, T.-S., 2012. Methods for high-resolution anisotropic finite element modeling of the human head: automatic MR white matter anisotropy-adaptive mesh generation. Med. Eng. Phys. 34, 85–98.

Leemans, A., Jones, D.K., 2009. The B-matrix must be rotated when correcting for subject motion in DTI data. Magn. Reson. Med. 61, 1336–1349.

Litvak, V., Mattout, J., Kiebel, S., Phillips, C., Henson, R., Kilner, J., Barnes, G., Oostenveld, R., Daunizeau, J., Flandin, G., et al., 2011. EEG and MEG data analysis in SPM8. Comput. Intell. Neurosci. 852961.

Maggioni, M., Katkovnik, V., Egiazarian, K., Foi, A., 2013. Nonlocal transform-domain filter for volumetric data denoising and reconstruction. IEEE Trans. Image Process. 22, 119–133.

Montes-Restrepo, V., van Mierlo, P., Strobbe, G., Staelens, S., Vandenberghe, S., Hallez, H., 2014. Influence of skull modeling approaches on EEG source localization. Brain Topogr. 27, 95–111.

Munck, d.J., Peters, M.J., 1993. A fast method to compute the potential in the multisphere model. IEEE Trans. Biomed. Eng. 40, 1166–1174.

Olivi, E., Papadopoulo, T., Clerc, M., 2011. Handling white-matter anisotropy in BEM for the EEG forward problem. Biomedical Imaging: From Nano to Macro. IEEE International Symposium on, IEEE, pp. 799–802.

Oostenveld, R., Fries, P., Maris, E., Schoffelen, J.-M., 2011. FieldTrip: open source software for advanced analysis of MEG, EEG, and invasive electrophysiological data. Comput. Intell. Neurosci. 156869.

Opitz, A., Windhoff, M., Heidemann, R.M., Turner, R., Thielscher, A., 2011. How the brain tissue shapes the electric field induced by transcranial magnetic stimulation. NeuroImage 58, 849–859.

Reese, T.G., Heid, O., Weisskoff, R.M., Wedeen, V.J., 2003. Reduction of eddy-current-induced distortion in diffusion MRI using a twice-refocused spin echo. Magn. Reson. Med. 49, 177–182.

Rullmann, M., Anwander, A., Dannhauer, M., Warfield, S.K., Duffy, F.H., Wolters, C.H., 2009. EEG source analysis of epileptiform activity using a 1 mm anisotropic hexahedra finite element head model. NeuroImage 44, 399–410.

Rush, S., Driscoll, D., 1968. Current distribution in the brain from surface electrodes. Anesth. Analg. 47, 717.

Rush, S., Driscoll, D.A., 1969. EEG electrode sensitivity — an application of reciprocity. IEEE Trans. Biomed. Eng. 15–22.

Sarvas, J., 1987. Basic mathematical and electromagnetic concepts of the biomagnetic inverse problem. Phys. Med. Biol. 32, 11.

Schimpf, P.H., 2007. Application of quasi-static magnetic reciprocity to finite element models of the MEG lead-field. IEEE Trans. Biomed. Eng. 54, 2082–2088.

Schimpf, P.H., Ramon, C., Haueisen, J., 2002. Dipole models for the EEG and MEG. IEEE Trans. Biomed. Eng. 49, 409–418.

Shirvany, Y., Rubæk, T., Edelvik, F., Jakobsson, S., Talcoth, O., Persson, M., 2013. Evaluation of a finite-element reciprocity method for epileptic EEG source localization: accuracy, computational complexity and noise robustness. Biomed. Eng. Lett. 3, 8–16.

Smith, S.M., 2002. Fast robust automated brain extraction. Hum. Brain Mapp. 17, 143–155.

Smith, S.M., Jenkinson, M., Woolrich, M.W., Beckmann, C.F., Behrens, T.E.J., Johansen-Berg, H., Bannister, P.R., Luca, M.D., Drobnjak, I., Flitney, D.E., Niazy, R.K., Saunders, J., Vickers, J., Zhang, Y., Stefano, N.D., Brady, J.M., Matthews, P.M., 2004. Advances in functional and structural MR image analysis and implementation as FSL. NeuroImage 23 (Suppl. 1), S208–S219.

Strobbe, G., van Mierlo, P., De Vos, M., Mijović, B., Hallez, H., Van Huffel, S., López, J.D., Vandenberghe, S., 2014. Bayesian model selection of template forward models for EEG source reconstruction. NeuroImage 93, 11–12.

Tuch, D.S., Wedeen, V.J., Dale, A.M., George, J.S., Belliveau, J.W., 2001. Conductivity tensor mapping of the human brain using diffusion tensor MRI. Proc. Natl. Acad. Sci. U. S. A. 98, 11697–11701.

Vallaghé, S., Papadopoulo, T., Clerc, M., 2009. The adjoint method for general EEG and MEG sensor-based lead field equations. Phys. Med. Biol. 54, 135.

Vanrumste, B., Van Hoey, G., Van de Walle, R., Michel, R.D., Lemahieu, I.A., Boon, P.A., 2001. The validation of the finite difference method and reciprocity for solving the inverse problem in EEG dipole source analysis. Brain Topogr. 14, 83–92.

Vorwerk, J., Cho, J.-H., Rampp, S., Hamer, H., Knösche, T.R., Wolters, C.H., 2014. A guideline for head volume conductor modeling in EEG and MEG. NeuroImage 100, 590–607.

Wagner, S., Rampersad, S., Aydin, Ü., Vorwerk, J., Oostendorp, T., Neuling, T., Herrmann, C., Stegeman, D., Wolters, C., 2014. Investigation of tDCS volume conduction effects in a highly realistic head model. J. Neural Eng. 11, 016002.

Weinstein, D., Zhukov, L., Johnson, C., 2000. Lead-field bases for electroencephalography source imaging. Ann. Biomed. Eng. 28, 1059–1065.

Windhoff, M., Opitz, A., Thielscher, A., 2013. Electric field calculations in brain stimulation based on finite elements: an optimized processing pipeline for the generation and usage of accurate individual head models. Hum. Brain Mapp. 34, 923–935.

Wolters, C., Anwander, A., Tricoche, X., Weinstein, D., Koch, M., MacLeod, R., 2006. Influence of tissue conductivity anisotropy on EEG/MEG field and return current computation in a realistic head model: a simulation and visualization study using high-resolution finite element modeling. NeuroImage 30, 813–826.

Wolters, C.H., Köstler, H., Möller, C., Härdtlein, J., Grasedyck, L., Hackbusch, W., 2007. Numerical mathematics of the subtraction method for the modeling of a current dipole in EEG source reconstruction using finite element head models. SIAM J. Sci. Comput. 30, 24–45.

A finite-element reciprocity solution for EEG forward modeling with realistic individual head models

Erik Ziegler[1,*], Sarah L. Chellappa[1], Giulia Gaggioni[1], Julien Q. M. Ly[1], Gilles Vandewalle[1], Elodie André[1], Christophe Geuzaine[2,+], Christophe Phillips[1,2,+]

1 Cyclotron Research Centre, University of Liège, Liège, Belgium
2 Department of Electrical Engineering and Computer Science, University of Liège, Liège, Belgium
∗ **E-mail: erik.ziegler@ulg.ac.be**
+ **Contributed equally**

Supplementary Material

Mathematical background

We start from Maxwell's equations, and assume that all phenomena are time independent (quasi-static approximation) [1,2]. By taking the divergence of Ampère's law $\nabla \times h = j$ (where h is the magnetic field and j is the current density), we obtain the current conservation law:

$$\nabla \cdot j = 0. \tag{1}$$

The current density j is also related to the local electric field e in the domain Ω (i.e., the subject's head) through the electric conductivity (tensor) σ by Ohm's law:

$$j = \sigma e. \tag{2}$$

Since all phenomena are time independent, Faraday's law states that the curl of the electric field is zero: $\nabla \times e = 0$. This implies that the electric field e can be derived from a scalar potential Φ, such that:

$$e = -\nabla\Phi. \tag{3}$$

Using (2) and (3), (1) becomes

$$-\nabla \cdot \sigma\nabla\Phi = 0 \quad \text{in } \Omega. \tag{4}$$

Equation (4) is a linear Poisson equation, which describes the distribution of the electric potential within the head, provided that appropriate boundary conditions are specified on the boundary $\partial\Omega$ of the domain Ω. In the problem at hand

1. we impose the electric potential on the electrodes $\Gamma_D \subset \partial\Omega$, i.e., we impose non-homogeneous Dirichlet conditions on Γ_D:

$$\Phi = \Phi_D \quad \text{on } \Gamma_D; \tag{5}$$

2. we impose a zero normal derivative of the electric potential elsewhere, i.e. a zero flux of the current density on the rest of the scalp:

$$n \cdot \sigma\nabla\Phi = 0 \quad \text{on } \partial\Omega \setminus \Gamma_D. \tag{6}$$

Physically, this last boundary condition means that no current can flow in or out of the scalp outside of the electrodes.

We use the finite element method to solve a weak form of (4) together with boundary conditions (5)–(6). In short, the aim of the method is to find the electric potential Φ satisfying the boundary conditions and such that the following equation holds for all suitable test functions Φ' in an appropriate function space:

2

$$\int\limits_{\Omega} \sigma \nabla \Phi \cdot \nabla \Phi' d\Omega = 0 \tag{7}$$

Symbolically, this is expressed in a GetDP formulation [3] as "`Galerkin[sigma[] * Dof{Grad phi}, {Grad phi}]`".

The basis described allows us to solve the forward problem throughout the head model with no restrictions on the geometry of the meshes. We can easily solve these equations using GetDP, an environment for discrete problem solving, and no tweaking of the solver is required. To further improve the efficiency of leadfield creation, we implemented the reciprocity method.

Meshing considerations

We investigated the benefit of including T2-weighted images during head tissue segmentation in a single subject. Figure 2 shows volumetric meshes created using either a single fat-suppressed T1-weighted image or a set of four images (T1-weighted, T2-weighted, and fat-suppressed T1 and T2-weighted MRI). While there is some discernible benefit to the segmentation of skin and cerebrospinal fluid, there does not appear to be any major segmentation errors in the meshes created solely from the T1. If possible, users should include T2-weighted images when running the meshing pipelines. If they are not available, however, it appears that a T1-weighted image is sufficient for accurate segmentation. MR images in Figure 2 are from the SimNIBS Example Dataset (available at `http://www.simnibs.de`).

Supplementary Figures
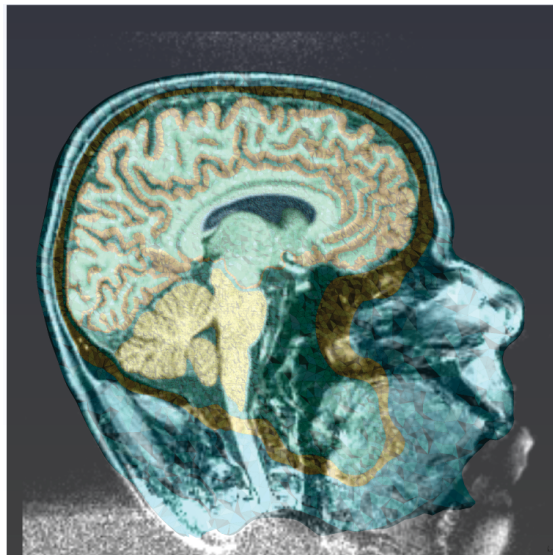
Figure 1. Finite element mesh overlaid on T1-weighted image

3

References

1. Plonsey R, Heppner DB (1967) Considerations of quasi-stationarity in electrophysiological systems. The Bulletin of mathematical biophysics 29: 657–664.

2. Sarvas J (1987) Basic mathematical and electromagnetic concepts of the biomagnetic inverse problem. Physics in medicine and biology 32: 11.

3. Dular P, Geuzaine C, Henrotte F, Legros W (1998) A general environment for the treatment of discrete problems and its application to the finite element method. Magnetics, IEEE Transactions on 34: 3395–3398.

Meshes constructed from a single fat-suppressed T1-weighted MRI
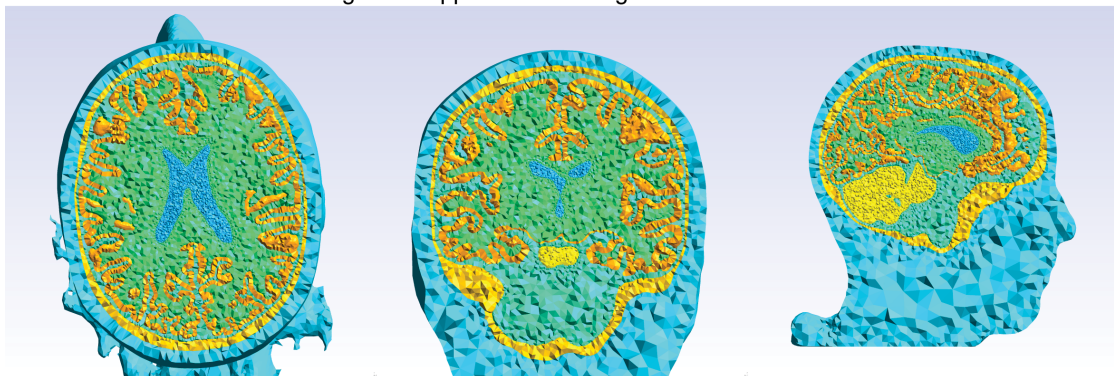
Meshes constructed from four MR images (T1, T2, fat-suppressed T1 and T2)
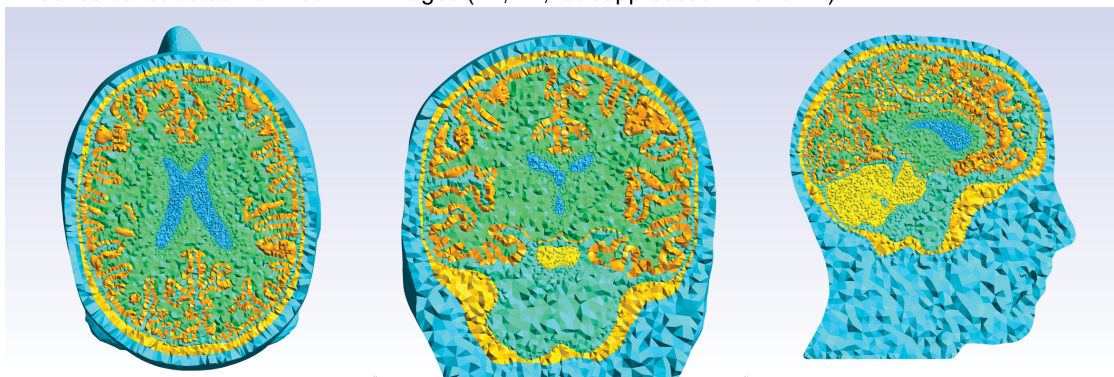
Original fat-suppressed T1-weighted MRI
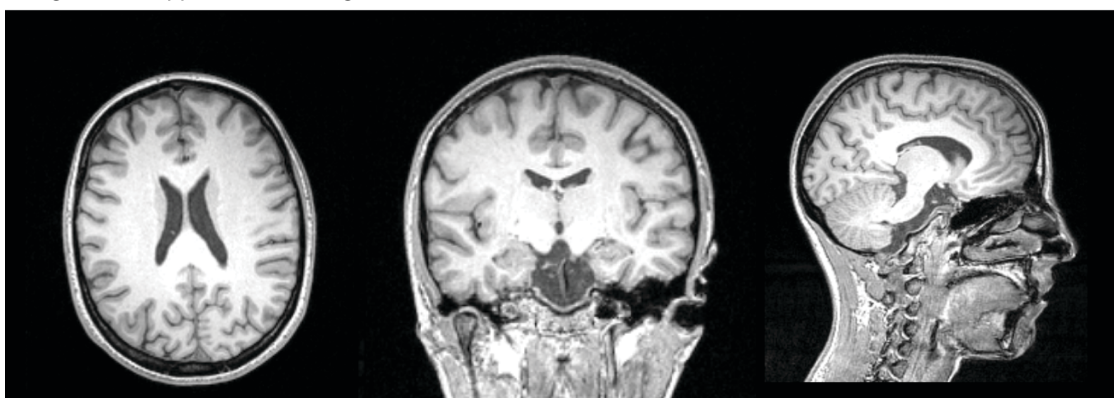
Figure 2. Finite element meshes from different MR origins

APPENDIX D
Valorization

Researchers at Maastricht University are expected to discuss the social and economic value of the knowledge developed during their doctoral studies. This chapter addresses the present and potential impact of this thesis.

Social & economic relevance

In this work we first explored the influence of genetics on the macro-scale structural connectivity of the human brain. We targeted an important and widespread neurotrophic growth factor (BDNF). Every human carries the *BDNF* gene in one of three forms, and polymorphisms in *BDNF* are known to impact both behaviour and disease susceptibility [128]. The study involved constructing brain networks (*connectomes*) and using machine learning classification algorithms to identify them by their *BDNF* allele. Alongside previously published studies, the results we obtained in Paper I (Appendix A) suggest that individuals carrying a specific form of this gene may show less pronounced cognitive decline during old age. Based on *in vitro* studies we hypothesize that this is due to impairments in axonal pruning during brain development. This is especially socially important considering that over the next 20 years, the number of people aged 65 and over in the global population will climb from 600 million to 1.1 billion [213].

Cell signalling via the BDNF protein has long been known to be key step in axonal development and branching, though it was only recently found that this can also facilitate apoptosis [214]. Our results reinforce earlier findings of macroscopic changes related to genetic alterations in the *BDNF* gene and provide a link between cellular-level and psychological studies. Understanding the mechanisms behind cognitive impairment may help researchers develop drugs that can slow or delay cognitive decline.

The second chapter of this thesis demonstrated an encouraging *in vivo* magnetic resonance imaging method capable of detecting early-stage changes in patients with Parkinson's disease. In developed countries, PD affects roughly 1% of those over 60 years old and following Alzheimer's disease it is the world's second most prevalent neurodegenerative disease [215]. In Western Europe's 5 most and the world's 10 most populous nations, it has been estimated that there will be nearly 9 million people with Parkinson's disease by 2030 [216]. These diseases also have biological links, as they both involve tangling of tau proteins. Novel methods for identifying disease onset and tracking severity are highly desired for preclinical testing of disease-modifying therapies. The method we have used in Paper II (Appendix B) can easily be adapted for animal imaging and could be a useful preclinical analysis tool. This project was made possible in part by a generous personal research grant I received from Amazon Web Services (AWS) in 2014.

Lastly, we produced a framework for EEG forward modelling using high-resolution finite element meshes. Over the course of this project a substantial amount of software was developed and open-sourced for the community. Although the software used for meshing and electromagnetic simulation are not completely novel, their integration and construction into workflows allows for easy and reproducible analyses. The method developed can help improve the accuracy of source localization in both research and clinical environments. These tools can also be used to simulate brain stimulation and modulation paradigms using techniques such as TMS, tDCS, tACS and DBS. These have wide-ranging social implications as they are commonly used to treat illnesses ranging from depression to Parkinson's disease.

The knowledge obtained here has led to the first (to our knowledge) successful 3D printed copy of a human white matter tractogram. Related developments in creating meshes from biological data have also led to a spin-off project. The spin-off has won nearly €20,000 in prizes and grants since its inception in the 3rd quarter of 2012. The team which developed the prototype software won the 2012 International Create Challenge in Martigny, Switzerland. They have since been awarded a

Bourse de Préactivité from the Agence de Stimulation Économique de Wallonie in Belgium and were finalists at the 2013 Innovact Campus Awards in Reims, France. The tractography model and others were recently exhibited at the World Intellectual Property Organization (WIPO) in Geneva. The cover photo shows a public roundtable meeting in which the founders of the spin-off were invited to discuss intellectual property rights related to 3D printing. The panel members included representatives of major Swiss universities, large multinational corporations, and ambassadors to various nations.

Figure D.1: 3D printed human tractogram. This teaching tool is a commercially available product developed using knowledge garnered through this doctoral work.

It is socially imperative to transmit scientific discoveries to the general public. Throughout my doctoral work I have participated in activities that help promote neuroscience. In 2011, I was awarded 1st place for a photograph in the "Promoting Science: Let's be innovative" competition at the Marie Curie Researcher's Symposium in Warsaw, where I also gave an invited talk on connectomics. A derivative piece of work was also featured in the magazine *Scientific American* [217]. In 2012, I produced various still images and videos that were displayed in the musée du

Louvre in Paris (and published in an associated book [218]) and Shanghai's Rock-bund Museum as part of the "Livre / Louvre" exposition by Jean-Philippe Toussaint. In 2013, I received an honorable mention at the Art of Neuroscience competition organized by the Netherlands Institute for Neuroscience.

Target group

The research results of the second chapter are immediately relevant to medical practitioners dealing with neurodegenerative disease, as they may offer a novel method to diagnose patients that are developing Parkinson's disease or similar neurodegenerative pathologies. Differential diagnosis of PD within the spectrum of Parkinsonian syndromes is complex. Misdiagnosis can lead to improper treatment (e.g. mismedication) and worsening of symptoms.

As this is an engineering thesis, it is not solely the results that are of interest to the community, but also the methods that have been developed. Those in the software engineering community, and especially those that work in the biomedical engineering field, can already benefit from the work done in this thesis because the source code has been made freely available. Alongside the Amazon Web Services research grant mentioned above, I was also awarded a high performance graphics processing unit (GPU) by the NVidia Corporation to facilitate open-source development of GPU computing methods in neuroscience.

Activities & Products

Automated diagnosis is ultimate goal of machine learning in medical imaging. No sole modality or analysis method can provide the best basis for sensitive and specific classification of all types of genetic or neurological abnormalities in the brain. This thesis has demonstrated both volumetric and white matter network-based approaches for discrimination between subjects' brains. All of my publications' source code and example data has been released to the public using Github and NITRC. The source code was designed to be modular and is provided as Python packages, making them relatively easy to integrate into larger-scale applications.

Neuromodulation techniques are repeatedly applied but their mechanisms of action and effect size are not modelled in most studies. Understanding the distribution and strength of stimulation modalities on a study-specific basis will undoubtedly help clarify their results. An application or service which can simplify the modelling

of stimulation techniques such as TMS, tDCS, tACS and DBS would be a useful tool for the neuroscientific community. This software could be developed and sold by a research institution or medical device manufacturer to both researchers and clinicians, assuming proper clearance procedures are followed. It would be beneficial to bundle this with the stimulation-guidance tools already in use.

So far, the spin-off mentioned has focused on web-based 3D modeling from multimodal medical images (CT, MRI, DWI). The 3D models produced are designed to be used for pre-surgical planning and patient education.

Innovation

Both Paper I and II incorporated innovative analysis techniques in order to identify differences between groups of subjects. In Paper I, we combined state-of-the-art fiber orientation modelling and tractography with network-based analysis and machine learning classification techniques. Our connectomes were built using a high-resolution 1015-region atlas based on an initial anatomically defined segmentation. To our knowledge, although there were some previous combinations of connectomics with machine learning, no published manuscripts had thusfar utilized similarly advanced methods of structural mapping.

Paper II was innovative in many respects. This paper was the first large-scale (n=53) application of track-weighted imaging in any population. The method, which provides super-resolution imaging of the white matter, had been demonstrated previously but never compared quantitatively. Furthermore, unlike all previous studies, we were able to identify abnormalities in the nigrostriatal pathway as well as extranigral regions using whole-brain statistics. Methodologically, Paper II was innovative in that we built and released workflows for track density imaging and comparison beginning from raw data. The study was performed using commercial on-demand cloud-based servers, and it is the first published study to utilize the recently released NITRC Computational Environment on AWS Elastic Compute Cloud.

Paper III combined diffusion-weighted imaging and structural MR imaging to produce accurate forward models for source reconstruction in electroencephalography. The toolbox developed allows for high-resolution head models to be calculated using 100% free software. It connects off-the-shelf open-source software using pipelines which can be easily be distributed across processing cores in a cluster or multi-core workstation. There is currently only one toolbox capable of producing an EEG lead-field matrix of similar quality (SimBio), but it was developed nearly ten years ago

and is practically unusable and unmaintained today. Our toolbox is modular and specific processing steps can be easily replaced when improved methods are made available.

In general, the availability of complex analysis approaches found in commercially available neuroscience software lags behind that of researcher-produced tools. This is by design, as the vast majority of developed techniques are not financially viable to develop and sell. Total available market sizes tend to be small and preparing a novel technique for clinical use is costly and time consuming. Commercial software aims to have more users and provide more stable and user-friendly tools than research software. Researchers are generally too busy writing papers or analyzing data to follow high-level software design and implementation practices. In this respect the work in this thesis was highly innovative in that advanced tools were developed in the open and were immediately available to anyone that wished to clone the repository. In collaboration with other researchers worldwide these tools have been constructed into reliable software packages (e.g. Nipype) with unit and continuous integration testing, so that future contributions do not break current features and stability is ensured.

Schedule & Implementation

Technological development in the biomedical field is impossible without financial backing. Financial backing relies on investors (public or private) to be sufficiently familiar with the technology they are being asked to fund. Outreach to the general public is therefore an important first step in any value-creation strategy. Human brain models designed and 3D printed based on research performed in this thesis have been publicly displayed on various occasions. In addition to the WIPO exhibition, they have also been shown in three TEDx Talks to date (in Martigny, Brussels, and Paris).

Commercial software, if it is eventually intended for clinical applications, must be the result of a rigorous design procedure (e.g. at least a Software Requirements Specification [219] and Software Design Document [220]). To attain the European CE mark and be cleared by the United States' Food and Drug Administration for clinical use, software must be reliably developed and include a hazard analysis and revision history, among other requirements. In all of the studies performed in this thesis, documented revision-controlled source code has been provided under commercially

permissive software licenses to help facilitate the production of commercially viable methodological tools and applications.

The spin-off described above intends to produce clinically cleared 3D modeling software based on the meshing procedures devised for Paper III. In 2013 a pre-submission ("Pre-sub") inquiry was filed and a teleconference performed with a number of division directors and reviewers at the U.S. Food and Drug Administration. The spin-off has been advised to file a 510(k) for the initial 3D modeling software, as this is sufficient if the models are used for surgical planning and patient education purposes. Subsequent 513(g) filings are advised for specific surgical cases (i.e. a single neurosurgical procedure). The initial 510(k) draft is in preparation and the spin-off is in active discussion with outside investors.

References

[1] D. Le Bihan (2003). Looking into the functional architecture of the brain with diffusion MRI. *Nature Reviews Neuroscience*, **4** (6): 469–480.

[2] D. Le Bihan, et al. (1986). MR imaging of intravoxel incoherent motions: application to diffusion and perfusion in neurologic disorders. *Radiology*, **161** (2): 401–407.

[3] J.-D. Tournier, et al. (2011). Diffusion tensor imaging and beyond. *Magnetic Resonance in Medicine*, **65** (6): 1532–1556.

[4] J. M. Soares, et al. (2013). A hitchhiker's guide to diffusion tensor imaging. *Frontiers in Neuroscience*, **7** (31).

[5] D. S. Tuch, et al. (2001). Measuring cortico-cortical connectivity matrices with diffusion spectrum imaging. In *Proceedings of International Society of Magnetic Resonance in Medicine*, volume 502.

[6] D. S. Tuch (2004). Q-ball imaging. *Magnetic Resonance in Medicine*, **52** (6): 1358–1372.

[7] C. G. Koay, et al. (2006). Investigation of anomalous estimates of tensor-derived quantities in diffusion tensor imaging. *Magnetic Resonance in Medicine*, **55** (4): 930–936.

[8] L.-C. Chang, et al. (2005). RESTORE: robust estimation of tensors by outlier rejection. *Magnetic Resonance in Medicine*, **53** (5): 1088–1095.

[9] J. Veraart, et al. (2013). Weighted linear least squares estimation of diffusion MRI parameters: Strengths, limitations, and pitfalls. *NeuroImage*, **81**: 335–346.

[10] D. K. Jones, et al. (2011). Diffusion tensor imaging. In *Magnetic Resonance Neuroimaging*, pages 127–144. Springer.

[11] J. H. Jensen, et al. (2005). Diffusional kurtosis imaging: The quantification of non-gaussian water diffusion by means of magnetic resonance imaging. *Magnetic Resonance in Medicine*, **53** (6): 1432–1440.

[12] J. H. Jensen, et al. (2010). MRI quantification of non-Gaussian water diffusion by kurtosis analysis. *NMR in Biomedicine*, **23** (7): 698–710.

[13] D. K. Jones, et al. (1999). Optimal strategies for measuring diffusion in anisotropic systems by magnetic resonance imaging. *Magnetic Resonance in Medicine*, **42** (3): 515–525.

[14] D. K. Jones (2004). The effect of gradient sampling schemes on measures derived from diffusion tensor MRI: a Monte Carlo study. *Magnetic Resonance in Medicine*, **51** (4): 807–815.

[15] D. S. Tuch, et al. (2002). High angular resolution diffusion imaging reveals intravoxel white matter fiber heterogeneity. *Magnetic Resonance in Medicine*, **48** (4): 577–582.

[16] D. B. Ennis, et al. (2006). Orthogonal tensor invariants and the analysis of diffusion tensor magnetic resonance images. *Magnetic Resonance in Medicine*, **55** (1): 136–146.

[17] G. Douaud, et al. (2011). DTI measures in crossing-fibre areas: *Increased* diffusion anisotropy reveals early white matter alteration in MCI and mild alzheimer's disease. *NeuroImage*, **55** (3): 880–890.

[18] S. Pajevic, et al. (1999). Color schemes to represent the orientation of anisotropic tissues from diffusion tensor data: application to white matter fiber tract mapping in the human brain. *Magnetic Resonance in Medicine*, **42** (3): 526–540.

[19] P. J. Basser, et al. (1994). Estimation of the effective self-diffusion *Tensor* from the NMR spin echo. *Journal of Magnetic Resonance, Series B*, **103** (3): 247–254.

[20] D. S. Tuch, et al. (2001). Conductivity tensor mapping of the human brain using diffusion tensor MRI. *Proceedings of the National Academy of Sciences*, **98** (20): 11697–11701.

[21] S. Oh, et al. (2006). Electrical conductivity estimation from diffusion tensor and T2: a silk yarn phantom study. In *Proc. Int. Soc. Magn. Reson. Med*, volume 14, page 3034.

[22] M. Akhtari, et al. (2006). Electrical conductivities of the freshly excised cerebral cortex in epilepsy surgery patients; correlation with pathology, seizure duration, and diffusion tensor imaging. *Brain Topography*, **18** (4): 281–290.

[23] D. Güllmar, et al. (2010). Influence of anisotropic electrical conductivity in white matter tissue on the EEG/MEG forward and inverse solution. a high-resolution whole head simulation study. *NeuroImage*, **51** (1): 145–163.

[24] M. Windhoff, et al. (2013). Electric field calculations in brain stimulation based on finite elements: an optimized processing pipeline for the generation and usage of accurate individual head models. *Human Brain Mapping*, **34** (4): 923–935.

[25] B. Jeurissen, et al. (2013). Investigating the prevalence of complex fiber configurations in white matter tissue with diffusion magnetic resonance imaging. *Human Brain Mapping*, **34** (11): 2747–2766.

[26] J. Tournier, et al. (2004). Direct estimation of the fiber orientation density function from diffusion-weighted MRI data using spherical deconvolution. *NeuroImage*, **23** (3): 1176–1185.

[27] J. Tournier, et al. (2013). Determination of the appropriate b value and number of gradient directions for high-angular-resolution diffusion-weighted imaging. *NMR in Biomedicine*, **26** (12): 1775–1786.

[28] C. M. Tax, et al. (2014). Recursive calibration of the fiber response function for spherical deconvolution of diffusion MRI data. *NeuroImage*, **86**: 67–80.

[29] D. Alexander, et al. (2002). Detection and modeling of non-Gaussian apparent diffusion coefficient profiles in human brain data. *Magnetic Resonance in Medicine*, **48** (2): 331–340.

[30] J. Tournier, et al. (2007). Robust determination of the fibre orientation distribution in diffusion MRI: non-negativity constrained super-resolved spherical deconvolution. *NeuroImage*, **35** (4): 1459–1472.

[31] J. Tournier, et al. (2008). Resolving crossing fibres using constrained spherical deconvolution: validation using diffusion-weighted imaging phantom data. *NeuroImage*, **42** (2): 617–625.

[32] G. Parker, et al. (2013). A pitfall in the reconstruction of fibre ODFs using spherical deconvolution of diffusion MRI data. *NeuroImage*, **65**: 433–448.

[33] F. Dell'Acqua, et al. (2010). A modified damped Richardson–Lucy algorithm to reduce isotropic background effects in spherical deconvolution. *NeuroImage*, **49** (2): 1446–1458.

[34] A. W. Anderson (2005). Measurement of fiber orientation distributions using high angular resolution diffusion imaging. *Magnetic Resonance in Medicine*, **54** (5): 1194–1206.

[35] P. Fillard, et al. (2011). Quantitative evaluation of 10 tractography algorithms on a realistic diffusion MR phantom. *NeuroImage*, **56** (1): 220–234.

[36] D. K. Jones, et al. (2013). White matter integrity, fiber count, and other fallacies: the do's and don'ts of diffusion MRI. *NeuroImage*, **73**: 239–254.

[37] J. Tournier, et al. (2012). MRtrix: diffusion tractography in crossing fiber regions. *International Journal of Imaging Systems and Technology*, **22** (1): 53–66.

[38] R. E. Smith, et al. (2012). Anatomically-constrained tractography: improved diffusion MRI streamlines tractography through effective use of anatomical information. *NeuroImage*, **62** (3): 1924–1938.

[39] R. E. Smith, et al. (2013). SIFT: Spherical-deconvolution informed filtering of tractograms. *NeuroImage*, **67**: 298–312.

[40] M. Reisert, et al. (2011). Global fiber reconstruction becomes practical. *NeuroImage*, **54** (2): 955–962.

[41] M.-A. Côté, et al. (2013). Tractometer: Towards validation of tractography pipelines. *Medical image analysis*, **17** (7): 844–857.

[42] P. F. Neher, et al. (2013). Fiberfox: Facilitating the creation of realistic white matter software phantoms. *Magnetic Resonance in Medicine*, **In Press**.

[43] M. Marcella Laganà, et al. (2012). Atlas-Based Versus Individual-Based Fiber Tracking of the Corpus Callosum in Patients with Multiple Sclerosis: Reliability and Clinical Correlations. *Journal of Neuroimaging*, **22** (4): 355–364.

[44] O. Sporns, et al. (2005). The human connectome: a structural description of the human brain. *PLoS Computational Biology*, **1** (4): e42.

[45] S. W. Oh, et al. (2014). A mesoscale connectome of the mouse brain. *Nature*, **508** (7495): 207–214.

[46] A. Zalesky, et al. (2010). Whole-brain anatomical networks: does the choice of nodes matter? *NeuroImage*, **50** (3): 970–983.

[47] R. S. Desikan, et al. (2006). An automated labeling system for subdividing the human cerebral cortex on MRI scans into gyral based regions of interest. *NeuroImage*, **31** (3): 968–980.

[48] A. Klein, et al. (2011). 101 labeled brain images and a consistent human cortical labeling protocol. *Frontiers in Neuroscience*, **6** (171).

[49] S. Gerhard, et al. (2011). The connectome viewer toolkit: an open source framework to manage, analyze, and visualize connectomes. *Front Neuroinform*, **5**: 3.

[50] A. Daducci, et al. (2012). The connectome mapper: an open-source processing pipeline to map connectomes with MRI. *PLoS One*, **7** (12): e48121.

[51] B. Fischl, et al. (2000). Measuring the thickness of the human cerebral cortex from magnetic resonance images. *Proceedings of the National Academy of Sciences*, **97** (20): 11050–11055.

[52] A. Klein, et al. (2009). Evaluation of 14 nonlinear deformation algorithms applied to human brain MRI registration. *NeuroImage*, **46** (3): 786–802.

[53] M. A. de Reus, et al. (2013). The parcellation-based connectome: Limitations and extensions. *NeuroImage*, **80**: 397–404.

[54] J. B. Colby, et al. (2012). Along-tract statistics allow for enhanced tractography analysis. *NeuroImage*, **59** (4): 3227–3242.

[55] A. A. Hagberg, et al. (2008). Exploring network structure, dynamics, and function using NetworkX. In *Proceedings of the 7th Python in Science Conference (SciPy2008)*, pages 11–15, Pasadena, CA USA.

[56] S. Achard, et al. (2012). Hubs of brain functional networks are radically reorganized in comatose patients. *Proceedings of the National Academy of Sciences*, **109** (50): 20608–20613.

[57] M. Bastiani, et al. (2012). Human cortical connectome reconstruction from diffusion weighted MRI: the effect of tractography algorithm. *NeuroImage*, **62** (3): 1732–1749.

[58] A. Zalesky, et al. (2010). Network-based statistic: identifying differences in brain networks. *NeuroImage*, **53** (4): 1197–1207.

[59] A. Zalesky, et al. (2012). The relationship between regional and inter-regional functional connectivity deficits in schizophrenia. *Human Brain Mapping*, **33** (11): 2535–2549.

[60] A. Zalesky, et al. (2012). Connectivity differences in brain networks. *NeuroImage*, **60** (2): 1055–1062.

[61] F. Calamante, et al. (2010). Track-density imaging (TDI): super-resolution white matter imaging using whole-brain track-density mapping. *NeuroImage*, **53** (4): 1233–1243.

[62] F. Calamante, et al. (2011). Track density imaging (TDI): validation of super resolution property. *NeuroImage*, **56** (3): 1259–1266.

[63] F. Calamante, et al. (2012). A generalised framework for super-resolution track-weighted imaging. *NeuroImage*, **59** (3): 2494–2503.

[64] K. Pannek, et al. (2011). The average pathlength map: a diffusion MRI tractography-derived index for studying brain pathology. *NeuroImage*, **55** (1): 133–141.

[65] F. Calamante, et al. (2013). Track-weighted functional connectivity (TW-FC): a tool for characterizing the structural–functional connections in the brain. *NeuroImage*, **70**: 199–210.

[66] T. Dhollander, et al. (2014). Track orientation density imaging (TODI) and track orientation distribution (TOD) based tractography. *NeuroImage*, **94** (0): 312–336.

[67] C. Bell, et al. (2014). Distance informed track-weighted imaging (diTWI): A framework for sensitising streamline information to neuropathology. *NeuroImage*, **86**: 60–66.

[68] A. Leemans, et al. (2009). The B-matrix must be rotated when correcting for subject motion in DTI data. *Magnetic Resonance in Medicine*, **61** (6): 1336–1349.

[69] A. Yendiki, et al. (2014). Spurious group differences due to head motion in a diffusion MRI study. *NeuroImage*, **88**: 79–90.

[70] D. Jones (2010). The signal intensity must be modulated by the determinant of the jacobian when correcting for eddy currents in diffusion MRI. In *Proc. ISMRM 18th Annual Meeting*, page 1644.

[71] T. G. Reese, et al. (2003). Reduction of eddy-current-induced distortion in diffusion MRI using a twice-refocused spin echo. *Magnetic Resonance in Medicine*, **49** (1): 177–182.

[72] D. Gallichan, et al. (2010). Addressing a systematic vibration artifact in diffusion-weighted MRI. *Human Brain Mapping*, **31** (2): 193–202.

[73] S. Mohammadi, et al. (2012). Correction of vibration artifacts in DTI using phase-encoding reversal (COVIPER). *Magnetic Resonance in Medicine*, **68** (3): 882–889.

[74] K. Pannek, et al. (2012). HOMOR: Higher Order Model Outlier Rejection for high b-value MR diffusion data. *NeuroImage*, **63** (2): 835–842.

[75] D. Raffelt, et al. (2011). Symmetric diffeomorphic registration of fibre orientation distributions. *NeuroImage*, **56** (3): 1171–1180.

[76] D. Raffelt, et al. (2012). Apparent Fibre Density: a novel measure for the analysis of diffusion-weighted magnetic resonance images. *NeuroImage*, **59** (4): 3976–3994.

[77] A. Collard, et al. (2012). An anisotropy preserving metric for DTI processing. *arXiv preprint arXiv:1210.2826*.

[78] J.-J. Wang, et al. (2011). Parkinson disease: diagnostic utility of diffusion kurtosis imaging. *Radiology*, **261** (1): 210–217.

[79] E. André, D, et al. (2014). Influence of noise correction on intra- and inter-subject variability of quantitative metrics in diffusion kurtosis imaging. *PLoS ONE*, **9** (4): e94531.

[80] Y. Assaf, et al. (2008). AxCaliber: a method for measuring axon diameter distribution from diffusion MRI. *Magnetic Resonance in Medicine*, **59** (6): 1347–1354.

[81] D. Barazany, et al. (2009). In vivo measurement of axon diameter distribution in the corpus callosum of rat brain. *Brain*, **132** (5): 1210–1220.

[82] D. C. Alexander, et al. (2010). Orientationally invariant indices of axon diameter and density from diffusion MRI. *NeuroImage*, **52** (4): 1374–1389.

[83] Y. Assaf, et al. (2005). Composite hindered and restricted model of diffusion (CHARMED) MR imaging of the human brain. *NeuroImage*, **27** (1): 48–58.

[84] C. Ros, et al. (2013). Atlas-guided cluster analysis of large tractography datasets. *PloS one*, **8** (12): e83847.

[85] P. Guevara, et al. (2012). Automatic fiber bundle segmentation in massive tractography datasets using a multi-subject bundle atlas. *NeuroImage*, **61** (4): 1083–1099.

[86] E. Garyfallidis, et al. (2012). QuickBundles, a method for tractography simplification. *Frontiers in Neuroscience*, **6** (175).

[87] R. M. Heidemann, et al. (2012). k-space and q-space: Combining Ultra-High Spatial and Angular Resolution in Diffusion Imaging using ZOOPPA at 7T. *NeuroImage*, **60** (2): 967–978.

[88] M. Aggarwal, et al. (2013). Feasibility of creating a high-resolution 3D diffusion tensor imaging based atlas of the human brainstem: A case study at 11.7 T. *NeuroImage*, **74**: 117–127.

[89] D. Le Bihan, et al. (2006). Direct and fast detection of neuronal activation in the human brain with diffusion MRI. *Proceedings of the National Academy of Sciences*, **103** (21): 8263–8268.

[90] T. Aso, et al. (2013). Comparison of diffusion-weighted fMRI and BOLD fMRI responses in a verbal working memory task. *NeuroImage*, **67**: 25–32.

[91] L. Haas (2003). Hans Berger (1873–1941), Richard Caton (1842–1926), and electroencephalography. *Journal of Neurology, Neurosurgery & Psychiatry*, **74** (1): 9–9.

[92] F. L. da Silva (2010). EEG: origin and measurement. In *EEG-fMRI*, pages 19–38. Springer.

[93] Y. C. Okada, et al. (1997). Genesis of MEG signals in a mammalian CNS structure. *Electroencephalography and clinical neurophysiology*, **103** (4): 474–485.

[94] M. Hämäläinen, et al. (1993). Magnetoencephalography—theory, instrumentation, and applications to noninvasive studies of the working human brain. *Reviews of Modern Physics*, **65** (2): 413.

[95] R. Oostenveld, et al. (2011). FieldTrip: open source software for advanced analysis of MEG, EEG, and invasive electrophysiological data. *Computational Intelligence and Neuroscience*, **2011** (156869).

[96] A. Delorme, et al. (2004). EEGLAB: an open source toolbox for analysis of single-trial EEG dynamics including independent component analysis. *Journal of Neuroscience Methods*, **134** (1): 9–21.

[97] A. Delorme, et al. (2011). EEGLAB, SIFT, NFT, BCILAB, and ERICA: new tools for advanced EEG processing. *Computational Intelligence and Neuroscience*, **2011** (130714).

[98] V. Litvak, et al. (2011). EEG and MEG data analysis in SPM8. *Computational Intelligence and Neuroscience*, **2011** (852961).

[99] A. Gramfort, et al. (2013). MEG and EEG data analysis with MNE-Python. *Frontiers in Neuroscience*, **7** (267).

[100] A. Gramfort, et al. (2014). MNE software for processing MEG and EEG data. *NeuroImage*, **86**: 446–460.

[101] Y. Leclercq, et al. (2011). FMRI artefact rejection and sleep scoring toolbox. *Computational Intelligence and Neuroscience*, **2011** (598206).

[102] Z. A. Acar, et al. (2010). Neuroelectromagnetic forward head modeling toolbox. *Journal of Neuroscience Methods*, **190** (2): 258–270.

[103] A. Gramfort, et al. (2010). OpenMEEG: opensource software for quasistatic bioelectromagnetics. *BioMedical Engineering OnLine*, **9**: 45.

[104] J. De Munck, et al. (1988). Mathematical dipoles are adequate to describe realistic generators of human brain activity. *IEEE Transactions on Biomedical Engineering*, **35** (11): 960–966.

[105] L. Koessler, et al. (2007). Spatial localization of EEG electrodes. *Neurophysiologie Clinique/Clinical Neurophysiology*, **37** (2): 97–102.

[106] A. Zani, et al. (2003). *The cognitive electrophysiology of mind and brain*. Academic Press.

[107] H. v. Helmholtz (1853). Ueber einige gesetze der vertheilung elektrischer ströme in körperlichen leitern mit anwendung auf die thierisch-elektrischen versuche. *Annalen der Physik*, **165** (6): 211–233.

[108] S. Rush, et al. (1969). EEG electrode sensitivity-an application of reciprocity. *IEEE Transactions on Biomedical Engineering*, **16** (1): 15–22.

[109] S. J. Kiebel, et al. (2008). Variational Bayesian inversion of the equivalent current dipole model in EEG/MEG. *NeuroImage*, **39** (2): 728–741.

[110] C. Phillips, et al. (2002). Anatomically informed basis functions for eeg source localization: combining functional and anatomical constraints. *NeuroImage*, **16** (3): 678–695.

[111] C. Phillips, et al. (2005). An empirical Bayesian solution to the source reconstruction problem in EEG. *NeuroImage*, **24** (4): 997–1011.

[112] J. Mattout, et al. (2006). MEG source localization under multiple constraints: an extended Bayesian framework. *NeuroImage*, **30** (3): 753–767.

[113] R. Henson, et al. (2010). A parametric empirical bayesian framework for fMRI-constrained MEG/EEG source reconstruction. *Human Brain Mapping*, **31** (10): 1512–1531.

[114] K. Friston, et al. (2008). Multiple sparse priors for the M/EEG inverse problem. *NeuroImage*, **39** (3): 1104–1120.

[115] X. Lei, et al. (2011). fMRI functional networks for EEG source imaging. *Human Brain Mapping*, **32** (7): 1141–1160.

[116] R. Grech, et al. (2008). Review on solving the inverse problem in EEG source analysis. *Journal of neuroengineering and rehabilitation*, **5** (1): 25.

[117] A. Fornito, et al. (2011). Genetic influences on cost-efficient organization of human cortical functional networks. *The Journal of Neuroscience*, **31** (9): 3261–3270.

[118] P. M. Thompson, et al. (2013). Genetics of the connectome. *NeuroImage*, **80**: 475–488.

[119] M.-C. Chiang, et al. (2008). Brain fiber architecture, genetics, and intelligence: a high angular resolution diffusion imaging (HARDI) study. In *Medical Image Computing and Computer-Assisted Intervention–MICCAI 2008*, pages 1060–1067. Springer.

[120] M.-C. Chiang, et al. (2009). Genetics of brain fiber architecture and intellectual performance. *The Journal of Neuroscience*, **29** (7): 2212–2224.

[121] M.-C. Chiang, et al. (2011). Genetics of white matter development: a DTI study of 705 twins and their siblings aged 12 to 29. *NeuroImage*, **54** (3): 2308–2317.

[122] M. Lommatzsch, et al. (1999). Abundant production of brain-derived neurotrophic factor by adult visceral epithelia: implications for paracrine and target-derived neurotrophic functions. *The American Journal of Pathology*, **155** (4): 1183–1193.

[123] J. M. Conner, et al. (1997). Distribution of brain-derived neurotrophic factor (BDNF) protein and mRNA in the normal adult rat CNS: evidence for anterograde axonal transport. *The Journal of Neuroscience*, **17** (7): 2295–2313.

[124] H. W. Horch, et al. (2002). BDNF release from single cells elicits local dendritic growth in nearby neurons. *Nature Neuroscience*, **5** (11): 1177–1184.

[125] D. Panja, et al. (2014). BDNF mechanisms in late LTP formation: a synthesis and breakdown. *Neuropharmacology*, **76**: 664–676.

[126] L. Cao, et al. (2007). Genetic modulation of BDNF signaling affects the outcome of axonal competition in vivo. *Current Biology*, **17** (11): 911–921.

[127] K. K. Singh, et al. (2008). Developmental axon pruning mediated by BDNF-p75NTR-dependent axon degeneration. *Nature Neuroscience*, **11** (6): 649–658.

[128] C.-J. Hong, et al. (2011). Effects of BDNF polymorphisms on brain function and behavior in health and disease. *Brain Research Bulletin*, **86** (5): 287–297.

[129] J. A. Kleim, et al. (2006). BDNF val66met polymorphism is associated with modified experience-dependent plasticity in human motor cortex. *Nature Neuroscience*, **9** (6): 735–737.

[130] T. L. Petryshen, et al. (2010). Population genetic study of the brain-derived neurotrophic factor (BDNF) gene. *Molecular Psychiatry*, **15** (8): 810–815.

[131] L. Mascetti, et al. (2013). Concurrent synaptic and systems memory consolidation during sleep. *The Journal of Neuroscience*, **33** (24): 10182–10190.

[132] W. B. Webb, et al. (1971). Stage 4 sleep: influence of time course variables. *Science*, **174** (4016): 1354–1356.

[133] J. V. Rétey, et al. (2005). A functional genetic variation of adenosine deaminase affects the duration and intensity of deep sleep in humans. *Proceedings of the National Academy of Sciences*, **102** (43): 15676–15681.

[134] V. Bachmann, et al. (2012). Functional ADA polymorphism increases sleep depth and reduces vigilant attention in humans. *Cerebral Cortex*, **22** (4): 962–970.

[135] C. E. Rasmussen, et al. (2005). *Gaussian Processes for Machine Learning (Adaptive Computation and Machine Learning)*. The MIT Press.

[136] J. Schrouff, et al. (2013). PRoNTo: pattern recognition for neuroimaging toolbox. *Neuroinformatics*, **11** (3): 319–337.

[137] A. P. Robinson, et al. (2004). Model validation using equivalence tests. *Ecological Modelling*, **176** (3): 349–358.

[138] A. P. Robinson, et al. (2005). A regression-based equivalence test for model validation: shifting the burden of proof. *Tree Physiology*, **25** (7): 903–913.

[139] H. Wickham (2009). *ggplot2: elegant graphics for data analysis*. Springer New York.

[140] C. Zheng, et al. (2012). Testing bioequivalence for multiple formulations with power and sample size calculations. *Pharmaceutical statistics*, **11** (4): 334–341.

[141] C. Lauzon, et al. (2009). Easy multiplicity control in equivalence testing using two one-sided tests. *The American Statistician*, **63** (2): 147–154.

[142] O. Kohannim, et al. (2012). Predicting white matter integrity from multiple common genetic variants. *Neuropsychopharmacology*, **37** (9): 2012–2019.

[143] M.-C. Chiang, et al. (2012). Gene network effects on brain microstructure and intellectual performance identified in 472 twins. *The Journal of Neuroscience*, **32** (25): 8732–8745.

[144] E. Sprooten, et al. (2014). Common genetic variants and gene expression associated with white matter microstructure in the human brain. *NeuroImage*, **In Press**.

[145] N. Jahanshad, et al. (2013). Multi-site genetic analysis of diffusion images and voxelwise heritability analysis: A pilot project of the ENIGMA–DTI working group. *NeuroImage*, **81**: 455–469.

[146] N. Jahanshad, et al. (2013). Genome-wide scan of healthy human connectome discovers SPON1 gene variant influencing dementia severity. *Proceedings of the National Academy of Sciences*, **110** (12): 4768–4773.

[147] M.-C. Chiang, et al. (2011). BDNF gene effects on brain circuitry replicated in 455 twins. *NeuroImage*, **55** (2): 448–454.

[148] H. Tost, et al. (2013). Effects of the BDNF val66met polymorphism on white matter microstructure in healthy adults. *Neuropsychopharmacology*, **38** (3): 525–532.

[149] D. J. Brooks, et al. (2011). Imaging biomarkers in Parkinson's disease. *Progress in neurobiology*, **95** (4): 614–628.

[150] C. J. Cochrane, et al. (2013). Diffusion tensor imaging in parkinsonian syndromes a systematic review and meta-analysis. *Neurology*, **80** (9): 857–864.

[151] K. Worsley, et al. (1999). Detecting changes in nonisotropic images. *Human Brain Mapping*, **8** (2-3): 98–101.

[152] S. Hayasaka, et al. (2004). Nonstationary cluster-size inference with random field and permutation methods. *NeuroImage*, **22** (2): 676–687.

[153] B. B. Avants, et al. (2008). Symmetric diffeomorphic image registration with cross-correlation: evaluating automated labeling of elderly and neurodegenerative brain. *Medical image analysis*, **12** (1): 26–41.

[154] B. Avants, et al. (2004). Geodesic estimation for large deformation anatomical shape averaging and interpolation. *NeuroImage*, **23**: S139–S150.

[155] B. B. Avants, et al. (2010). The optimal template effect in hippocampus studies of diseased populations. *NeuroImage*, **49** (3): 2457–2466.

[156] S. M. Smith, et al. (2006). Tract-based spatial statistics: voxelwise analysis of multi-subject diffusion data. *NeuroImage*, **31** (4): 1487–1505.

[157] R. E. Burke, et al. (2013). Axon degeneration in Parkinson's disease. *Experimental neurology*, **246**: 72–83.

[158] Y. Li, et al. (2009). Mutant LRRK2^{R1441G} BAC transgenic mice recapitulate cardinal features of Parkinson's disease. *Nature Neuroscience*, **12** (7): 826–828.

[159] M. Herkenham, et al. (1991). Selective retention of MPP$^+$ within the monoaminergic systems of the primate brain following MPTP administration: An *in vivo* autoradiographic study. *Neuroscience*, **40** (1): 133–158.

[160] L. A. Volpicelli-Daley, et al. (2011). Exogenous α-synuclein fibrils induce lewy body pathology leading to synaptic dysfunction and neuron death. *Neuron*, **72** (1): 57–71.

[161] J. E. Galvin, et al. (1999). Axon pathology in Parkinson's disease and Lewy body dementia hippocampus contains α-, β-, and γ-synuclein. *Proceedings of the National Academy of Sciences*, **96** (23): 13450–13455.

[162] M. Coleman (2005). Axon degeneration mechanisms: commonality amid diversity. *Nature Reviews Neuroscience*, **6** (11): 889–898.

[163] K. Tsukamoto, et al. (2012). Significance of apparent diffusion coefficient measurement for the differential diagnosis of multiple system atrophy, progressive supranuclear palsy, and Parkinson's disease: evaluation by 3.0-T MR imaging. *Neuroradiology*, **54** (9): 947–955.

[164] N. Weiskopf, et al. (2008). Multi-parameter mapping of the human brain at 1mm resolution in less than 20 minutes. In *Proc. Intl. Soc. Magn. Reson. Med*, volume 16, page 2241.

[165] G. Stanisz, et al. (1999). Characterizing white matter with magnetization transfer and T2. *Magnetic Resonance in Medicine*, **42** (6): 1128–1136.

[166] T. Bjarnason, et al. (2005). Characterization of the NMR behavior of white matter in bovine brain. *Magnetic Resonance in Medicine*, **54** (5): 1072–1081.

[167] G. Helms, et al. (2008). High-resolution maps of magnetization transfer with inherent correction for RF inhomogeneity and T1 relaxation obtained from 3D FLASH MRI. *Magnetic Resonance in Medicine*, **60** (6): 1396–1407.

[168] N. Gelman, et al. (2001). Interregional variation of longitudinal relaxation rates in human brain at 3.0 T: relation to estimated iron and water contents. *Magnetic Resonance in Medicine*, **45** (1): 71–79.

[169] P. Peran, et al. (2007). Voxel-based analysis of R2* maps in the healthy human brain. *Journal of Magnetic Resonance Imaging*, **26** (6): 1413–1420.

[170] T.-Q. Li, et al. (2009). Characterization of T2* heterogeneity in human brain white matter. *Magnetic Resonance in Medicine*, **62** (6): 1652–1657.

[171] G. Helms, et al. (2009). Improved segmentation of deep brain grey matter structures using magnetization transfer (MT) parameter maps. *NeuroImage*, **47** (1): 194–198.

[172] N. Weiskopf, et al. (2011). Unified segmentation based correction of R1 brain maps for RF transmit field inhomogeneities (UNICORT). *NeuroImage*, **54** (3): 2116–2124.

[173] P. Péran, et al. (2010). Magnetic resonance imaging markers of Parkinson's disease nigrostriatal signature. *Brain*, **133** (11): 3423–3433.

[174] M. Ulla, et al. (2013). Is R2* a New MRI Biomarker for the Progression of Parkinsons Disease? A Longitudinal Follow-Up. *PLoS ONE*, **8** (3): e57904.

[175] N. Weiskopf, et al. (2013). Quantitative multi-parameter mapping of R1, PD*, MT, and R2* at 3T: a multi-center validation. *Frontiers in Neuroscience*, **7** (95).

[176] J. Ashburner (2007). A fast diffeomorphic image registration algorithm. *NeuroImage*, **38** (1): 95–113.

[177] J. Sarvas (1987). Basic mathematical and electromagnetic concepts of the biomagnetic inverse problem. *Physics in medicine and biology*, **32** (1): 11–22.

[178] d. J. Munck, et al. (1993). A fast method to compute the potential in the multisphere model. *IEEE Transactions on Biomedical Engineering*, **40** (11): 1166–1174.

[179] F. Kariotou (2004). Electroencephalography in ellipsoidal geometry. *Journal of Mathematical Analysis and Applications*, **290** (1): 324–342.

[180] A. Gramfort, et al. (2011). Forward field computation with OpenMEEG. *Computational Intelligence and Neuroscience*, **2011** (923703).

[181] J. Fingberg, et al. (2003). Bio-numerical simulations with SimBio. *NEC Research and Development*, **44** (1): 140–145.

[182] C. Wolters, et al. (2006). Influence of tissue conductivity anisotropy on EEG/MEG field and return current computation in a realistic head model: a simulation and visualization study using high-resolution finite element modeling. *NeuroImage*, **30** (3): 813–826.

[183] H. Hallez, et al. (2007). Review on solving the forward problem in EEG source analysis. *Journal of neuroengineering and rehabilitation*, **4** (1): 46.

[184] T. Neuling, et al. (2012). Finite-element model predicts current density distribution for clinical applications of tDCS and tACS. *Frontiers in Psychiatry*, **3** (83).

[185] C. Saiote, et al. (2014). Impact of transcranial direct current stimulation on fatigue in multiple sclerosis. *Restorative neurology and neuroscience*, **In Press**.

[186] C. S. Herrmann, et al. (2013). Transcranial alternating current stimulation: a review of the underlying mechanisms and modulation of cognitive processes. *Frontiers in Human Neuroscience*, **7** (279).

[187] W. Goldsmith, et al. (2004). A biomechanical analysis of the causes of traumatic brain injury in infants and children. *The American Journal of Forensic Medicine and Pathology*, **25** (2): 89–100.

[188] O. Clatz, et al. (2005). Realistic simulation of the 3-D growth of brain tumors in MR images coupling diffusion with biomechanical deformation. *IEEE Transactions on Medical Imaging*, **24** (10): 1334–1346.

[189] K. Gorgolewski, et al. (2011). Nipype: a flexible, lightweight and extensible neuroimaging data processing framework in Python. *Frontiers in Neuroinformatics*, **5** (13).

[190] P. Dular, et al. (1998). A general environment for the treatment of discrete problems and its application to the finite element method. *IEEE Transactions on Magnetics*, **34** (5): 3395–3398.

[191] L. D. Eggert, et al. (2012). Accuracy and reliability of automated gray matter segmentation pathways on real and simulated structural magnetic resonance images of the human brain. *PloS one*, **7** (9): e45081.

[192] E. H. Gronenschild, et al. (2012). The effects of FreeSurfer version, workstation type, and Macintosh operating system version on anatomical volume and cortical thickness measurements. *PLoS One*, **7** (6): e38234.

[193] R. Van Uitert, et al. (2003). Volume currents in forward and inverse magnetoencephalographic simulations using realistic head models. *Annals of biomedical engineering*, **31** (1): 21–31.

[194] P. H. Schimpf (2007). Application of quasi-static magnetic reciprocity to finite element models of the MEG lead-field. *IEEE Transactions on Biomedical Engineering*, **54** (11): 2082–2088.

[195] S. Vallaghé (2010). *EEG and MEG forward modeling: computation and calibration*. PhD thesis, University of Picardie, France.

[196] A. Thibaut, et al. (2014). tDCS in patients with disorders of consciousness: Sham-controlled randomized double-blind study. *Neurology*, **82** (13): 1112–1118.

[197] P. Ritter, et al. (2013). The virtual brain integrates computational modeling and multimodal neuroimaging. *Brain Connectivity*, **3** (2): 121–145.

[198] P. S. Leon, et al. (2013). The Virtual Brain: a simulator of primate brain network dynamics. *Frontiers in Neuroinformatics*, **7**.

[199] M. Dannhauer, et al. (2011). Modeling of the human skull in EEG source analysis. *Human Brain Mapping*, **32** (9): 1383–1399.

[200] K. Eley, et al. (2012). "Black bone" MRI: a partial flip angle technique for radiation reduction in craniofacial imaging. *British Journal of Radiology*, **85** (1011): 272–278.

[201] A. Fedorov, et al. (2012). 3D Slicer as an image computing platform for the Quantitative Imaging Network. *Magnetic Resonance Imaging*, **30** (9): 1323–1341.

[202] C. Geuzaine, et al. (2009). Gmsh: A 3-D finite element mesh generator with built-in pre-and post-processing facilities. *International Journal for Numerical Methods in Engineering*, **79** (11): 1309–1331.

[203] F. Darvas, et al. (2006). Generic head models for atlas-based EEG source analysis. *Human Brain Mapping*, **27** (2): 129–143.

[204] S. T. Schwarz, et al. (2013). Diffusion tensor imaging of nigral degeneration in Parkinson's disease: A region-of-interest and voxel-based study at 3T and systematic review with meta-analysis. *NeuroImage: Clinical*, **3**: 481–488.

[205] J. E. Desmond, et al. (2002). Estimating sample size in functional MRI (fMRI) neuroimaging studies: statistical power analyses. *Journal of Neuroscience Methods*, **118** (2): 115–128.

[206] J. Carp (2012). The secret lives of experiments: methods reporting in the fMRI literature. *NeuroImage*, **63** (1): 289–300.

[207] J. Carp (2012). On the plurality of (methodological) worlds: estimating the analytic flexibility of fMRI experiments. *Frontiers in Neuroscience*, **6** (149).

[208] N. J. Tustison, et al. (2013). Instrumentation bias in the use and evaluation of scientific software: recommendations for reproducible practices in the computational sciences. *Frontiers in Neuroscience*, **7** (162).

[209] J. Zimmermann, et al. (2012). Network-based statistics for a community driven transparent publication process. *Frontiers in computational neuroscience*, **6**.

[210] A. E. Budden, et al. (2008). Double-blind review favours increased representation of female authors. *Trends in ecology & evolution*, **23** (1): 4–6.

[211] H. G. Morrison (2012). *Freedom for scholarship in the internet age*. PhD thesis, Communication, Art & Technology: School of Communication.

[212] The Economist (2011). Of goats and headaches: One of the best media businesses is also one of the most resented.

[213] The Economist (2014). Global ageing: A billion shades of gray. Apr 26th.

[214] A. M. Davies (2008). Neurotrophins giveth and they taketh away. *Nature neuroscience*, **11** (6): 627–628.

[215] L. M. de Lau, et al. (2006). Epidemiology of parkinson's disease. *The Lancet Neurology*, **5** (6): 525–535.

[216] E. Dorsey, et al. (2007). Projected number of people with parkinson disease in the most populous nations, 2005 through 2030. *Neurology*, **68** (5): 384–386.

[217] D. Mosher (2011). Visual cortexes: Brain-art competition shows off neuroscience's aesthetic side.

[218] J.-P. Toussaint, et al. (2012). *La main et le regard: livre/louvre.[Paris, musée du Louvre,... 7 mars au 11 juin 2012]*. Louvre éd.

[219] IEEE (2009). IEEE Standard for Information Technology–Systems Design–Software Design Descriptions. *IEEE STD 1016-2009*, pages 1–35.

[220] IEEE Computer Society. Software Engineering Standards Committee and IEEE-SA Standards Board (1998). IEEE Recommended Practice for Software Requirements Specifications.

License

This work is licensed under a Creative Commons Attribution-ShareAlike 4.0 International License.

Curriculum Vitae

Erik Cserep Ziegler was born in Reading, United Kingdom on December 8th, 1986. He obtained his high school diploma in 2004 from Bluevale Collegiate Institute in Waterloo, Ontario, Canada. He then attended the University of Toronto where he studied Materials Science & Engineering with a focus on nanomaterials and nanoengineering. He graduated with a Bachelor's degree in Applied Science in 2008 and moved to Sweden.

In 2010 in Gothenburg, Sweden he obtained his Master's degree in Applied Physics at Chalmers University of Technology. During and after his Master's thesis Erik worked at the Sahlgrenska University Hospital and the University of Gothenburg Department of Neuroscience & Neurophysiology. Here he performed EEG experiments related to tactile sensation and contributed to the EU FP6 project "NANOBIOTACT".

In 2010 he moved to Liège, Belgium to begin his doctoral program as a Marie Curie Fellow at the Cyclotron Research Centre. As part of the EU FP7 Marie Curie Initial Training Network "NEUROPHYSICS", he collaborated with researchers at Maastricht University, Jülich Forchungzentrum in Germany, and GlaxoSmithKline in the United Kingdom.

Acknowledgements

First and foremost I'd like to thank my wonderful girlfriend Lizette for her patience, help, and support. Without you I would never have gotten this far.

Next I'd like to thank all my amazing friends in Liège that have listened to my complaints for the past four years. Thanks a ton to Vanessa, Florian, Anahita, Fabian, Johan, Elodie, Vincenzo, Olivia, Luca, Ariane, Lucie, Vincent, Aurore, Athena, Yaniv, Mathieu, Yorgos, Enrico, Marine, Sarah, Giulia, Gian-Luca, and Marlène. I hope le Pot au Lait will survive without me. Thanks as well to my office-mates Khadidja and Jitka for all the candy and distractions.

Thanks to my co-authors for dealing with my impatience. I'm especially grateful for Ariane Forêt, Maud Rouillard, Evelyne Balteau, Pierre Maquet, Gaëtan Garraux, and Christophe Geuzaine.

I'd also like to thank the others that have taught me so much. Specifically I'd like to thank Mohamed Bahri, Andrea Soddu, "Patcho" Gomez, Quentin Noirhomme, Gilles Vandewalle, Eric Salmon, and Steven Laureys. Special thanks as well to the Nipy* development team and especially Satrajit Ghosh, Chris Gorgolewski, and John Griffiths.

The valorization of this doctoral work would not have been possible without Maro Sciacchitano and Tristan Renaud. We are immensely in debt to Francois Foglia of IDIAP and his vision of the International Create Challenge. I'd also like to thank Christophe Van Huffel and André Luxen for their support.

My heartfelt thanks to my supervisors Rainer Goebel, Alard Roebroeck, and Christophe Phillips for their supervision and trust. I know how lucky I've been; few doctoral advisors would allow their students the free rein I've been given and for that I am extremely grateful.